

**Percolation of Oxide Networks in Nano-Composite
Lithium Salt Electrolytes**

Von der Fakultät Chemie der Universität Stuttgart
zur Erlangung der Würde eines
Doktors der Naturwissenschaften (Dr. rer. nat.)
genehmigte Abhandlung

Vorgelegt von

Anna Jarosik

aus Sieraków (Polen)

Hauptberichter:	Prof. Dr. Joachim Maier
Mitberichter:	Prof. Dr. Klaus Müller
Weiterer Prüfer:	Prof. Dr. Joachim Bill
Prüfungsvorsitzender:	Prof. Dr. Thomas Schleid

Tag der Einreichung:	29.10.2009
Tag der mündlichen Prüfung:	11.12.2009



MAX-PLANCK-INSTITUT FÜR FESTKÖRPERFORSCHUNG

Stuttgart

2009

...to my parents and sister, for love, support and care. Thank You.

...moim rodzicom i siostrze, za miłość, wsparcie i opiekę. Dziękuję.

Zusammenfassung

Die vorliegende Arbeit hat die Untersuchung des Netzwerkverhaltens in Fest-Flüssig-Kompositelektrolyten zum Ziel. Die Resultate wurden zum große Teil mit Hilfe von Simulationen erhalten, die sich an realen Systemen orientieren. Die Bildung von Netzwerken durch Füllstoffe als Funktion des Volumenanteils und der Partikelgröße führt zu interessanten Einflüssen auf die elektrochemischen sowie mechanischen Eigenschaften. In der Literatur wurde bereits berichtet, dass die Dispersion von Oxiden in nichtwässrigen Flüssigelektrolyte ("soggy sand" Elektrolyte) sowie in Polymerelektrolyten zu einem Anstieg der Leitfähigkeit führen kann. Während in Polymerelektrolyten verschiedene Erklärungen angeführt werden – die meisten dieser Vorschläge sehen Veränderungen in der Mobilität durch Segmentbewegungen des Lösungsmittels bzw. Polymers und Veränderungen des Kristallinitätsgrades als mögliche Ursachen für den Leitfähigkeitanstieg an – wird in den "soggy sand" electrolytes Ionenadsorption als wahrscheinlichster Mechanismus angeführt. Der Austausch von hochpolaren Lösemitteln gegen Lösemittel geringer Polarität erlaubt es, die Möglichkeit von Ionenadsorption genauer zu untersuchen. Hierbei wird vermutet, dass eine erhöhte Ladungsträgerkonzentration durch selektive Adsorption einer Ionensorte an der isolierenden Oberfläche der Oxidpartikel resultiert. Der Adsorptionseffekt ist ein Spezialfall des allgemeinen Konzepts von heterogen dotierten Ionenleitern (z. B. AgCl , PbF_2), das ursprünglich in Stuttgart entwickelt wurde, um den Zweitphaseneffekt auf die Leitfähigkeit schwacher Festelektrolyte zu erklären.

Das Hauptargument besteht im Sachverhalt, dass in einer kovalenten Matrix, wie Polymeren oder organischen Molekülkristallen, der Grundzustand die undissoziierten Ionenpaare sind. Durch Adsorption einer Ionensorte werden die Ionenpaare aufgebrochen und mobile Gegenionen generiert, wodurch die Leitfähigkeit steigt. Die verbesserte Leitfähigkeit zeigt das für Grenzleitfähigkeit typische Perkolationsverhalten. Werden Oxide mit ausreichend saurer Oberfläche benutzt, kann angenommen werden, dass die Oxidpartikel die Anionen an der Oberfläche einfangen. Dieser Vorgang führt ganz allgemein zu einem Überschuss an Gegenionen in den Raumladungszonen nahe des Oxides. Der Perkolationsvorgang beruht auf Partikelwechselwirkungen und dem resultierenden Netzwerkverhalten und involviert Packungseffekte, Partikelnetzwerkbildung sowie Partikelstabilität. All diese Wechselwirkungen und damit die Lithiumionenleitung hängen

demgemäß von der Größe der Partikel, deren Oberfläche und Volumenanteil, sowie von der Dielektrizitätskonstante und Polarität des Lösungsmittel ab; außerdem von der Konzentration und Natur der Lithiumsalze. In dieser Arbeit wurden ‘Monte Carlo Random Walk’ Simulationen durchgeführt, die unterschiedliche Partikelgrößen und Volumenanteile berücksichtigen.¹ Derartige Simulationen erleichtern das Verständnis von Netzbildung und – stabilität in Kompositelektrolyten. Zunächst wurde die Netzbildung durch einen irreversiblen ‘hit-and-stick’ Mechanismus (*diffusionslimitierte Clusteraggregation*) modelliert. Sobald die Partikel ein Netzwerk gebildet haben (*fraktale Perkulationscluster*), können sie auf einer längeren Zeitskala zusammenballen, und damit ihre Oberflächenenergie herabsetzen. Ein derartiges Verklumpen der Partikel führt zu einer raschen Unterbrechung der Perkulationspfade und einer allgemeinen Leitfähigkeitserniedrigung mit der Zeit. Ab einem bestimmten Punkt sinkt die Leitfähigkeit unter den Wert des partikelfreien Elektrolyten. Die wahrscheinlichste Erklärung dafür ist, dass das Zusammenballen der Partikel zu kompakteren Clustern sowie stärkerer und schnellerer Sedimentierung führt, wodurch Elektrolyt eingeschlossen wird.

Die Resultate der vorliegenden Arbeit zeigen, dass Oxidpartikel attraktive, zusammenhängende Netzwerke bilden, die zur Agglomeration neigen. Diese Netzwerke bilden fraktale Perkulationsstrukturen. Perkulation führt schon bei kleinen Volumenanteilen zu erhöhter Leitfähigkeit. Auf einer längeren Zeitskala ballen sich diese Netzwerke zusammen und werden kompakter, wodurch der kontinuierliche Perkulationspfad gestört und Lösungsmittel im Sediment eingeschlossen wird. Dadurch sinkt mit der Zeit die Leitfähigkeit in derartigen Kompositelektrolyten. Aufgrund des beobachteten Packungseffektes kann geschlussfolgert werden, dass sich die Stabilität des Systems deutlich verbessert, wenn kleinere Partikel, sowie höhere Volumenanteile und viskosere Lösungsmittel benutzt werden. Neben den Simulationen wurden Experimente an Modellsystemen basierend auf niedermolekularen Polyethylenglykolen durchgeführt.

¹Wir danken Prof. A. Bunde, Theoretische Physik III, Universität Gießen, für seine Hilfe.

Abstract

The starting point for this work was to investigate the network behaviour present in solid-liquid composite electrolytes. Results are obtained using simulations based on real systems. The formation of networks of filler particles that depend sensitively on volume fraction and particles size, results in interesting influences on electrochemical as well as mechanical properties. In the literature it has been already found that the dispersion of oxides can lead to a conductivity increase in non-aqueous electrolytes (e.g. “soggy sand” electrolytes) as well as in polymer electrolytes. For the latter various explanations are proposed in the literature, many of those concentrating on the change in the mobility owing to segmental motion or variation in the degree of crystallinity as possible causes for the increase in conductivity. In the case of the “soggy sand” electrolytes ion adsorption was proposed as most probable mechanism. Replacing the high polarity solvent with a solvent of low polarity allows one to address the ion adsorption scenario more explicitly. The enhancement of the charge carrier concentration is expected to be due to the selective adsorption of one ion sort on the insulating surface of the introduced oxide particles. The adsorption effect is a special case of the general concept of heterogeneously doped ion conductors – originally developed in Stuttgart for explaining second phase effect on the conductivity of weak solid electrolytes – e.g. AgCl, PbF₂.

In a covalent matrix, such as polymers and organic molecular crystals, the immobile ground state is the undissociated ion pair and the conductivity effect is attributed due to the adsorption of one of the pair’s constituents. This would result in a break-up of the ion pair and the generation of a mobile counter ion, thereby increasing the ion conduction. The enhanced conductivity showed percolation behaviour that is typical for interfacial conductivity. As oxides with sufficiently acidic surfaces were used, one could presume that the oxide particles are able to trap the anions on the surface, resulting in the dissociation of ion-pairs in solution. This, in general, leads to an excess of cations in the space charge regions around the oxide particles. It was observed that lithium ion conduction depends on particles size, surface area or volume fraction, on the solvent’s dielectric constant and viscosity, as well as on concentration and nature of the different lithium salts. In this thesis ‘Monte Carlo Random Walk’

was applied taking into account variation of particle size and volume fraction.¹ This ‘Random Walk’ simulation helps to better understand network formation and stability of these composite electrolytes. At first, the network formation was modelled according to an irreversible ‘hits-and-stick’ mechanism (*diffusion-limited cluster aggregation*). Then, once the particles form a network (*fractal percolating cluster*), they are allowed to coarsen on a longer time scale, which leads to minimization of their surface energy. Coarsening, as was found, rapidly interrupts the percolation pathways resulting in overall decrease of the conductivity with time, which at certain point is lower compared to ‘filler-free’ electrolytes. The most reasonable explanation suggests that due to coarsening more compact clusters are formed, stronger and faster sedimentation occurs that consequently leads to trapping of the solvent, thereby pronouncedly decreasing the composite’s conductivity.

The results show that oxide particles form attractive, coherent networks that tend to agglomerate. This formation corresponds to the ‘hit-and-stick’ mechanism and to the formation of percolating fractal structure. Percolation can lead to a conductivity increase already at small volume fractions. The simulations show that with decreased particle size the percolation threshold appears significantly earlier. On a longer time scale, these networks coarsen, become more compact, and sediment. Because of coarsening the conductivity decreases with time in such composite electrolytes. Owing to the observed packing effect it can be concluded that the stability of the system is greatly enhanced when the particle size is smaller, the volume fraction higher and when more viscous solvents are used. The modelling is accompanied by experiments on model systems based on low molecular weight poly(ethylene glycol).

¹The help of Professor Armin Bunde, Theoretical Physics III, Giessen University is gratefully acknowledged.

Contents

1	Introduction and Motivation	1
1.1	Lithium-based batteries and the electrolyte problem	5
1.1.1	Non-aqueous liquid and polymer electrolytes	6
1.1.2	Composite Electrolytes	7
1.2	Heterogeneous Doping	9
1.3	Colloids	11
1.4	Network formation and stability	13
1.5	Motivation	16
2	Experimental Section	19
2.1	Electrolyte Components	19
2.1.1	Solvents	19
2.1.2	Lithium Salts	20
2.1.2.1	Lithium Perchlorate ($LiClO_4$)	21
2.1.2.2	Lithium Chloride ($LiCl$)	21
2.1.3	Oxide Fillers	21
2.2	Instrumental techniques	24
2.2.1	Brunauer – Emmett – Teller Surface Area Analyser (BET)	24
2.2.2	Scanning Electron Microscope (SEM)	24
2.2.3	Differential Scanning Calorimeter (DSC)	24
2.2.4	(Electrochemical) Impedance Spectroscopy (EIS)	24
2.2.5	Acoustic and Electroacoustic Spectroscopy	28
2.2.6	Rheology	30
2.3	Experimental Results	32
2.3.1	Thermal Analysis by Differential Scanning Calorimetry (DSC)	32

CONTENTS

2.3.2	Ionic Conductivity	37
2.3.2.1	Methodology Of Equivalent Circuit Modelling	37
2.3.2.2	Ionic Conductivity Results	41
2.3.3	Transference number	52
2.3.3.1	Method	52
2.3.3.2	Results	54
2.3.4	Zeta-Potential	60
2.3.4.1	Theory	60
2.3.4.2	Results	61
2.3.5	Viscosity	65
2.3.5.1	Fluids behaviours	65
2.3.5.2	Results	66
3	Numerical Modelling and Simulation	71
3.1	Modelling Methods	71
3.1.1	‘Monte Carlo Random Walk Method’	71
3.1.2	Metropolis-Hastings algorithm	74
3.2	‘Hit-and-Stick’ Mechanism	75
3.3	Coarsening	82
4	Discussion	89
4.1	Interpretation	91
4.2	Outlook and search for appropriate “Soggy Sand” electrolytes	95
5	Conclusions	97
	Symbols and Abbreviations	99
	List of Figures	105
	List of Tables	109
	Bibliography	111

1

Introduction and Motivation

Since the end of the 20th century we have observed an exponential growth and interest in portable electronic devices (*PEDs*) such as CD-, MP-players, laptop computers, video games, cellular telephones etc. This interest in wireless devices leads to an enormous demand in compact, light-weight batteries, offering high energy densities. Energy density is a significant parameter indicating the amount of energy stored in a given system per mass or volume. Because of high energy density lithium-based batteries are appealing for many such applications. Recently they are also in the focus as regards electrotraction.

The motivation of using a battery technology based on lithium metal as anode was based on the fact that Li is the most electropositive (-3.04 V, versus standard hydrogen electrode) as well as the lightest (equivalent weight 6.94 g · mol⁻¹, and density 0.53 g · mol⁻³) metal, thus enabling the design of high performance storage systems (1). Lithium-based batteries provide a higher energy density compared to the other rechargeable battery systems such as lead-acid car batteries, whose chemical process was recognised in 1859 by G. Planté. Batteries of nickel-cadmium type, operating on the electrochemical reaction proposed by W. Jungner in 1899. These different battery systems are shown in Figure 1.1.

The advantage of Li-batteries was demonstrated by M. S. Whittingham (Binghamton University, Exxon) in the 1970s (2). Whittingham used titanium sulfide as a cathode and lithium metal as an anode. TiS₂ was the best intercalation compound available at that time, having a favourable layered-type structure. But in spite of the impeccable operation of the positive electrode, the system was not without flaws. Due

1. INTRODUCTION AND MOTIVATION

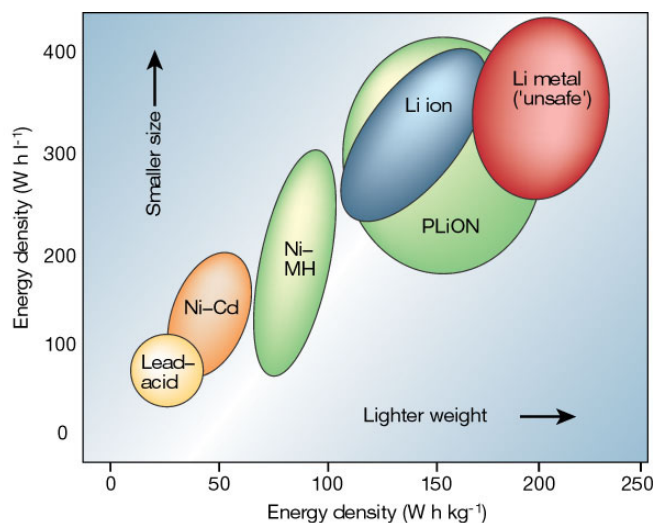


Figure 1.1: Comparison of the different battery technologies in terms of volumetric and gravimetric energy density (1). Used with permission.

to a poor surface properties of the material, it soon encountered the shortcomings of a Li-metal/liquid electrolyte combination, caused by dendritic lithium growth during each subsequent discharge-recharge cycle. This led to explosion hazards and/or fire. In the meantime, significant advances in intercalation materials had occurred with the realization at Bell Labs that oxides were providing higher capacities and voltages (3, 4). To circumvent the safety issues surrounding the use of Li metal, several alternative approaches were pursued in which either the electrolyte or the negative electrode was modified. The first approach involved substituting metallic Li for a second insertion material. The concept was first demonstrated in the laboratory by Murphy and co-workers (5), and then by Scrosati and co-workers (6) and led, at the end of the 1980s and early 1990s, to the so-called Li-ion or rocking-chair technology (Fig. 1.2). The principle of rocking-chair batteries had been used previously in Ni-MH batteries (1, 8). Today nickel-metal hydride (Ni-MH) batteries are widely used in hybrid car technologies. This technology was developed by Toyota and initially used in Toyota Prius (1997–2003). At present time this technology is also used in the company's Prius, Highlander Hybrid, Camry Hybrid, Lexus RX 400h/RX 450h, Lexus GS 450h, Lexus LS 600h/LS 600hL, and Lexus HS 250h automobiles and also by Nissan Altima Hybrid. The newest Hybrid Synergy Drive (*HSD*) in recent Prius (model NHW20, 2004–2009)

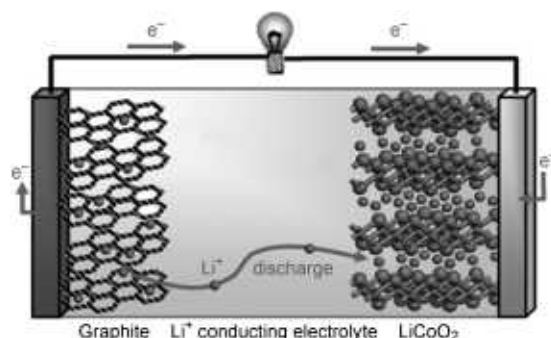


Figure 1.2: Schematic representation of a lithium-ion battery. Negative electrode (graphite), positive electrode(LiCoO₂), separated by a non-aqueous liquid electrolyte (7). Used with permission.

uses an all-electric A/C compressor for cooling, an electric power steering system to further minimize engine belt-driven engine accessories, combined with a smaller and lighter Ni-MH battery (9).

The presence of Li in its rather ionic than metallic state in so-called Li-ion cells, solves the dendrite problem and are, in principle, inherently safer than Li metal cells. Nevertheless, it took quite a long time to implement the Li-ion concept. Delays were attributed to the lack of suitable materials for the negative electrode and the failure of electrolytes to meet safety and operational requirements. Besides safety measures, the costs and performance requirements for a battery technology to succeed also played a role (1). Lithium-ion batteries became a reality when Bell Labs developed a workable graphite anode to provide an alternative to the (metallic lithium anode) lithium battery (10). The discovery of the highly reversible, low voltage Li intercalation-deintercalation process in carbonaceous material (providing that carefully selected electrolytes are used), led to the creation of the Carbon/LiCoO₂ rocking-chair cell, commercialized by Sony Corporation in June 1991 (1). This type of Li-ion cell, having a potential exceeding 3.6 V (three times that of alkaline systems) and gravimetric energy densities as high as 120-150 W · h · kg⁻¹ (two to three times of usual Ni-Cd batteries), is found in most of today's high-performance portable electronic devices (1). Although, the battery production is a large-scale industry producing several million batteries per month, nevertheless, Li-ion batteries still require many improvements such as energy capacity to be more efficient for more and more demanding portable electronic devices. At the moment one strives to introduce the LiFePO₄/FePO₄ redox

1. INTRODUCTION AND MOTIVATION

couple as cathode owing to its environmental benignity, capacity and rate performance, in spite of its lower operation voltage (~ 3.5 V) (11, 12).

1.1 Lithium-based batteries and the electrolyte problem

A rechargeable lithium-based battery is composed of several electrochemical cells that are connected in series (or in parallel) to provide the required voltage (or current). Each cell consists of a positive and a negative electrode separated by an electrolyte solution containing dissociated salts, which enable ions transfer between them (1). A representation of the lithium-ion device is shown in Figure 1.2, where graphite is used as a negative electrode (anode during discharge) and the positive electrode (cathode during discharge) is composed of LiCoO_2 . The electrode materials determine the battery voltage and the energy density. The high voltage of Li-ion batteries (typically 4 V) is one major advantage. Both the anode (at high Li potential) and the cathode (at low Li potential) are not thermodynamically stable against typical electrolytes. Kinetic stability is achieved by passivation layers, yet in the case of an accident the volatility and flammability is a crucial problem. This leads to a closer look on the electrolyte.

When it comes to the electrolytes, there are mainly three types in common use: liquids, gels and solids. Liquid and gel electrolytes are based on non-aqueous solvents, and contain lithium salts. Recently, also ionic liquids came into the focus of interest. The gel electrolytes are solid-like electrolytes because the liquid component is incorporated into a polymer matrix. There is also a great interest in electrolytes based only on polymers and salts (solid electrolytes), however, in this case one has to overcome their low conductivities (13, 14, 15, 16, 17), what is the main theme of this thesis; in addition solid electrolytes (unlike the “soggy sand” electrolytes) are not compatible with nano-structuring of the electrodes as one wants an electrolyte penetration into the pores.

The basic requirements for the electrolytes applicable to electrochemical devices are as follows (18, 19):

- High ionic conductivity (to minimize the cell resistance and resistive heating of the device).
- High chemical stability (to prevent decomposition of electrolyte on the surface of a highly reducing anode materials).

1. INTRODUCTION AND MOTIVATION

- Electrochemical stability (to tolerate the high voltage difference between anode and cathode (≥ 4 V) without being reduced or oxidized, including the possibility to form stable passivation layers).
- Low melting point (to provide sufficient conductivity at sub-ambient temperatures, and prevent solidification, and phase separation).
- High boiling point and reactivity (to provide safety and prevent explosions resulting from high pressure build-up in the cell).
- Immobilization of anions (soaking etc.)
- Low cost (to be affordable and compete with existing power sources using aqueous electrolytes).

Ionic conductivity and stability are the key parameters in selecting an electrolyte, but the solvent properties, and dynamics of ion solvent interaction, must be clearly understood in order to design the new ionic conductors. Although the role of electrolyte is often considered trivial, its choice is crucial, and is based on whether or not a solid polymer or a liquid-based electrolyte should be employed in the fabrication of the Li-ion rechargeable batteries (1). More details concerning different types of electrolytes are presented in the following subsections.

1.1.1 Non-aqueous liquid and polymer electrolytes

Non-aqueous liquids as well as some low molecular weight polymers are used as solvents for lithium salts making up the electrolyte solution. One can also consider molten salts as liquid electrolytes. These electrolyte systems dissolve salts forming ionic phases which are highly ionically conductive. In the case of solid electrolytes one can, besides polymers, consider inorganic solids (e. g. based on sulfides), as well as plasticized and gelled electrolytes (based on e. g. poly(lithium oligoetherato mono-oxalato borate) and others (20, 21)). With reference to the type of solvent used, liquid electrolytes can be aqueous (*water*), mixed aqueous (*water* and *co-solvent*), and non-aqueous (*organic* or *inorganic solvent*) electrolyte solutions. Molten salts may be classified according to their useful liquid range as high-temperature and ambient-temperature molten salts (*ionic liquids*), which are often based on mixtures of organic halides with aluminium

1.1 Lithium-based batteries and the electrolyte problem

trichloride. Also solid polymer electrolytes (*SPEs*) can be included within the liquid electrolytes, as they exhibit various properties typical for this type of electrolytes. SPEs are usually composed of a blend of a solvating polymer and a salt or a non-aqueous electrolyte solution containing ionic salts and other solid particles (22). The choice of electrolytes is not unambiguous as one can find advantages as well as disadvantages in both major types of ionic conductors (solid and liquid). When compared with solid electrolytes liquid electrolytes generally show better stabilities for both temperature and concentration discontinuities and allow for small volume changes during chemical or electrochemical reactions (22). They also maintain a permanent interfacial contact at the electrolyte/electrode interface (which is most important in the case of nano-structured electrodes) and have generally higher conductivities. Yet, in contrast to solid electrolytes, they do not function as a separator in a battery. Further disadvantages of liquid electrolytes are potential gassing and leakage in cells, and the higher effort in cell assembling (22).

So, in order to combine advantages from liquid electrolyte as well as from solid electrolyte, this research work focuses on composite electrolytes, which appear very promising for the development of rechargeable lithium batteries. They can also provide improved performance in terms of cyclability and power output (15).

1.1.2 Composite Electrolytes

Composite electrolytes are a type of ionic conductors which are obtained by the addition of inert fillers to the solid or liquid electrolyte. Such fillers are usually non-reacting oxide particles that provide a support matrix for the conductive amorphous complex. They (the composite electrolytes) retain an overall solid structure even at high temperatures, while maintaining liquid-like configuration at the microscopic level necessary to assure fast ionic mobility. Probably, first useful liquid-solid electrolyte was demonstrated by A. Chandra and J. Maier (23). The concept of “soggy sand” electrolytes (A. J. Bhattacharyya and J. Maier (24)) then even used synergistic conductivity effects in that the addition of finely dispersed ceramic powders not only greatly improves the mechanical stability of such electrolytes, moreover a number of studies confirmed that incorporation of a ceramic component can even lead to enhanced conductivities (specifically at low temperatures), increased lithium ion transport numbers and improved electrode-electrolyte interfacial stability (23, 24, 25). Composite electrolytes may be considered

1. INTRODUCTION AND MOTIVATION

as bi-continuous two-phase materials, whose transport characteristics are influenced by both the content of the dispersoid and by its particle size. Previous studies confirm that increase in the conductivity is observed in the case of nano-sized particles. The rationale behind the increase in conductivity in these solvent systems is considered in this thesis. While the local mechanisms have been addressed in Reference (24), this thesis focuses on the formation and the stability of the filler network that is indispensable for percolation and hence long range conductivity.

1.2 Heterogeneous Doping

Heterogeneous doping is a concept that was proposed by J. Maier (26) to explain the surprising findings that the ionic conductivity is increased by several orders of magnitude, if cationic conductors such as LiI, LiCl, AgCl, AgBr, CuCl, CuBr as well as anionic conductors such as CaF₂, SrF₂ or PbF₂, contain fine, insulating oxide particles such as Al₂O₃ and SiO₂ (26, 27, 28). The concept relies on ionic space charge regions, the region of redistribution of ionic and electronic point defects occurring as a result of differences in the defect's local free energy in the bulk and at the surface (here the contact to the oxide particle). This corresponds to internal adsorption of one ion sort on the insulating surface, which thereby increases 'dissociation' of ions and hence increases ion conduction (Fig. 1.3). In the case of crystalline Ag⁺ or F⁻ conductors (e. g. AgCl : Al₂O₃ or CaF₂ : SiO₂ composites) this may be the adsorption of Ag⁺ or F⁻ ions. This is connected with their removal from the energetically deep-lying regular position, resulting in the generation of charge carriers – here vacancies – as mobile carriers. The space charge potential itself depends on the charge density and hence on the number of newly formed (mobile) charge carriers. If the ions are majority carriers also the electron concentrations in the ionic conductors are determined by the interaction of the ions with the interface. In such cases the electronic carrier concentration is acid-base controlled rather than redox controlled. From literature it is known that small oxide particles are preferentially located at the grain boundary of the relatively large ionic conductor grains and form coherent conductivity paths even at a relatively low volume fraction (26, 29). This means that the first continuous path (*percolation threshold*) is

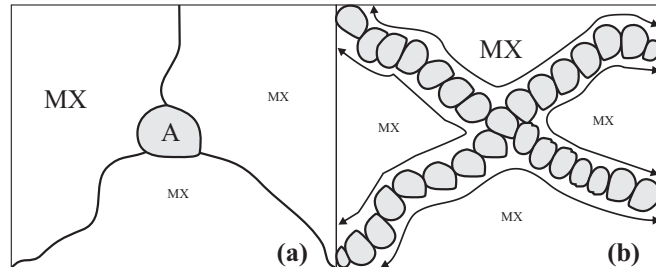


Figure 1.3: By cation adsorption the insulating A particles induce highly conducting boundary layers in the ionic conductor MX. In (a) the A-grain is isolated and in (b) the coherent paths are formed between the MX grains (29).

1. INTRODUCTION AND MOTIVATION

already created at low values of volume fraction, φ . If such a network is maintained and increase of oxide admixture leads to lower grain sizes, the specific conductivity, σ_m is approximately linear in the volume concentration, as expressed by Equation 1.1

$$\sigma_m = (1 - \varphi) \cdot \beta_\infty \cdot \sigma_\infty + \varphi \cdot \beta_L \cdot \sigma_L \quad (1.1)$$

where β_∞ and β_L measure the number of parallel, continuous paths. These factors are independent of the volume fraction of oxide particles (φ) and temperature (T) under the above conditions (σ_∞ bulk conductivity, σ_L mean space charge layer conductivity).

One can expect a similar effect in ionically conducting polymers, owing to the less polar environment. Lithium salt (e. g. LiClO_4) which is introduced into polymers, such as high-molecular weight poly(ethylene oxide), is not completely dissociated. Because of this, adsorption of one ion sort on the oxide particle surfaces, as proposed in the heterogeneous doping concept (26), results in breaking up the ion pairs. In the polymers it is also probable that this involves mobility effects, such as segmental motion or amorphization. Figure 1.4 compares the principle of heterogeneous doping (*introduc-*

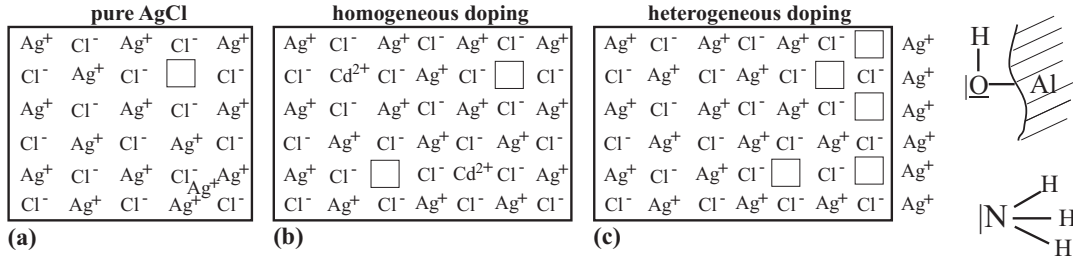


Figure 1.4: As in homogeneous doping, heterogeneous doping lowers or raises in a predictable manner the concentration of the individual defects. However, the effect is limited to the region near the interface (29).

tion of metastable higher-dimensional defects) (29) with that of homogeneous doping (*introduction of metastable impurity point defects*) with regard to conductivity. Owing to its generality, it is reasonable to apply the concept of heterogeneous doping to liquid ionic conductors as well.

1.3 Colloids

Colloidal science is concerned with mixtures of different phases in which the particle size of at least one phase is in between 1 nm and 1 μm . Even though too large to be atomistically dissolved, these particles are also small enough to be nano-dispersed and to maintain a homogeneous appearance, and again large enough to scatter light.

The factors which contribute most to the overall nature of colloidal systems are:

- Particle size,
- Surface properties,
- Particle-Particle interactions,
- Particle-Solvent interactions.

A characteristic feature of colloidal dispersion is its large area-to-volume ratio. Adsorption of ions and formation of double layer takes place at the interfaces between the dispersed phase and the dispersion medium. Such surface properties play an important role in determining the physical properties of the system as a whole.

The following terms are frequently used to describe the tendency of a surface or functional group to become solvated (30):

1. **lyophilic** (“liquid-loving”) – system in which the disperse phase comprises substances, which readily adsorb solvent and may swell, and even stay homogeneous,
2. **lyophobic** (“liquid-hating”) – system in which the disperse phase (oxide particles such as Al_2O_3 , SiO_2) does not attractively interact with liquids. On a long run, it is usually precipitated, and cannot be re-dispersed with additional solvent.

If one considers a simple, two-phase colloidal dispersion system, the particles in it are sufficiently large for definite surfaces of separation to exist between the particles and the medium in which they are dispersed. The phases in dispersions are distinguished by the terms *dispersed phase* or *internal phase* (forming the particles) and *dispersion medium* or *continuous phase* (the medium in which the particles are distributed). Sols (which means solid dispersed in liquid), gels (liquid dispersed in solid) and emulsions (liquid in liquid) are by far the most important types of colloidal dispersion. A characteristic feature of colloidal dispersions is the large area-to-volume ratio for the particles

1. INTRODUCTION AND MOTIVATION

involved. At the interfaces between the dispersed phase and the dispersion medium characteristic surface properties such as adsorption, electric double layer effects and specific interactions between particles, are important. They also play a crucial role in determining the physical properties of the system as a whole. Colloidal particles often carry an electrical charge and therefore attract or repel each other. Another interaction that one can find between colloidal particles are van der Waals forces. They exist between dipoles that are either permanent or induced and hence always present as short-range, and attractive forces. Due to the mentioned interactions between colloidal particles one can consider stabilization as well as destabilization effects in such colloidal dispersions. Stabilization serves to prevent colloids from aggregating and destabilization makes unstable colloidal systems aggregate. Electrostatic stabilization is based on the mutual repulsion because of the same electrical charges on the particles surfaces. Removing or reducing repulsive forces that keep colloidal particles separated or overcoming these barriers by thermal events will lead to coagulation due to omnipresent van der Waals forces. For example, addition of a salt to a suspension, can neutralize or ‘screen’ the surface charge of the particles in suspension and introduce flocculation. Colloidal systems exhibit also quite interesting rheological behaviours which are intermediate between Newtonian viscous fluids and Hookean elastic solids. One can consider steady-state phenomena (such as shear-thinning and shear-thickening) and time-dependent phenomena (such as thixotropy). If particles aggregate in a colloidal system, then the shear rate increase will tend to break down the aggregates, which in consequence decrease the viscosity of the system what is typical for shear-thinning behaviour. Opposite effects one can observe due to shear-thickening which is characterized by an increase in viscosity with increased rate of deformation. Shear-thinning systems typically show a thixotropic behaviour: if the system is allowed to stand and is then sheared at a constant rate, the viscosity decreases with time until a balance between structural break-down and structure re-formation is reached (30).

1.4 Network formation and stability

From a fundamental perspective, network formation is a percolation process within the constrained geometry of the particular microstructure. In the simplest model system containing an insulating and a conducting phase, one finds randomly occupied sites on a squared lattice, with concentration p , as well as empty ones with concentration $1 - p$ (31). If one assumes that occupied sites represent electrical conductors and the empty sites represent insulators, two conductor sites belong to the same cluster if they are connected by a path of nearest neighbour conductor sites. Such a contact is necessary for a current to flow. At low p values, the mixture is an insulator, since a conducting path connecting opposite edges of the lattice does not exist. However, at large p values, typically many conduction paths exist between opposite edges, and consequently the mixture is a conductor (31). Hence at some concentration in between, a threshold concentration, p_c , exists, where electrical current can *percolate* from one edge to the other for the first time. Below this concentration one has an insulator and above a conductor. The threshold concentration is called *percolation threshold* or *critical concentration*. The above mentioned percolation is considered *site percolation*, where the sites of a lattice have been occupied randomly. When the bonds between sites are randomly occupied, one can speak of *bond percolation*. Two occupied bonds belong to the same cluster if they are connected by a path of occupied bonds. In general, the main difference between both types of percolation (site and bond) is that, in a given lattice, a bond percolation corresponds to more of the nearest neighbours than site percolation. This is due to the fact that on a 2D square lattice one bond is connected to six nearest neighbour bonds, while a site has four nearest neighbour sites. In our case the conducting phase conducts via the heterointerface. Yet again, percolation of the conducting phase is necessary.

In order to consider a real system with percolation let us turn back to the previously mentioned colloids. A colloidal suspension is a fluid containing small charged particles that are kept afloat by Brownian motion and kept apart by Coulombic repulsion. Nevertheless owing to mentioned interactions between charged particles, an aggregation process occurs on a long run and consequently clusters of growing size are created. If these clusters are formed rapidly they form fractal networks. Pioneering work was done by M. Smoluchowski, who formulated a kinetic theory for the irreversible aggregation

1. INTRODUCTION AND MOTIVATION

of single particles into clusters and further clusters combining with clusters. It appears that there are two distinct limiting regimes of the irreversible colloidal aggregation process, namely:

1. A diffusion limited regime (*Diffusion-Limited Cluster Aggregation, DLCA*), in which the reaction rate is determined by the time it takes for the clusters to encounter each other by diffusion.
2. A reaction limited regime (*Reaction-Limited Cluster Aggregation, RLCA*), in which the aggregation is rate limiting. Often the term RLCA is – unprecisely – used for the case that the aggregation reaction is not completely reversible (31).

The interactions between charged colloidal particles in electrolyte solutions play an essential role in determining the structure and, therefore, the macroscopic properties of a colloidal system, such as stability, phase diagrams, and rheology. The main feature of the interaction between a pair of colloidal particles can be depicted by the Derjaguin-Landau-Verwey-Overbeek (*DLVO*) theory. This theory includes the electrostatic repulsion and van der Waals attraction and has been successful in explaining the stabilization of charged colloidal particles. It assumes that the forces are governed by Coulombic repulsion and attractive van der Waals forces. If by thermal events two particles come very close in spite of Coulombic repulsion, they stick together because of the deeper van der Waals minimum (see Fig. 1.5).

Figure 1.5 and Figure 1.6 indicate the energetic variations for a lyophobic colloid as a function of the distance between approaching interfaces. At infinity, which may mean a few microns, the force is essentially zero. At an extremely short distance, where the two interfaces are in contact, the force is always attractive owing to van der Waals interaction or even specific chemical bonding (e. g. sintering). Depending on the case the force balance at intermediate distance (even as short as 100 Å) can be repulsive (Fig. 1.5(a)) or not (Fig. 1.5(b)). The cases in which Figure 1.5(a) or Figure 1.5(b) apply, depend on the nature of particles, the solvent, the state of the interface (charge, adsorbed surfactant) etc. In the first case (Fig. 1.5(a)) which is representative for most of our systems, the force is repulsive at a longer distance, and there is a barrier, which needs to be overcome if the two interfaces are to adhere. A high barrier is thus associated with a stable colloidal system. This barrier increases with interfacial charge, electrical double layer, adsorption of ions and decreases when

electrolyte is added (*DLVO*). In Figure 1.5(b) the force is attractive at all distances

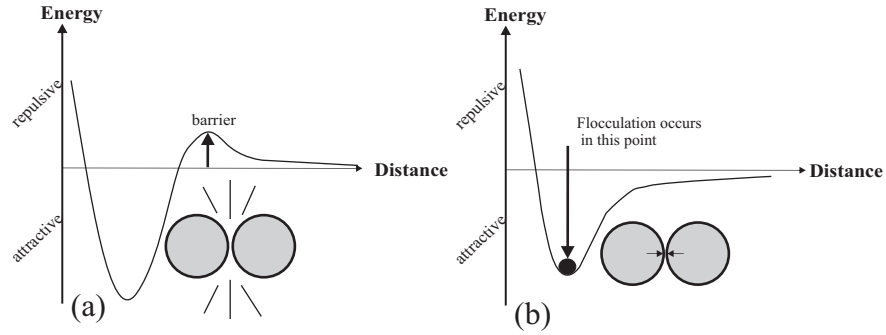


Figure 1.5: Forces ((a) repulsive, (b) attractive) as a function of the distance between colloidal particles.

and the approach proceeds until the minimum is reached, where the most stable state is encountered. Depending on whether this minimum occurs at a short or very short distance, a matter of few Å indeed, the situation is called *flocculation*, *coagulation* or *aggregation*.

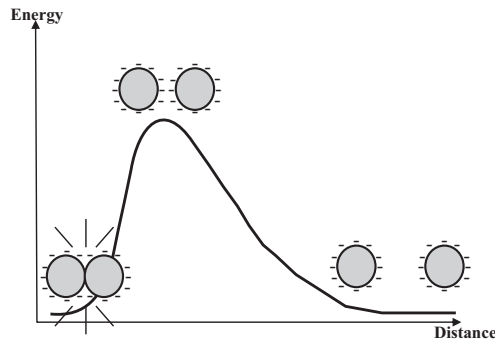


Figure 1.6: Interactions between charged particles depend on distance between them.

1.5 Motivation

In the present thesis, liquid/solid composite electrolytes are explored, as such composites of solids and non-aqueous lithium salt solutions can be successfully used as electrolytes in lithium ion batteries, and in other electrochemical devices (e.g. electrochromic windows and dye sensitized solar cells). Already at low oxide-particle content, investigated systems showed enhanced conductivities compared to liquid electrolytes together with the favourable mechanical properties typical of gel-like electrolytes. Conductivity increases have been found in non-aqueous electrolytes (24, 32, 33), but also in solid and liquid polymer electrolytes (17, 34, 35, 36). In the case of polymers the suggested explanations (19, 37, 38) include change in mobility owing to a segmental motion of the solvents or polymers, and variation in the degree of crystallinity (39). Ion adsorption on the surface of the particles has also been suggested (24, 32, 33, 40, 41, 42). Replacing the high polarity solvent with a liquid solvent of low polarity allows one to address the ion adsorption scenario more explicitly. An enhancement of ion conduction should indicate enhancement of the charge carrier concentration due to selective adsorption of ions on the oxide surface. Such an adsorption effect is a special case of the general concept of heterogeneous doping of ion conductors (26). In a covalent matrix, such as polymers and organic molecular crystals, the immobile ground state would be the undissociated ion pair and the conductivity effect would be due to the adsorption of one of the pair's constituents. This would result in a break-up of the ion pair; generating a mobile counter ion. Using lithium salts dissolved in a liquid solvent of low polarity allows us to investigate the influence of the ion adsorption process as a function of the lithium salt and the oxide concentration. The enhanced conductivity shows a percolation behaviour that is typical of interfacial conductivity. As oxides with sufficiently acidic surfaces are used, one can presume that the oxide particles trap anions on the surface, resulting in excess of cations (in this case Li^+) in the space charge region – in the vicinity of the oxide.

To explore composite electrolyte systems, for this thesis, experimental as well as theoretical studies were conducted. By analysing the experimental results, a number of stable systems were identified, which provided the parameters for the theoretical approach of the cluster network formation in solutions. The filler (oxide) particles create clusters, and for a certain concentration threshold, a more or less stable cluster is created

that allows for percolation of the ions along the cluster. Essentially, the work presented here addresses as to why the network, having reached the percolation threshold, is unstable and sometimes collapses upon addition of a slight excess of filler particles. The particle network formation and stability, which is important for comprehending percolation and ageing aspects in the examined systems, were studied in this thesis.

1. INTRODUCTION AND MOTIVATION

2

Experimental Section

2.1 Electrolyte Components

2.1.1 Solvents

In accordance to the basic requirements for electrolytes, an ideal electrolyte solvent should meet the following criteria: **(1)** the solvent should be able to dissolve salts to a sufficient concentration (high dielectric constant, ϵ), **(2)** it should be a fluid (low viscosity, η) to facilitate ion transport, **(3)** it should remain inert to all cell components, especially to the cathode and the anode, during cell operation, **(4)** it should remain liquid in a wide temperature range (melting point, T_m , should be low and boiling point, T_b , high), **(5)** it should also be safe (high flash point, T_f), non-toxic, and economical. For lithium-based batteries, the active nature of the strongly reducing anodes (lithium metal, highly lithiated carbon) rule out the use of any solvents that have active protons despite their excellent power in solvating salts. The reduction of such protons and/or the oxidation of the corresponding anions generally occurs within 2.0-4.0 V versus lithium, while the potentials of the anode in the current rechargeable lithium devices are much less, namely at 0.0-0.2 V (43). In protic solvents also stabilizing kinetic barriers have not been demonstrated. On the other hand, the non-aqueous compounds that qualify as electrolyte solvents, must be able to dissolve sufficient amounts of lithium salt; therefore, those solvents typically contain polar groups such as carbonyl ($C=O$), nitrile ($-C\equiv N$), sulfonyl ($-S(=O)_2-$), and ether-linkage ($-O-$) (44) etc. A high electrochemical stability of the solution is related to the use of non-aqueous solvents and relatively inert anions of the lithium salt, which are not easily oxidized or reduced.

2. EXPERIMENTAL SECTION

Table 2.1: Properties of solvents used in electrolytes taken at $T = 25^\circ\text{C}$ (44, 45); *experimentally obtained viscosity at the shear rate, $\dot{\gamma} = 500 \text{ s}^{-1}$.

Solvents	Structure	T_m [$^\circ\text{C}$]	T_b [$^\circ\text{C}$]	T_f [$^\circ\text{C}$]	η [cP]	ϵ [-]	ρ [$\text{g} \cdot \text{cm}^{-3}$]
DMSO		18.55	189	87	1.99/5.79*	46.6	1.096
PEG-150		<-2	150	156	6.94*	23.9	1.016
PEG-350		<-15	>250	182	31.22*	25.2	1.106

The present dissertation focuses on three different solvents: **(1)** Poly(ethylene glycol)dimethyl ether, PEG-150 ($M_W = 150 \text{ g} \cdot \text{mol}^{-1}$, $\text{CH}_3\text{O}[\text{C}_2\text{H}_4\text{O}]_n\text{CH}_3$, $n \sim 3$, Fluka), **(2)** Methoxy polyethylene glycol, PEG-350 ($M_W = 350 \text{ g} \cdot \text{mol}^{-1}$, $\text{HO}[\text{C}_2\text{H}_4\text{O}]_n\text{CH}_3$, $n \sim 7$, Sigma) and **(3)** Dimethylsulfoxide, DMSO ($M_W = 78.13 \text{ g} \cdot \text{mol}^{-1}$, $\text{C}_2\text{H}_6\text{SO}$, Fluka, 99.5%) which were used as received.

Properties of the used solvents are presented in Table 2.1. For reasons that are explained later, the focus is on the first two solvents.

2.1.2 Lithium Salts

An ideal electrolyte solute should be able to completely dissolve and dissociate in the non-aqueous media. The solvated ions (lithium cations) should be able to move in the media with relatively high mobility. Another requirement is that the anion should be stable against oxidative decomposition at the cathode and also inert to electrolyte solvents. The anion and the cation should remain inert towards the other cell components such as the separator, the electrode substrates and the cell packing materials. It is also worth mentioning that the anion should be non-toxic and remain stable against thermally induced reactions with electrolyte solvents and other cell components (38).

In the present thesis two lithium salts, lithium perchlorate (LiClO_4) and lithium chloride (LiCl) are used.

2.1.2.1 Lithium Perchlorate (LiClO_4)

LiClO_4 has been a popular electrolyte solute owing to its satisfactory solubility and high conductivity (conductivity of 1M LiClO_4 is $5.6 \times 10^{-3} \text{ S} \cdot \text{cm}^{-1}$ in propylene carbonate (PC), $8.4 \times 10^{-3} \text{ S} \cdot \text{cm}^{-1}$ in ethylene carbonate/dimethyl carbonate (EC/DMC) (46), $6.2 \times 10^{-3} \text{ S} \cdot \text{cm}^{-1}$ in dimethylsulfoxide (DMSO) (47), at $T=25^\circ\text{C}$) as well as its high anodic stability (up to 5.1 V on a spinel cathode surface in EC/DMC (46)). The ionic radii of Li^+ is equal 0.060 nm and of ClO_4^- equal 0.236 nm (17). It should be mentioned that LiClO_4 in comparison with other lithium salts is less hygroscopic and is stable to ambient moisture. However, LiClO_4 is potentially a strong oxidant due to a high oxidation state of chloride (VII). It can react with most organic species under certain conditions such as a high temperature and high current charge. Nevertheless, it is frequently used in laboratory tests because it is easy to handle and kinetically inert (46).

Lithium perchlorate (LiClO_4 , Aldrich 99.99%) as received was used in preparation of non-aqueous and polymer electrolytes.

2.1.2.2 Lithium Chloride (LiCl)

On the contrary, LiCl salt is not a commonly used salt for preparing organic electrolytes since it is highly hygroscopic and not well soluble in non-polar solvents (e. g. polymers). LiCl is also not used due to the high polarizability of its anion (Cl^-) what in principle leads to easy distortion from its normal shape by an external electric field. The ion polarizability also determines the dielectric constant at high frequency (48). Its ionic radii are equal for Li^+ 0.060 nm and Cl^- 0.181 nm (17).

Lithium chloride (LiCl , Sigma-Aldrich 99.99%) as received was used in preparation of non-aqueous electrolytes.

2.1.3 Oxide Fillers

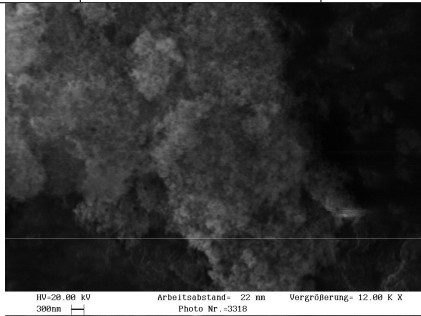
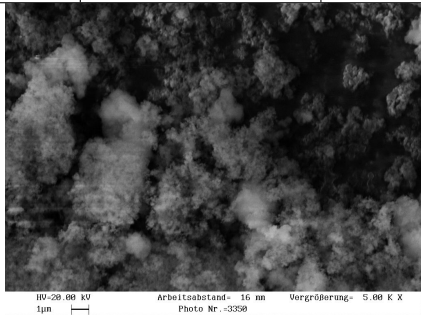
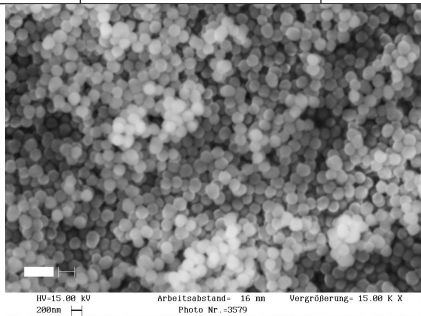
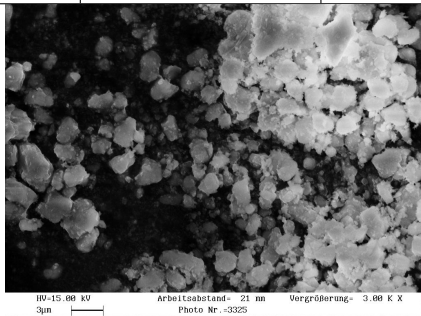
The preparation of the composite electrolytes requires addition of oxide fillers. A variety of oxide fillers were used to. Their morphological parameter are given in Table 2.2. The

2. EXPERIMENTAL SECTION

acidity of the oxides was determined on the basis of the point of zero charge (*pzc*) in aqueous solution (49). The low *pzc* for SiO₂ (*pzc* \simeq 3) provides high acidity and thus high affinity towards anion adsorption. Usually, the surface of highly pure and dispersed fumed silica is characterized by a high density of silanol (Si-OH) groups.

2.1 Electrolyte Components

Table 2.2: Oxides Properties

Oxide	Size, nm	Surface, BET _{area} /m ² · g ⁻¹	Density, g · cm ⁻³	IEC, mmol · m ⁻²
SiO ₂ -fumed	7	605.0	2.438	0.0032
				
SiO ₂	10	537.9	2.400	0.0037
				
SiO ₂	300	8.2	3.068	0.1780
				
ZrO ₂ (MEL)	10	182.5	4.555	0.0105
				

2. EXPERIMENTAL SECTION

2.2 Instrumental techniques

2.2.1 Brunauer – Emmett – Teller Surface Area Analyser (*BET*)

Specific surface areas of oxides were determined using multi-point Brunauer – Emmett – Teller (*BET*) N₂ adsorption and desorption isotherms, which were obtained from a Autosorb-1 Quantachrome surface area analyser (Quantachrome, Syosset, New York). The analysis refers to the BET equation:

$$\frac{1}{W((P_0/P) - 1)} = \frac{1}{W_m C} + \frac{C - 1}{W_m C} (P/P_0) \quad (2.1)$$

in which W is the weight of gas adsorbed at a relative pressure P_0 and W_m is the weight of adsorbate constituting a monolayer of surface coverage. The term C is related to the energy of adsorption in the first adsorbed layers and, consequently, its value is an indication of the magnitude of the adsorbent/adsorbate interactions.

2.2.2 Scanning Electron Microscope (*SEM*)

The S420 scanning electron microscope (*SEM*) equipped from Leica (Leica Microsystems GmbH Wetzlar, Germany) was used to study the surface morphology and to verify the size of the oxide particles.

2.2.3 Differential Scanning Calorimeter (*DSC*)

The thermal characterization of non-aqueous and polymer electrolytes was conducted using Differential Scanning Calorimetry (*DSC*) technique. Data were obtained between -100°C and 100°C at a heating/cooling rate of $10 \text{ K} \cdot \text{min}^{-1}$ using a Pyris 1 scanning calorimeter (Perkin Elmer Life And Analytical Sciences, Inc.). Samples were loaded into aluminium pans in an argon filled dry box. The instrument was calibrated by an empty aluminium pan in the first run and sapphire in the second run. The thermal effects identified in the samples were the glass transition temperature (T_g), crystallization temperature (T_c) and melting temperature (T_m). These are the essential quantities for the assessment of material properties and working conditions.

2.2.4 (Electrochemical) Impedance Spectroscopy (*EIS*)

Impedance spectroscopy is a powerful method for the characterization of electrical properties of materials and their interfaces with electronically conducting electrodes.

Electrical measurements to evaluate the electrochemical behaviour of electrode and/or electrolyte materials are usually made with cells that have two identical electrodes applied to the faces of a sample in the form of a circular cylinder or rectangular parallelepiped. Electrochemical impedance is measured by applying an AC (*alternating current*) potential to an electrochemical cell and measuring magnitude and phase of the current through the cell. If a monochromatic signal in the form of $V(t) = V_m \sin(\omega t)$ is applied to the cell, the resulting steady state current response is for small signals $I(t) = I_m \sin(\omega t + \theta)$, i. e. sinusoidal as well with the same frequency (ω). However, a phase shift between the voltage and current (θ) is observed, as in the Figure 2.1 (50).

It is convenient to present the impedance in form of a complex function, $Z = Z' + jZ''$.

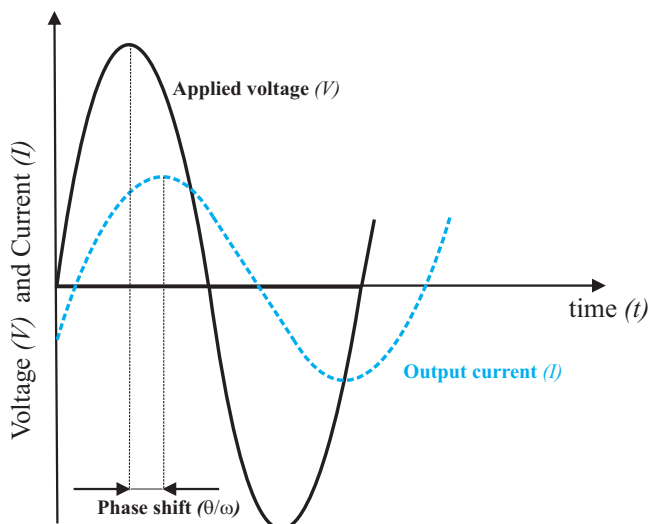


Figure 2.1: Sinusoidal voltage perturbation and current response.

The impedance (Z) may be plotted in the Gaussian plane, as shown in Figure 2.2.

Here, the two coordinate values are:

$$Re(Z) \equiv Z' = |Z| \cos(\theta) \quad (2.2)$$

and

$$Im(Z) \equiv Z'' = |Z| \sin(\theta) \quad (2.3)$$

with the phase angle:

$$\theta = \arctan(Z''/Z') \quad (2.4)$$

2. EXPERIMENTAL SECTION

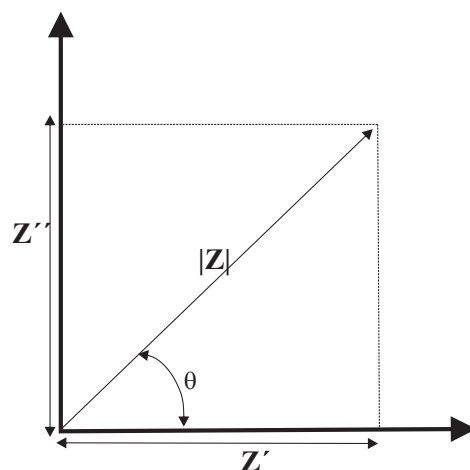


Figure 2.2: Impedance plot in a complex plane, Z' and Z'' are the real and imaginary part, respectively, of the impedance, $|Z|$ is the magnitude of impedance and θ the phase angle.

and the magnitude or modulus of total impedance:

$$|Z| = \sqrt{(Z')^2 + (Z'')^2} \quad (2.5)$$

Using Euler's relationship one can also write the impedance in exponential form:

$$Z = |Z|e^{-j\theta} \quad (2.6)$$

THE NYQUIST DIAGRAM

One of the common ways of transferring the electrochemical impedance data is plotting the imaginary part (Z'') as a function of the real part (Z') using the frequency as special parameter. This is called Cole-Cole diagram, complex plane impedance diagram or – the most popularly – Nyquist diagram (Fig. 2.3). The Nyquist diagram for a parallel resistor-capacitor ($R - C$), circuit is shown in Figure 2.3. The resistance is obtained as intercept of low frequencies and the capacitance from the frequency at the maximum according to:

$$\omega_{max} = \frac{1}{R \cdot C} \quad (2.7)$$

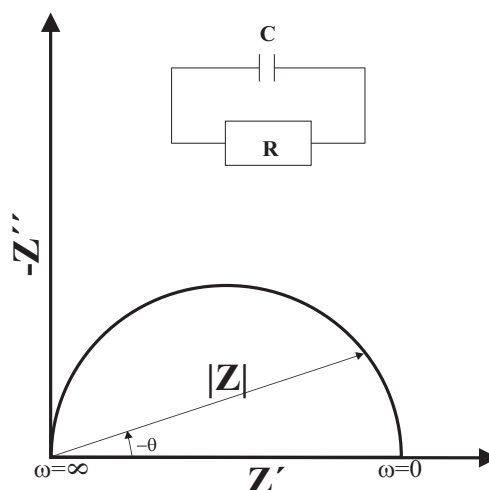


Figure 2.3: Nyquist diagram of a circuit consisting of a resistor, (R) parallel to a capacitor, (C).

THE BODE DIAGRAM

Another useful way of representing the impedance is to plot magnitude, ($|Z|$) and phase shift (θ) as functions of the angular frequency, (ω). In many cases these Bode plots are to be preferred as they reveal details more clearly than the Nyquist plot, although containing the same information as the latter.

CONSTANT PHASE ELEMENT (CPE)

In various complex cases the mapping of the situation by simple circuit elements R , C , L does not suffice. It is often helpful to introduce Constant Phase Elements (CPE). The CPE refers to an empirical impedance function of the type:

$$Z_{CPE} = A(j\omega)^{-z} \quad (2.8)$$

The parameter, z , is between 0 and 1. For $z = 1$, the Equation 2.8 reduces to the impedance of an ideal capacitor and for $z = 0$ to the impedance of an ideal resistor. The most common reason for a non-ideal z -value is electrode roughness, due to which there is a distribution of resistances and capacitances representing the roughness or surface porosity of an electrode interface. Apart from the above observation, CPE elements are also attributed to diffusion processes and/or inhomogeneous reaction rates on the surface or to a thickness variation of the sample.

2. EXPERIMENTAL SECTION

2.2.5 Acoustic and Electroacoustic Spectroscopy

Electroacoustics offer a useful possibility to characterize concentrated dispersed systems, where particle interaction is significant. There are two quite different approaches. Historically, the first approach began with works by Enderby and Booth (51). The initial theory was valid only for dilute systems and a system of classical electrokinetic equations without using any thermodynamic relationships were considered. An alternative approach to electroacoustic theory was suggested later by O'Brien (52). In this approach, the concept of a *dynamic electrophoretic mobility* (μ_d) was introduced and a relationship was derived between μ_d and the measured electroacoustic parameters such as *colloid vibration current* (CVI) (53):

$$CVI = k\rho\varphi\mu_d|\nabla P| \quad (2.9)$$

where k is cell constant, ρ is the contrast between particle density, ρ_p and liquid density, ρ_m equal: $\rho = (\rho_p - \rho_m) \cdot \rho_m^{-1}$, φ is the volume fraction of solid, μ_d is the dynamic electrophoretic mobility and $|\nabla P|$ is the magnitude of the pressure gradient of the sound waves.

According to O'Brien a complete functional dependence of CVI on ζ -potential, particle size, and frequency is incorporated into dynamic electrophoretic mobility:

$$\mu_d = \frac{CVI(\omega)}{k(\omega)F(Z_T, Z_s)\varphi\rho} \quad (2.10)$$

where the CVI is assumed to be normalized by the corresponding driving force ($|\nabla P|$), $k(\omega)$ is an instrument constant found by calibration, and $F(Z_T, Z_s)$ is a function of the acoustic impedances of the transducer and the dispersion under investigation. The coefficient of proportionality between CVI and μ_d is frequency independent as well as independent of particle size and ζ -potential (53, 54, 55). Taking into account the double layer polarization process, the dynamic mobilities for various values of κr (κ is the reciprocal Debye length, r is the particle radius) were calculated numerically (56, 57) and analytically (52). It was shown that the electrophoretic mobility for $\kappa r \gg 1$ is:

$$\mu_d = \frac{2\varepsilon\zeta}{3\eta}(1 + f(\lambda, \omega')) \quad (2.11)$$

where η is the dynamic viscosity of bulk solution, ζ is the zeta-potential of a colloidal particle, and:

$$f(\lambda, \omega') = \frac{1 - i\omega' - 2\lambda + i\omega'(\varepsilon_p/\varepsilon)}{2(1 - i\omega') + (2\lambda - i\omega'(\varepsilon_p/\varepsilon))} \quad (2.12)$$

where $\lambda = \sigma_s/\sigma_\infty \cdot r$ (σ_s is ‘surface’ conductivity, σ_∞ is the conductivity of the electrolyte beyond the double layer, r is particle radius) and $\omega' = \omega\varepsilon/\sigma_\infty = \omega/\kappa^2 D'_i$, since $\varepsilon/\sigma_\infty \approx 1/\kappa^2 D'_i$ (ε is dielectric constant and D'_i is diffusion coefficient) (52). The conventional method of DC electrophoresis may underestimate ζ for a sample with large λ (sound wave length), as in the case of the concentrated colloidal suspension. In such cases, ζ is obtained by using the high-frequency value of dynamic electrophoretic mobility according to the Smoluchowski equation.

An acoustic and electroacoustic spectrometer DT-1200 (Dispersion Technology, Inc., Quantachrome) were used to determinate the zeta-potential (ζ). The electroacoustic sensor measures magnitude and phase of the *colloid vibration current (CVI)* at 3 MHz. The CVI Probe consists of two parts: a transmitting and a receiving transducer. The first one consists of a piezoelectric transducer to convert a radio frequency (*RF*) pulse into acoustic energy, and a delay rod that launches this acoustic pulse into the slurry after a suitable delay. This acoustic excitation of the slurry causes the particles to gain induced dipole moments. The dipole moments from the particles add up to create an electric field, which can be sensed by a receiver (55). During the sound wave propagation in electrolyte solution, the motion of cations and that of anions may differ from each other because of their different masses. Therefore, the periodic excesses of either cations or anions should be produced at a given point in the solution, generating vibration potentials. This potential is called *ion vibration potential (IVP)*. A similar electroacoustic phenomenon occurs in a suspension of colloidal particles, and is called *colloid vibration potential (CVP)*. As colloidal particles are much larger and carry a far greater charge compared to the electrolyte ions, the potential difference in the suspension is caused by the asymmetry of the electrical double layer around each particle rather than by the relative motion of cations and anions. In the colloidal suspension, in the electrolyte solution, IVP and CVP are both generated simultaneously, and the total vibration potential between two points in the suspension is given by the sum of IVP and CVP (58).

2. EXPERIMENTAL SECTION

2.2.6 Rheology

A wide variety of viscosimeters suitable for liquid and colloid systems are currently available. The common models for measuring viscosity are: (1) stress is applied electrically to the system and strain is measured; and (2) strain is imposed to the system and stress is computed from the deformation of a calibrated spring system. Different measuring geometries such as simple parallel plates, cone and plane, Couette, Mooney, double gap are available (59). The designs are such that the shear rate is approximately constant throughout the sample.

Rheology measurements for the work presented here were conducted on a Haake RheoStress 1, using a plate-plate configuration, where the sample is placed between two round titan plates. In this configuration, the upper plate is rotated, and the lower one is fixed in place. Advantages of such an arrangement are that only small sample volumes are needed and the mass of the upper plate can be kept low to minimise the moment of inertia. In the parallel-disk (plate-plate) rheometer (Fig. 2.4), when the upper disk is rotated at a constant angular velocity (Ω) the shear rate value ($\dot{\gamma}$) can be calculated using:

$$\dot{\gamma} = \frac{\Omega \cdot r_{plate}}{h} \quad (2.13)$$

where r_{plate} is the plate radius and h is the variable distance between the stationary and

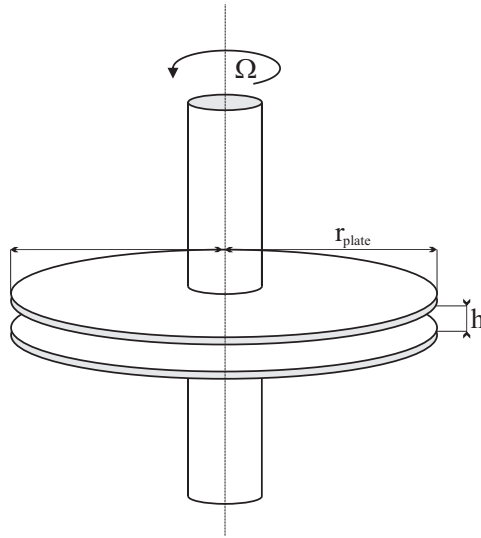


Figure 2.4: Plate-Plate Sensor Systems

the movable plate. The angular velocity (Ω) is calculated according to $2\pi/60 \cdot l$ from the speed l . A further value important in determination fluid properties is the shear stress, τ , which is proportional to the torque (M_d) and to the stress factor (S): $\tau = S \cdot M_d$. The factor S is: $S = 2/\pi \cdot r_{plate}^3$.

In the following we measured the viscosity (η) of the sample as a function of shear strain rate ($\dot{\gamma}$). The measurements were performed within a shear strain rate range of 2-1000 s^{-1} .

2. EXPERIMENTAL SECTION

2.3 Experimental Results

2.3.1 Thermal Analysis by Differential Scanning Calorimetry (*DSC*)

The influence of lithium salts as well as oxides on the thermal properties of non-aqueous and polymer electrolytes were studied using differential scanning calorimetry (*DSC*).

Figure 2.5(a) and Figure 2.5(b) show the DSC thermograms of the ‘pure’ DMSO solvent and DMSO consisting of lithium salts (LiCl and LiClO₄). In Figure 2.5(a) en-

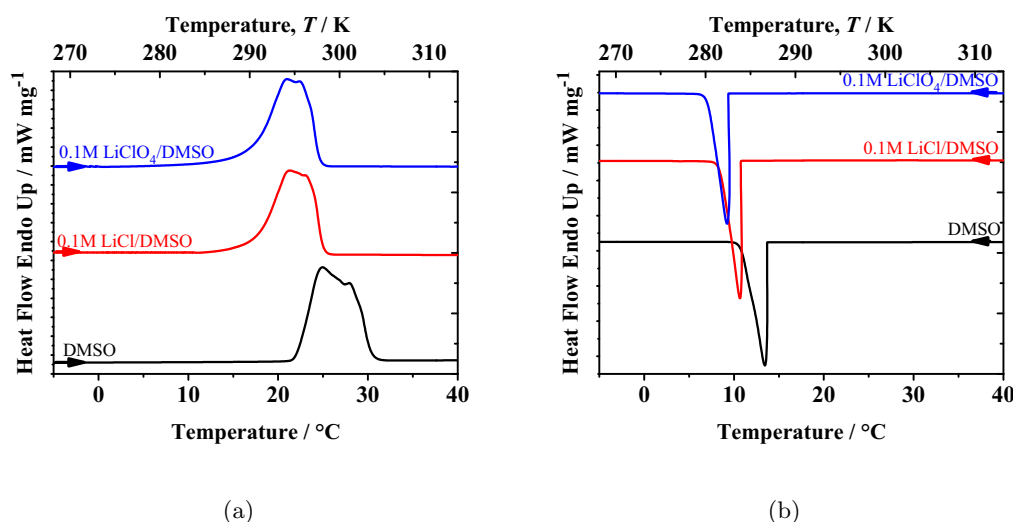


Figure 2.5: DSC thermogram for DMSO, 0.1M LiCl/DMSO and 0.1M LiClO₄/DMSO electrolytes ((a) heating from -100°C till 100°C ; (b) cooling from 100°C till -100°C).

dothermic processes are observed on heating between 13.0°C and 31.6°C . In the case of ‘pure’ DMSO a broad peak around 24.9°C , for 0.1M LiCl/DMSO at around 21.2°C and for 0.1M LiClO₄/DMSO around 20.9°C , corresponds to the melting transition, were observed. In Figure 2.5(b) exothermic processes are shown that occur upon cooling between 6.1°C and 13.8°C . ‘Pure’ DMSO solidifies at about 13.5°C , whereas solidification for 0.1M LiCl/DMSO and 0.1M LiClO₄/DMSO occurs at 10.7°C and 9.1°C , respectively.

Figure 2.6(a) and Figure 2.6(b) show the thermal properties of the various LiClO₄ concentrations using PEG-150 and PEG-350 as solvents. One can see that in most cases endothermic events are present on heating between -44.7°C and -24.7°C (Fig. 2.6(a)). For ‘pure’ PEG-150 the peak appears at about -29.1°C , for 0.01M LiClO₄/PEG-150 at

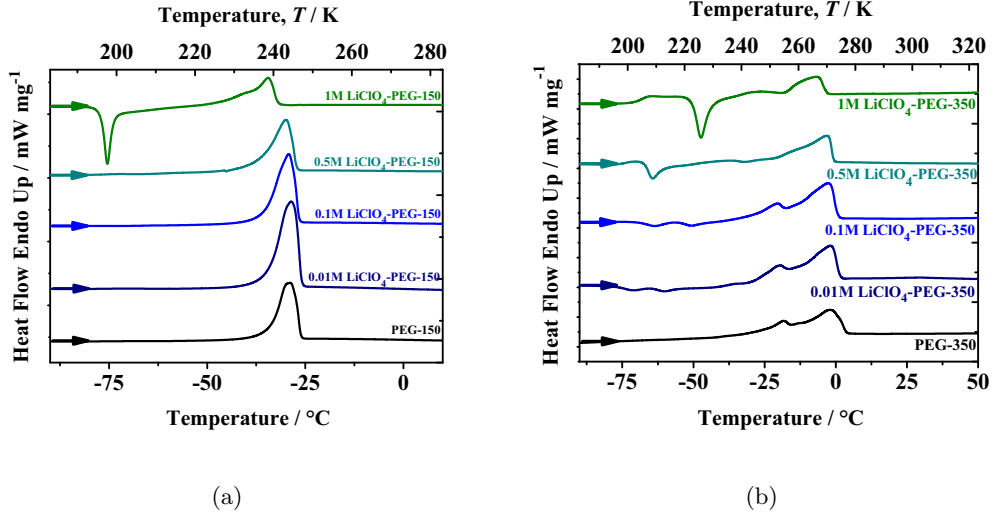


Figure 2.6: DSC thermograms for systems consisting of (a) PEG-150; (b) PEG-350 and electrolytes with different concentration of LiClO_4 (0.01M-1M), for heating from -100°C till 100°C .

about -28.8°C , for $0.1\text{M LiClO}_4/\text{PEG-150}$ at about -29.2°C , for $0.5\text{M LiClO}_4/\text{PEG-150}$ at about -29.6°C and for $1\text{M LiClO}_4/\text{PEG-150}$ at about -34.6°C , which corresponds to melting. In the case of the highest concentration of LiClO_4 (1M) one can notice an exothermic event at about -75.4°C which corresponds to the crystallization of the composite. According to the literature, the poly(ethylene glycol) chains have a tendency to crystallize upon addition of the Li-salt, which is even more pronounced in the case of PEG-350 (Fig. 2.6(b)), where an exothermic peak appears already at lower concentration (0.5M) of LiClO_4 (60, 61). This kind of behaviour is also present in polymers (62).

Figure 2.7(a) displays the influence of addition of SiO_2 ($\varphi = 0.01$ i.e. 1% by volume; 7nm-fumed and 10nm) to $1\text{M LiClO}_4/\text{PEG-150}$ electrolyte with respect to the thermal properties. Figure 2.7(c) describes the influence of higher volume fraction ($\varphi = 0.03$) of SiO_2 . Upon the addition of the oxides, the DSC profile of the sample remains unchanged apart from slight shifts in the values of the glass transition temperature (T_g), crystallization temperature (T_c) and melting temperature (T_m). Table 2.3 summarizes the values of thermal transition observed for those samples. One can see that due to the presence of 10nm silica in ‘pure’ PEG-150, melting as well as solidification started

2. EXPERIMENTAL SECTION

Table 2.3: Thermal properties of PEG-150, 1M LiClO₄/PEG-150 and the influence of SiO₂ particles on the mentioned systems.

PEG-150		1M LiClO ₄ /PEG – 150			
heating	cooling	heating			cooling
T _m /°C	T _s /°C	T _g /°C	T _c /°C	T _m /°C	T _s /°C
-29.1	-44.1	-92.7	-75.4	-34.6	-61.0
PEG – 150 : SiO ₂		1M LiClO ₄ /PEG – 150 : SiO ₂			
<i>SiO₂ (7nm-fumed); φ=0.01</i>					
-29.4	-40.7	-90.7	-74.2	-34.2	-60.5
<i>SiO₂ (7nm-fumed); φ=0.03</i>					
-	-	-92.3	-71.7	-31.7	-54.9
<i>SiO₂ 10nm; φ=0.01</i>					
-26.2	-47.1	-90.4	-68.9	-34.5	-58.5
<i>SiO₂ 10nm; φ=0.03</i>					
-	-	-91.2	-69.9	-30.6	-54.8

Table 2.4: Thermal properties of PEG-350, 1M LiClO₄/PEG-350 and the influence of SiO₂ particles on the mentioned systems.

PEG-350		1M LiClO ₄ /PEG – 350			
heating	cooling	heating			cooling
T _m /°C	T _s /°C	T _g /°C	T _c /°C	T _m /°C	T _s /°C
-2.0	-13.1	-65.8	-47.9	-6.8	-35.2
PEG – 350 : SiO ₂		1M LiClO ₄ /PEG – 350 : SiO ₂			
<i>SiO₂ (7nm-fumed); φ=0.01</i>					
-1.4	-16.2	-64.4	-44.2	-7.1	-34.2
<i>SiO₂ 10nm; φ=0.01</i>					
-1.3	-11.9	-62.2	-39.4	-6.8	-37.9

at higher temperature. This behaviour is slightly different in the case of samples consisting of 7nm-fumed silica, where melting started at almost the same temperature (-29.4°C) as that of 'pure' PEG-150 (-29.1°C) and solidification started much earlier (-40.7°C) compared to 'pure' PEG-150 (-44.1°C). However, more significant differences can be observed in the case of electrolyte, where due to presence of silica the glass transition temperature and melting shifted up to higher temperatures. Figure 2.6(b) and Figure 2.7(b) present similar influence of different concentration of LiClO_4 and the oxides presence in PEG-350.

In Figure 2.6(b) one can observe the influence of LiClO_4 concentration on the thermal properties of PEG-350 and Table 2.4 consists of the values obtained for those samples.

The above results show the different thermal properties of lithium salt type (LiCl and LiClO_4 in the case of DMSO), of various concentration of LiClO_4 (in the cases of PEGs) with or without oxide fillers. Increasing salt concentration leads to lower melting/solidifying temperatures. As to the effects of SiO_2 admixed in the composite electrolytes: addition slightly decreased glass transition temperature, crystallization temperature, melting/solidifying temperature.

2. EXPERIMENTAL SECTION

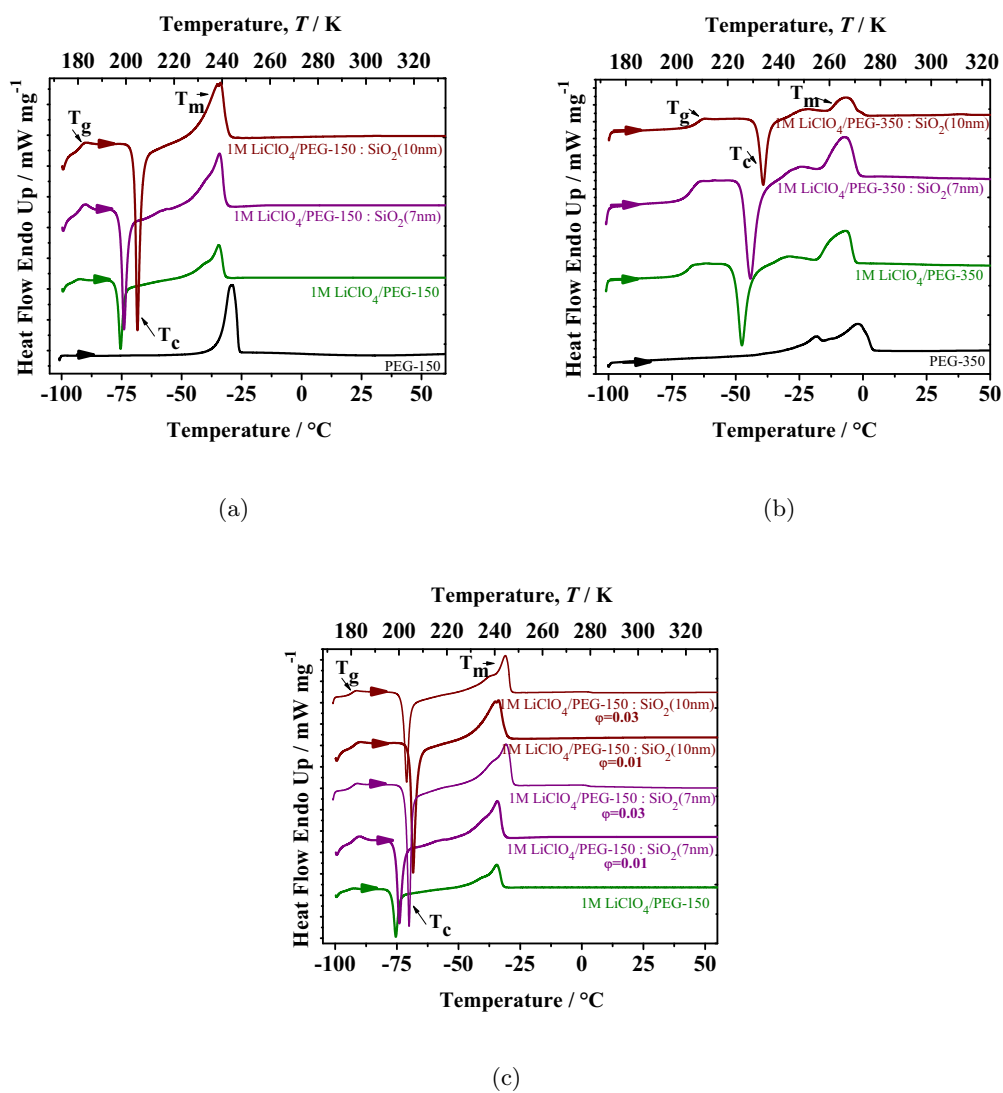


Figure 2.7: DSC thermograms for systems consisting of (a) PEG-150 and 1M LiClO₄/PEG-150 with dispersed SiO₂ (7nm-fumed, 10nm); (b) PEG-350 and 1M LiClO₄/PEG-350 with dispersed SiO₂ (7nm-fumed, 10nm); (c) 1M LiClO₄/PEG-150:SiO₂ (7nm-fumed, 10nm; low and high volume fraction), for heating from -100°C till 100°C.

2.3.2 Ionic Conductivity

2.3.2.1 Methodology Of Equivalent Circuit Modelling

Once collected the impedance data were fitted with equivalent circuit models, as mentioned earlier (Subsect. 2.2.4). To obtain the mathematical values of the circuit elements a *Complex Non-Linear Least Square (CNLS)* fitting technique was utilized. This is a non-linear least square fit of real and imaginary part (or magnitude and the phase angle) as a function of frequency to the circuit elements of an equivalent circuit. The ionic conductivity of the electrolytes was measured using AC-impedance spectroscopy in the frequency range from 10^{-1} Hz to 10^6 Hz with voltage amplitudes of 0.1 V (Solartron 1260 frequency analyser). The samples were placed between two parallel gold electrodes of a home-built cell. This cell was immersed in a stainless steel container, placed in RC6CP Lauda thermostat (containing 1:1 water and polyethylene glycol mixture) as shown on Figure 2.8.

The impedance data acquisition and the equivalent circuit modelling of the impedance data was done using software 'ZPlot' and 'ZView2', respectively from Scribner Associates Inc.

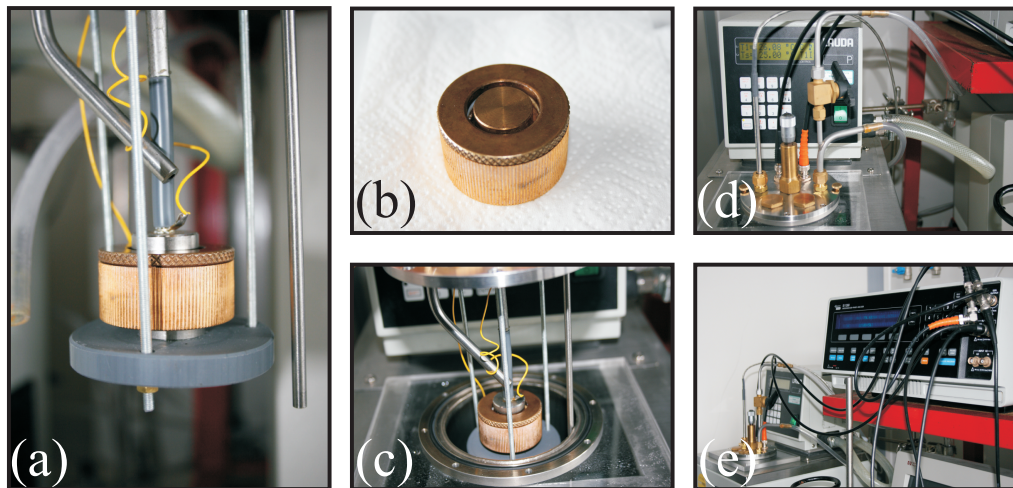


Figure 2.8: The home-built system used for the conductivity measurements. (a) cell immersed in a stainless steel contacts, (b) tightly closed home-built cell filled with the sample, (c) cell put inside a stainless steel container which is placed in RC6CP Lauda thermostat, (d) tightly closed container is under argon flow during the whole measurement, (e) general overview on the working system.

2. EXPERIMENTAL SECTION

Impedance Measurements on PEG-350/LiClO₄ system

One representative example for the analysis of the impedance measurements of the polymer electrolytes consisting of PEG-350, LiClO₄ and SiO₂, measured between 10°C to 60°C is shown in Figure 2.9. In the frequency range of 10⁴ Hz and 10⁶ Hz the phase angle almost becomes zero (< 1°). The Nyquist diagram for the corresponding Bode diagram is shown in Figure 2.10(a) and in Figure 2.10(b).

Equivalent circuit analysis

The equivalent circuit that well describes the impedance behaviour is shown in Figure 2.11 and consists of R₁-C₁ and R₂-CPE circuits in series. More accurately the second capacitor is a non-ideal circuit element, a so-called constant phase element (*CPE*). The analysis clearly shows that the left R₁-C₁ circuit maps the electrolyte impedance giving rise to a high frequency semicircle, while the right one is associated with interfacial blocking. From the left circuit characterized by R₁ and C₁ electrolyte bulk conductivity and dielectric constant follow as

$$\sigma = \frac{1}{R_1} \cdot \frac{h}{A}, \quad \varepsilon = (C_1 \cdot \frac{h}{A})/\varepsilon_0 \quad (2.14)$$

where h is the thickness of sample (distance between electrodes) and A the area of sample (area of the electrodes). The quantity $h \cdot A^{-1}$ is the cell constant (k) which was calculated from its geometry and compared with results obtained during calibration. The cell was calibrated following the method of Fuoss and co-workers (63). This involved the use of aqueous potassium chloride solutions in the concentration range 0.01N to 1N. The cell constant was determined to be 0.1283 cm⁻¹. Calculated ionic conductivities were measured as a function of various parameters (such as temperature, oxides and solvents type, concentration and time) and are discussed below.

Table 2.5 gives typical values for R₁, C₁, R₂, CPE as well as σ and ε .

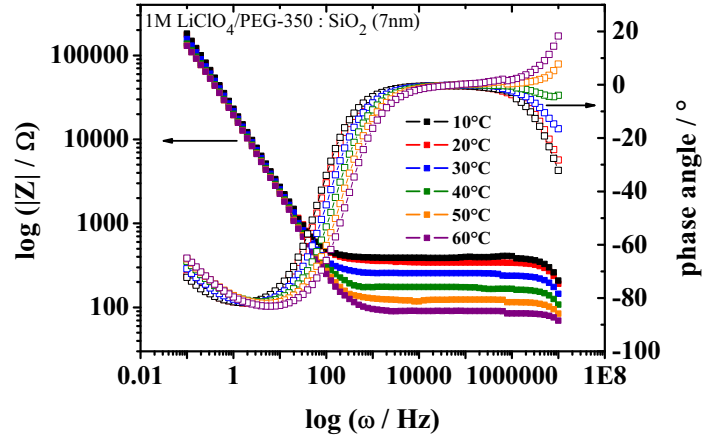


Figure 2.9: Bode diagram of 1M LiClO₄/PEG – 350 : SiO₂(7nm-fumed, $\varphi = 0.01$), measured between 10°C to 60°C.

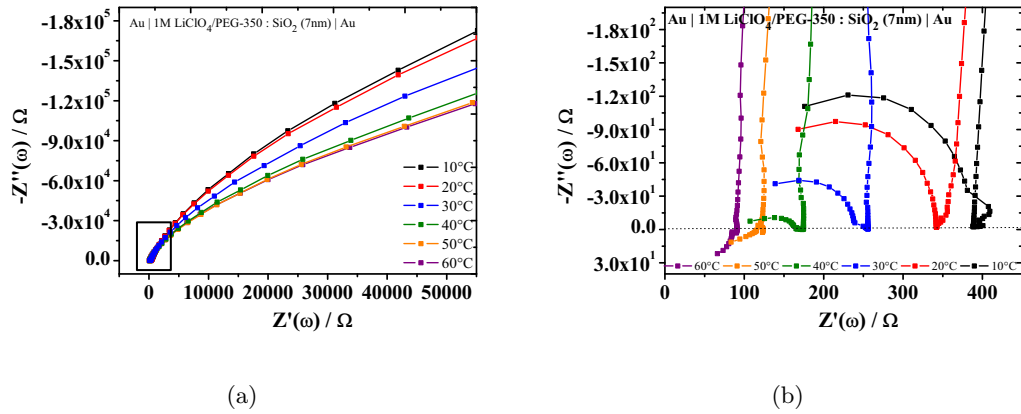


Figure 2.10: Nyquist diagram of 1M LiClO₄/PEG – 350 : SiO₂(7nm-fumed, $\varphi = 0.01$), measured between 10°C to 60°C, (b) zoomed semi-circles.

2. EXPERIMENTAL SECTION

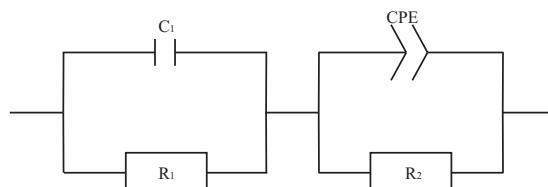


Figure 2.11: Proposed equivalent circuit consisting of two resistors, R_1, R_2 and one constant phase element, CPE.

Table 2.5: Fitting parameters for the equivalent circuit elements for 1M $\text{LiClO}_4/\text{PEG} - 350 : \text{SiO}_2$, where Q° is numerical value of the admittance at $1 \text{ rad} \cdot \text{s}^{-1}$ and z is CPE parameter between 0 and 1.

1M $\text{LiClO}_4/\text{PEG} - 350 : \text{SiO}_2$ (7nm-fumed)							
$T/^\circ\text{C}$	R_1/Ω	R_2/Ω	C_1/F	CPE		$\sigma/\text{S} \cdot \text{cm}^{-1}$	ϵ
				$Q^\circ/\Omega^{-1} \cdot \text{s}^{1-z}$	z		
10	388.5	722040	8.96e-11	7.757e-6	0.9441	3.303e-4	13.0
20	340.6	735630	1.13e-10	7.984e-6	0.9367	3.767e-4	16.4
30	253.3	488090	2.77e-10	8.381e-6	0.9428	5.065e-4	40.2
40	174.2	363400	1.118e-9	9.298e-6	0.9386	7.365e-4	162.0
50	120.2	320630	9.118e-8	8.371e-6	0.9418	10.67e-4	1.3e+5
60	91.08	307830	7.675e-6	9.348e-6	0.9467	14.09e-4	1.1e+7

2.3.2.2 Ionic Conductivity Results

(a) Conductivity as a function of temperature

The measured conductivities of Li^+ ions in DMSO (dielectric constant, $\varepsilon = 46.7$ at $T = 25^\circ\text{C}$ (47)) using different volume fraction (φ) of SiO_2 (300nm) are shown in Figure 2.12. One can see that for all electrolytes ('filler free' liquid electrolyte and

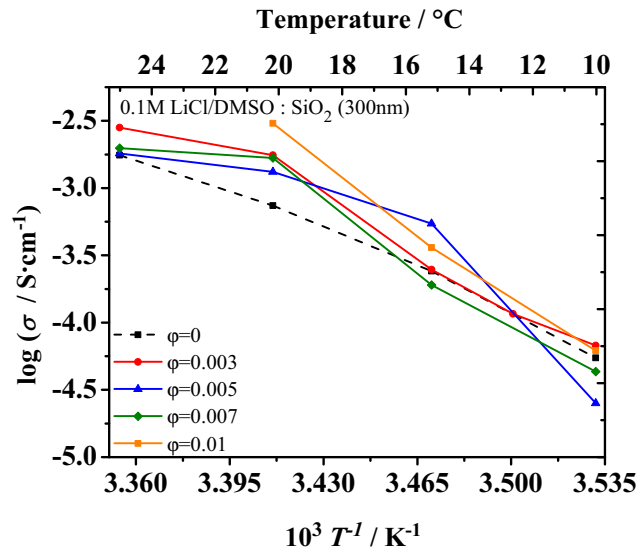


Figure 2.12: Changes in the ionic conductivity as a function of temperature for 0.1M $\text{LiCl/DMSO} : \text{SiO}_2$ (300nm) composite electrolytes, consisting of different volume fraction (φ) of oxide particles, measured between 10° to 25°C .

composite electrolyte), the ionic conductivity increased with temperature. One can conclude that the presence of SiO_2 in the liquid electrolyte consisting of LiCl and DMSO , improves the ionic conductivity in a wider temperature regime, not just at room temperature. In the Figures 2.13(a) and 2.13(b), the influence of two different types of SiO_2 (7nm-fumed and 10nm) on the conductivity of lithium salt polymer electrolytes is seen. Two polymer solvents (PEG-150, $\varepsilon = 23.9$ and PEG-350, $\varepsilon = 25.2$ at $T = 25^\circ\text{C}$) were used. The conductivities for 1M $\text{LiClO}_4/\text{PEG-150}$ were found to be between $3.1 \times 10^{-4} - 2.7 \times 10^{-3} \text{ S}\cdot\text{cm}^{-1}$ at temperatures between $5-70^\circ\text{C}$, whereas for 1M $\text{LiClO}_4/\text{PEG-350}$ the values were between $6.7 \times 10^{-5} - 3.1 \times 10^{-4} \text{ S}\cdot\text{cm}^{-1}$ at the same temperature range. As before, one can notice that addition of SiO_2 improved

2. EXPERIMENTAL SECTION

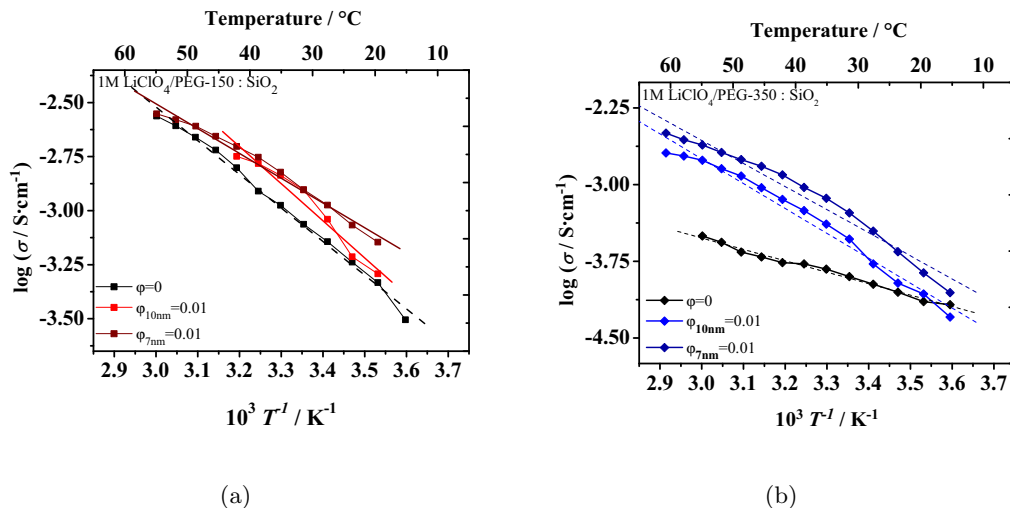


Figure 2.13: Changes in the ionic conductivity as a function of temperature for (a) 1M $\text{LiClO}_4/\text{PEG} - 150 : \text{SiO}_2$; (b) 1M $\text{LiClO}_4/\text{PEG} - 350 : \text{SiO}_2$, (7nm-fumed and 10nm) composite electrolytes, consisting of one volume fraction ($\varphi = 0.01$) of oxide particles, measured between 10°C to 60°C. Dashed lines are fitted to the Arrhenius equation.

the conductivity in the entire temperature regime for both types of silica. The electrolytes consisting of SiO_2 (7nm-fumed), showed higher conductivity for all measured temperatures, probably due to the greater surface area (smaller particles size). The complicated and not completely reproducible temperature dependences point towards network morphology variations. Network complications are particularly obvious in Figure 2.13(b) indicating complex oxide/electrolyte interactions in the direction of lyophilic interactions.

(b) Conductivity: Comparison of different types of oxides and solvents

To verify the influence of different oxides on the ionic conductivity, composite electrolytes containing a number of oxide particles, such as SiO₂ – 7nm-fumed; 11nm-fumed; 300nm; mesoporous (MCM-41); γ – Al₂O₃ and sulfonated ZrO₂ were used. In Figure 2.14(a) and Figure 2.14(b) one recognises variations in the conductivity even at low concentrations of oxides ($\varphi = 0.015$ or $\varphi = 0.01$). One can conclude that addition of low concentration of silica oxides had no effect on systems containing DMSO (this was not unexpected due to the high dielectric constant). More pronounced increases in conductivity were noticed in the case of sulfonated ZrO₂. Unfortunately, composites containing ZrO₂ were not stable at higher volume fraction because of strong agglomeration and sedimentation. In the case of the systems containing PEG-150 or PEG-350 SiO₂ effected a stronger increase on the conductivity.

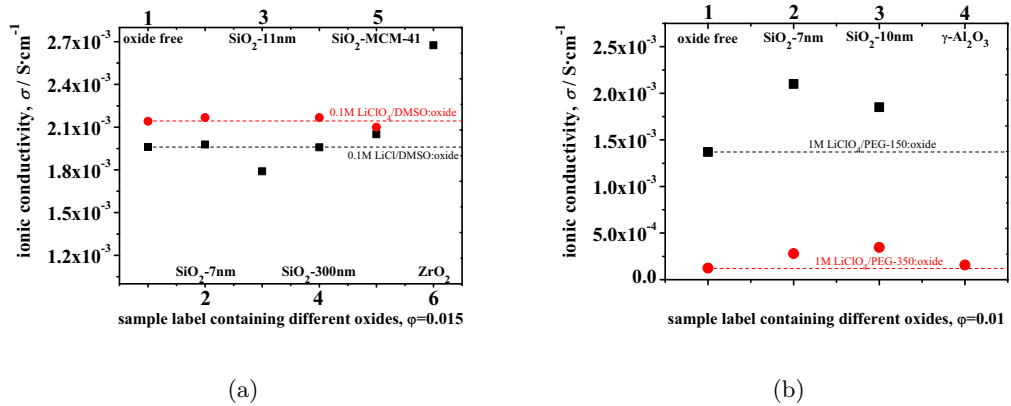


Figure 2.14: Changes in the ionic conductivity in (a) 0.1M LiClO₄/DMSO and in 0.1M LiCl/DMSO and (b) 1M LiClO₄/PEG – 150 and 1M LiClO₄/PEG – 350 electrolytes depend on various oxide particles at the same concentration ((a) $\varphi = 0.015$ and (b) $\varphi = 0.01$), measured at T = 25°C. Dashed lines emphasise the ionic conductivity of ‘filler-free’ electrolytes.

2. EXPERIMENTAL SECTION

(c) Conductivity as a function of salt concentration

The conductivity was also measured as a function of different LiClO_4 concentrations in systems containing low concentration of SiO_2 (7nm-fumed, $\varphi = 0.01$). Intentionally, the same volume fraction was considered for quite unlike solvents such as non-aqueous, DMSO and polymer, PEG-150. In Figure 2.15 one can observe higher conductivity values for all composite electrolytes in comparison to ‘filler-free’ electrolytes. It is important to mention that a more pronounced increase was observed for higher lithium salt molarities. This effect can be explained by an increased fraction of ion pairs at higher total concentration.

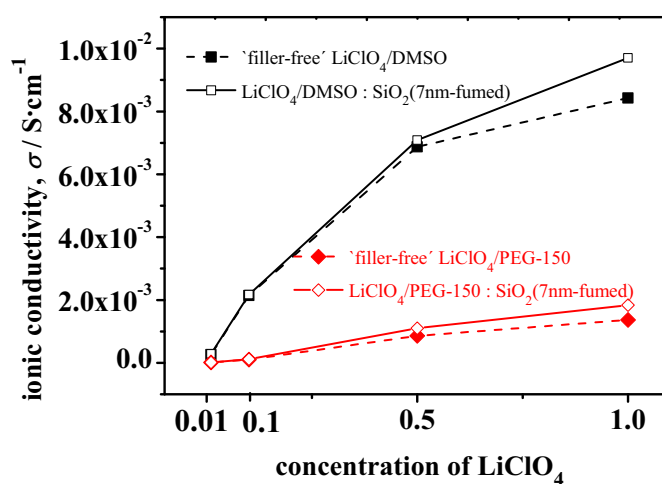
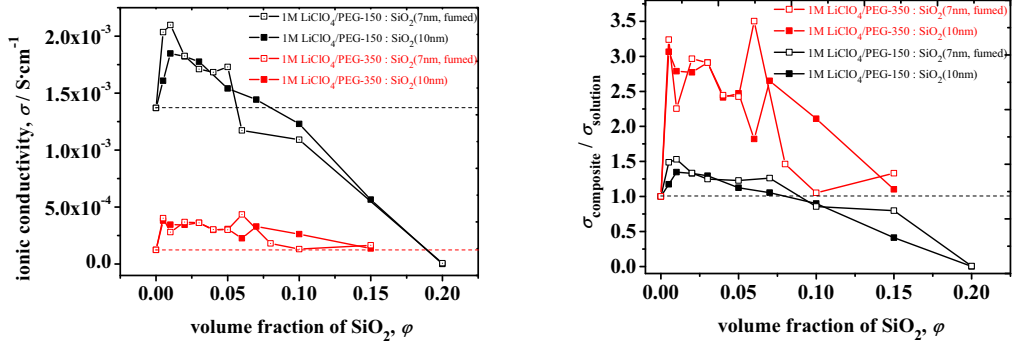


Figure 2.15: Changes in the ionic conductivity in $\text{LiClO}_4/\text{DMSO}$ and in $\text{LiClO}_4/\text{PEG} - 150$ electrolytes due to changes in concentration of LiClO_4 in presence (closed symbols) and absence (open symbols) of SiO_2 (7nm-fumed, $\varphi = 0.01$), measured at $T = 25^\circ\text{C}$.

(d) Conductivity as a function of oxide volume fraction

On the basis of the aforementioned results (Paragraphs a, b, c), a favourable solvent to verify the influence of salt and oxide parameters should be the low molecular weight liquid polymers PEG-150 and PEG-350. Here viscosity and dielectric constant offer the right compromise to still see enhancement effects but to have a sufficient network stability. The influence of volume fraction of nano-size oxide particles in polymer electrolytes is presented in Figure 2.16(a). In both cases, where SiO₂ was incorporated into the electrolyte, higher values of conductivity were obtained compared to ‘filler-free’ electrolytes. One can notice that the conductivity reaches a maximum value and then quickly decreases already at low φ -values. Figure 2.16(b), displays the relative increase



(a) Conductivity vs. SiO₂ volume fraction

(b) Relative increase in conductivity vs. SiO₂ volume fraction

Figure 2.16: (a) changes in the ionic conductivity in 1M LiClO₄/PEG – 150 and in 1M LiClO₄/PEG – 350 electrolytes, (b) changes in conductivity relative increase of the same systems, depend on increased volume fraction of SiO₂ (7nm-fumed and 10nm), measured at T = 25°C.

of the conductivity for the same systems. Because the dielectric constants for PEG-150 and PEG-350 are very close and the viscosity values for bulk and boundary are also expected to be the same for a given solvent, one would expect a similar enhancement. Figure 2.16(b) indeed shows that the enhancement is on the same order of magnitude unlike the absolute value. That PEG-350 shows an even higher enhancement may be due to the network blocking that is obvious for PEG-150 at higher volume fractions (Fig. 2.16(a)).

2. EXPERIMENTAL SECTION

(d) Conductivity as a function of time

Of a great significance is the time dependence (before the stationary values are achieved that are to be or have been discussed in the other sections) as this reveals degree and rate of the network coarsening. Changes in conductivity as a function of time were considered for the following situations: **(1)** different oxide sizes; **(2)** different volume fractions as well as **(3)** various solvent viscosities.

In Figure 2.17 one can observe that for both PEG as well as DMSO the ionic conductivity decreases with time. The steady state conductivity was reached after circa 1 h. This decrease was steeper and more significant in the case of bigger particles.

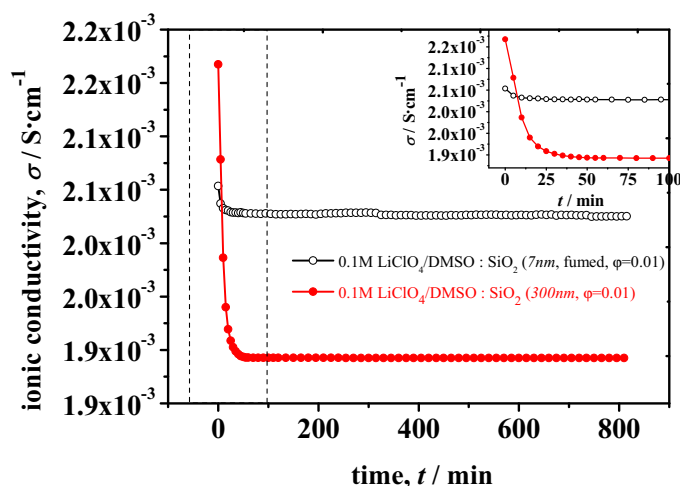


Figure 2.17: Changes in the ionic conductivity as a function of time for 0.1M LiClO₄/DMSO : SiO₂ consisting of two different size SiO₂ (7nm-fumed and 300nm), measured at T = 25°C. The inset shows the σ vs. time for 100 min.

The influence of different oxide volume fractions – at low values (“colloidal” regime) and high values (gel-solid regime) – on the conductivity as a function of time was also considered. In Figure 2.18 one observes a significant difference in the conductivity, which decreases with time. This decrease is stronger for systems with low oxide volume fraction and not so pronounced for the more packed system, containing a higher fraction of oxide particles. The systems with solvents of different viscosities were also studied.

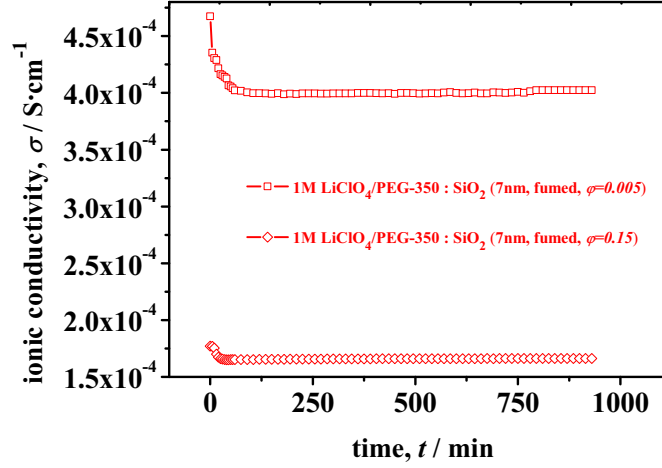


Figure 2.18: Changes in the ionic conductivity as a function of time of one system 1M LiClO₄/PEG – 350 : SiO₂ consists of different volume fraction of SiO₂ (7nm-fumed) – $\varphi = 0.005$ and $\varphi = 0.15$, measured at T = 25°C.

Figure 2.19 presents the comparison between three systems in DMSO with different molarities of lithium salt. In Figure 2.20 one can observe the conductivity changes as a function of time for the 1M LiClO₄/PEG : SiO₂ (10nm) system using PEG-150 ($\eta = 0.0132 \text{ Pa} \cdot \text{s}$ at $\dot{\gamma} = 500 \text{ s}^{-1}$) and PEG-350 ($\eta = 0.101 \text{ Pa} \cdot \text{s}$ at $\dot{\gamma} = 500 \text{ s}^{-1}$), respectively. The time dependence can be characterized by the difference between the stationary value and the initial value ($\delta\sigma$) as well as by a time constant. It was found that $\delta\sigma$ increases with decreasing viscosity of the solvent. The relaxation time, however, is roughly constant in all the experiments, under all conditions at room temperature ($\sim 1 \text{ h}$) but we also notice that this relaxation time decreases with increasing temperature (around 2.5-3 hours for 10°C and around 25 minutes at ($\sim 35^\circ\text{C}$)).

2. EXPERIMENTAL SECTION

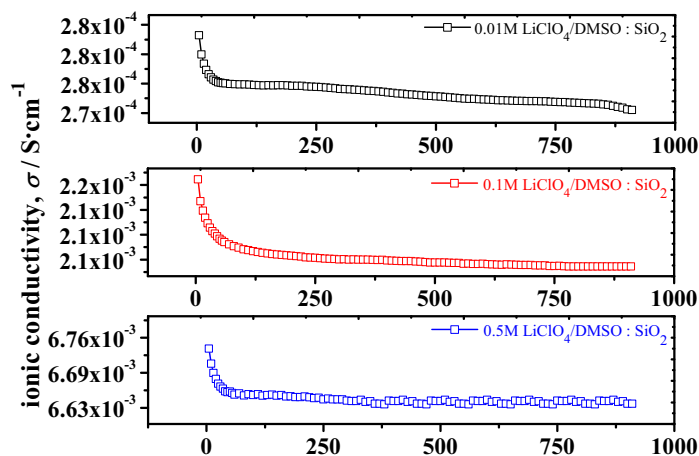


Figure 2.19: Ionic conductivity as a function of time for 0.01M $\text{LiClO}_4/\text{DMSO} : \text{SiO}_2$ ($\eta = 0.00662 \text{ Pa}\cdot\text{s}$ at $\dot{\gamma} = 500 \text{ s}^{-1}$), 0.1M $\text{LiClO}_4/\text{DMSO} : \text{SiO}_2$ ($\eta = 0.00796 \text{ Pa}\cdot\text{s}$ at $\dot{\gamma} = 500 \text{ s}^{-1}$) and 0.5M $\text{LiClO}_4/\text{DMSO} : \text{SiO}_2$ ($\eta = 0.00986 \text{ Pa}\cdot\text{s}$ at $\dot{\gamma} = 500 \text{ s}^{-1}$) containing of $\varphi = 0.01$ of SiO_2 (7nm-fumed), measured at $T = 25^\circ\text{C}$.

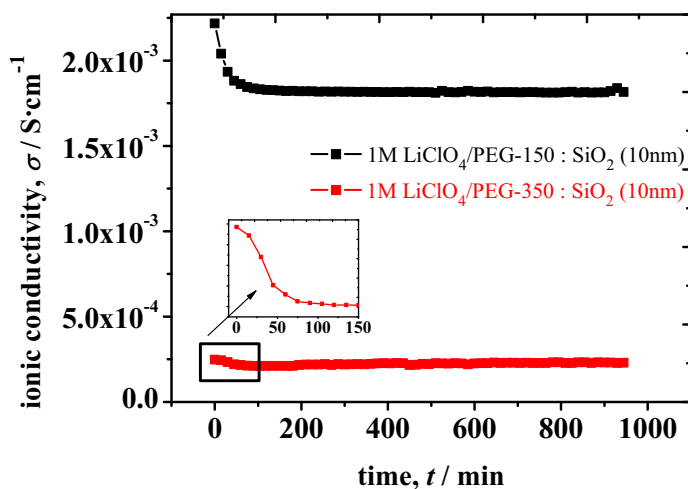


Figure 2.20: Changes in the ionic conductivity as a function of time for 1M $\text{LiClO}_4/\text{PEG} - 150 : \text{SiO}_2$ and 1M $\text{LiClO}_4/\text{PEG} - 350 : \text{SiO}_2$ contain of one volume fraction of SiO_2 (10nm); $\varphi = 0.01$, measured at $T = 25^\circ\text{C}$.

2.3 Experimental Results

Assuming that we have exponential dependencies, the plot $\ln\left(\frac{\sigma(t)-\sigma(t=\infty)}{\sigma(t=0)-\sigma(t=\infty)}\right)$ as a function of time (see Fig. 2.21) should give the time constant as negative inverse slop. The time dependencies are in the span shown in Figure 2.21 and hence range between 10 and 20 minutes.

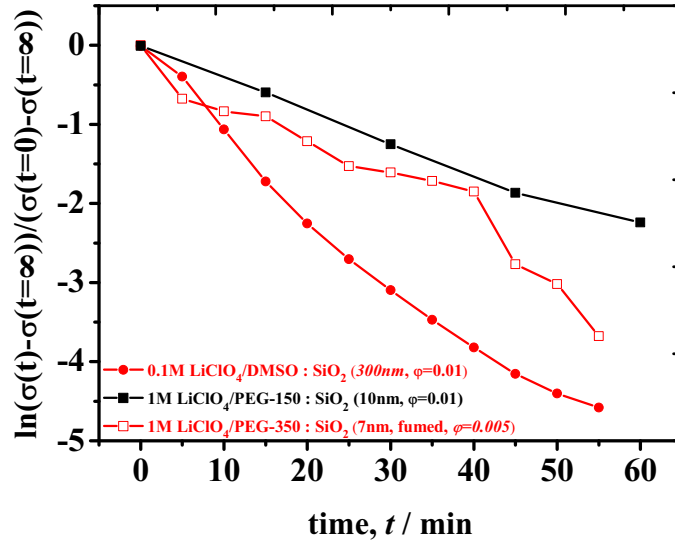


Figure 2.21: Relative conductivity changes as a function of time for composites presenting pronounced difference between stationary and initial value $\delta\sigma$ (for 0.1M LiClO₄/DMSO : SiO₂ (300nm), 1M LiClO₄/PEG – 150 : SiO₂ (10nm) and 1M LiClO₄/PEG – 150 : SiO₂ (7nm-fumed)), measured at T = 25°C. The time constants range between 10 min and 20 min.

2. EXPERIMENTAL SECTION

Sedimentation

The above presented time dependent results were obtained after around 12 hours. After more than two days one could observe in various cases that most of the coarsened particles settle down, i. e. sediment (see Fig. 2.22). Let us consider sedimentation for

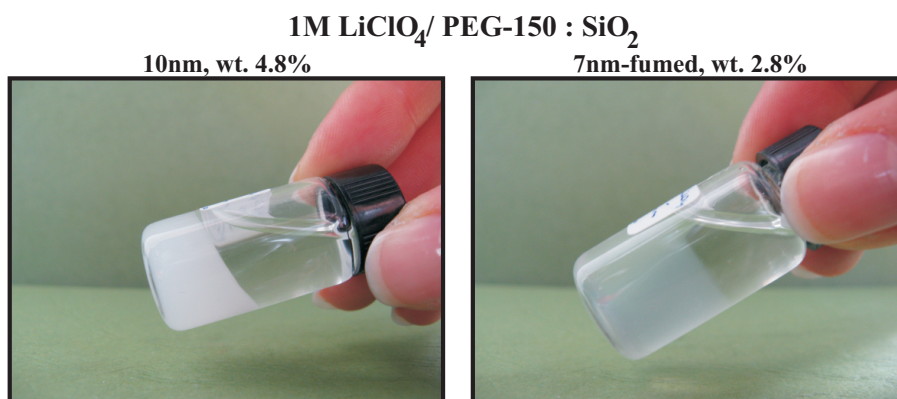


Figure 2.22: Sedimentation effect observed after two days from preparation on 1M LiClO₄/PEG – 150 : SiO₂, 7nm-fumed and 10nm.

an uncharged, single particle of mass m and specific volume v in a liquid of density ρ . The driving force on the particle, which is independent of particle shape or solvation is $m(1 - v\rho)g$, where g is the acceleration of gravity. The factor $(1 - v\rho)$ takes account of the buoyancy. The liquid medium offers a resistance to the particle motion which increases with increasing velocity (30). The sedimentation velocity is given by balancing the frictional drag of the solvent with the gravitational force. For spherical particles of radius r in a solvent with a viscosity η one has to formulate (30, 59):

$$\Delta\rho\frac{4}{3}\pi r^3 g = \nu 6\pi\eta r \quad (2.15)$$

where $\Delta\rho$ is the density difference between the particles and the medium. By simple rearrangement the sedimentation velocity ν follows as

$$\nu = \frac{2\Delta\rho gr^2}{9\eta} \quad (2.16)$$

The derivations of Stokes' law assumes that (30):

1. The spherical particles move slowly.

2. The liquid medium (solution or suspension) is strongly dilute.
3. The liquid medium is continuous compared with the dimensions of the particles (valid for the motion of colloidal particles since their size is not comparable with the molecules constituting the liquid medium).

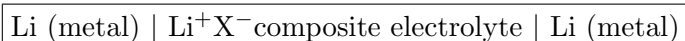
The colloidal systems' sedimentation profiles are affected by many factors. In a system unstable to flocculation and sedimentation, one has to distinguish between: **(1)** flocculation followed by sedimentation, **(2)** sedimentation followed by flocculation in the sediment, and **(3)** simultaneous flocculation and sedimentation (59). In this work the detailed mechanism, however, was not important and not further elucidated.

2. EXPERIMENTAL SECTION

2.3.3 Transference number

2.3.3.1 Method

The Li^+ ion mobility (*transference number*, t_+) of non-aqueous and polymer composite electrolytes was determined using a special variant of the Hebb – Wagner – Yokota polarization technique, according to the approach by Evans and co-workers (64, 65, 66, 67, 68). Here at the Li-electrodes the blocking of the anions is due to the non-reversibility of the electrodes for the anions. The blocking occurs even more effectively as a consequence of a selective passivation layer formed at the lithium/electrolyte interface in a symmetrical cell of the type:



For an electrolyte that contains a salt, which dissociates to given single cationic and anionic species, the electric transport number, t_+ is defined as the fraction of the total electric current carried in the solution:

$$t_+ = \frac{i_+}{(i_+ + i_-)} = \frac{i_+}{i} \quad (2.17)$$

where i_+ and i_- are the partial currents carried by cations and anions respectively, and i is the total current. As the transport is driven only by the electric field and as both ions perceive the same electric field, t_+ can also be written in terms of conductivities

$$t_+ = \frac{\sigma_+}{(\sigma_+ + \sigma_-)} = \frac{\sigma_+}{\sigma} \quad (2.18)$$

If the electrodes were completely reversible for anion and cation a constant current I would develop on applying a constant voltage V with the conductivity being available from

$$\sigma = \frac{I \cdot k}{\Delta V} \quad (2.19)$$

(k : cell constant)

As the electrodes are only reversible for the cation but block the anion, this equation only holds for the situation directly after switching on the voltage

$$\sigma = \frac{I_{(t=0)} \cdot k}{\Delta V} \quad (2.20)$$

2.3 Experimental Results

The blocking of the anions leads to the fact that in the steady state only the cationic current flows ($I_{(t=\infty)} = I_{+ (t=\infty)}$). Hence

$$\sigma_+ = \frac{I_{+ (t=\infty)} \cdot k}{\Delta V} \quad (2.21)$$

The comparison ($I_{(t=\infty)}/I_{(t=0)}$) yields t_+ . These considerations ignore the occurrence of additional polarization effects, the time constance of which are very short (e. g. contact impedance, impedance of passivation layers). Or in other terms the above equations still hold if ΔV is not the total applied voltage ΔU but the voltage drop only due to the bulk conductivity effects. This difference

$$\Delta V' = \Delta U - \Delta V \quad (2.22)$$

can be obtained from impedance spectroscopy.

Or formulated differently by taking account of additional resistances $R_{(t)}$:

$$I_{(t=0)} = \frac{\Delta U}{R_{(t=0)} + R_{ion}} \quad (2.23)$$

$$I_{(t=\infty)} = \frac{\Delta U}{(R_{(t=\infty)} + R_{ion}/t_+)} \quad (2.24)$$

$$t_+ = \frac{I_{(t=\infty)}(\Delta U - I_{(t=0)} \cdot R_{(t=0)})}{I_{(t=0)}(\Delta U - I_{(t=\infty)} \cdot R_{(t=\infty)})} \quad (2.25)$$

where

$$I_{(t=0)} \cdot R_{(t=0)} = \Delta V'_{(t=0)}, \quad I_{(t=\infty)} \cdot R_{(t=\infty)} = \Delta V'_{(t=\infty)} \quad (2.26)$$

(R_{ion} is the total ionic resistance in the electrolyte)

Another important point refers to the diffusivity of ion pairs. Obviously a steady state transport is possible without free Li^+ motion, namely by counter motion of LiX and X^- (LiX dissociates in Li^+ and X^- at the electrode, Li^+ transfers into the electrode and X^- migrates to the bulk). This is a special case of the concept of Conservative Ensembles, treated in References (69, 70, 71, 72) and in fact applied to the present problem in Reference (73, 74). The specific conductivity derived from $I_{(t=\infty)}$ is then not simply σ_+ but contains diffusivity contributions from the counter ion (σ_-) and the ion pair (s).

$$\sigma_{pol} = \sigma_+ + \frac{s \cdot \sigma_-}{s + \sigma_-} \quad (2.27)$$

$$= \sigma_+ + \left(\frac{1}{s} + \frac{1}{\sigma_-} \right)^{-1} \quad (2.28)$$

2. EXPERIMENTAL SECTION

where $\sigma_+ = \sigma_{\text{Li}^+}$, $\sigma_- = \sigma_{\text{X}^-}$ and $s \equiv F^2 c_{\text{LiX}} D_{\text{LiX}} / RT$. If $s = 0$ what we assume here, the above equations are valid.

2.3.3.2 Results

As seen in Figure 2.23 the current versus time polarization curves exhibit a smooth, gradual decay until the cell is polarized, after which a constant, steady state current is observed. It is important to note that the voltage has been applied after a stationary network (see previous section) has been established.

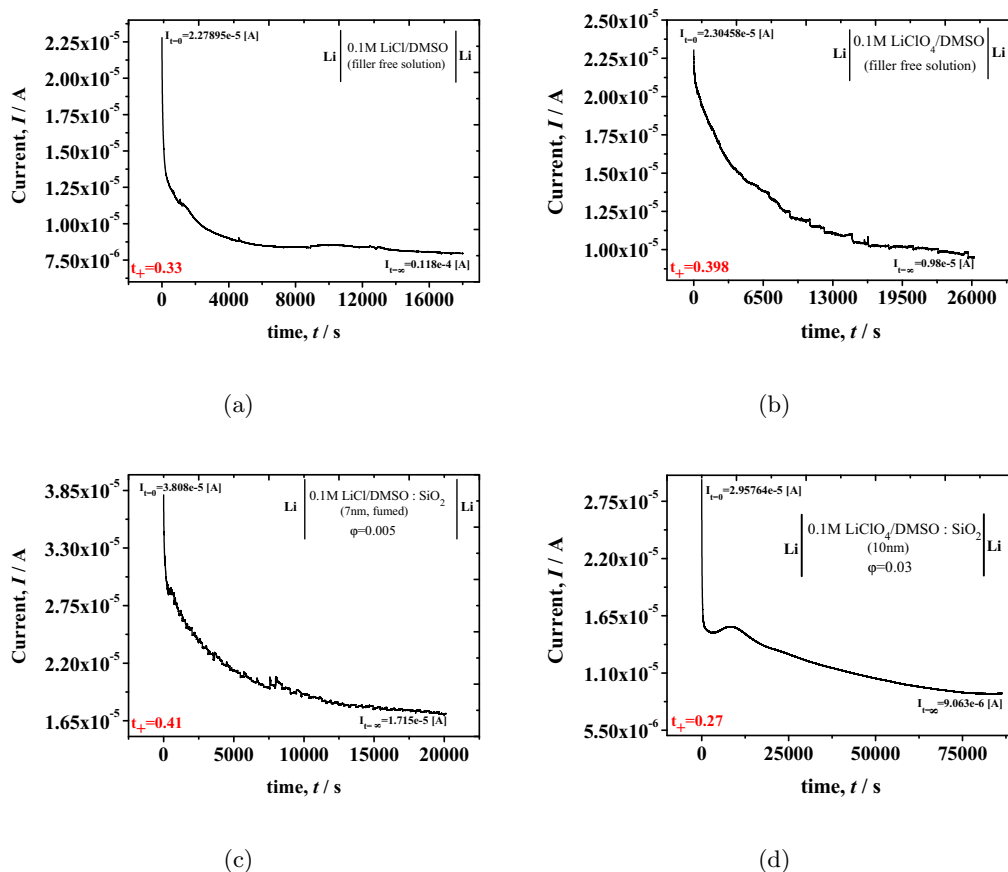


Figure 2.23: Plot of the current as a function of time. 10 mV of potential was applied across the symmetric cell, to (a) 0.1M LiCl/DMSO; (b) 0.1M LiClO₄/DMSO; (c) 0.1M LiCl/DMSO:SiO₂ (7nm-fumed; $\varphi = 0.01$); (d) 0.1M LiClO₄/DMSO:SiO₂ (10nm; $\varphi = 0.03$), at room temperature.

2.3 Experimental Results

In this section I will only discuss the results obtained for PEG-150. DMSO showed a reaction with Li perhaps catalyzed by the oxide, obvious by the yellow coloration of the electrolyte. (Table 2.6 and Table 2.7 give the apparent numbers initially decrease of t_+ for LiClO_4 and increase of t_+ for LiCl . Both results in fact are unsurprisingly inconsistent with the zeta-potential (see next Subsection 2.3.4)).

The experiments with the polymer (PEG-150) as solvent are presented in Table 2.9 and Table 2.10. These results are very consistent with zeta-potential measurements. The following results can be extracted:

1. PEG-350 exhibited lower ionic conductivity and transference number (1M LiClO_4 /PEG-350, $t_+ = 0.14$) because of viscosity.
2. The transference number increased on SiO_2 addition.
3. The effect is smaller if the packing density is increased.

2. EXPERIMENTAL SECTION

Table 2.6: Values of measured $I_{(t=0)}$, $I_{(t=\infty)}$, $R_{(t=0)}$, $R_{(t=\infty)}$ and calculated t_+ , for the investigated samples: (1) 0.1M LiCl/DMSO, (2) 0.1M LiCl/DMSO:SiO₂, 7nm-fumed; $\varphi = 0.005$, (3) 0.1M LiClO₄/DMSO, (4) 0.1M LiClO₄/DMSO : SiO₂, 10nm; $\varphi = 0.03$. 10 mV of potential was applied across the symmetric cell. All the measurements were carried out at room temperature.

Sample	$I_{(t=0)}/\mu\text{A}$	$I_{(t=\infty)}/\mu\text{A}$	$R_{(t=0)}/\Omega$	$R_{(t=\infty)}/\Omega$	t_+
(1)	22.79	7.98	36.90	43.14	0.33
(2)	38.08	17.15	45.20	52.20	0.41
(3)	23.05	9.77	42.17	40.01	0.40
(4)	29.58	9.06	60.61	61.47	0.27

Table 2.7: Values for calculated t_+ , for the investigated composite electrolytes consisting of DMSO as a solvent. 10 mV of potential was applied across the symmetric cell. All the measurements were carried out at room temperature.

Transference number, t_+				
volume fraction, φ	0.1M LiCl/DMSO:SiO ₂		0.1M LiClO ₄ /DMSO : SiO ₂	
	7nm-fumed	10nm	7nm-fumed	10nm
0	0.33		0.40	
0.005	0.41	0.36	0.20	0.23
0.01	0.31	0.34	0.32	0.28
0.02	0.27	0.18	0.16	0.38
0.03	0.21	0.16	0.07	0.27

Table 2.8: Values for calculated t_+ , for the investigated composite electrolytes consisting of PEG-150 as a solvent. 100 mV (values without * a 10 mV) of potential was applied across the symmetric cell. All the measurements were carried out at room temperature.

Transference number, t_+		
volume fraction, φ	1M LiClO ₄ /PEG – 150 : SiO ₂	
	7nm-fumed	10nm
0	0.33	
0.005	0.63*	0.64
0.01	0.51*	0.50*
0.02	0.56*	0.82*
0.03	0.26*	0.47*

2.3 Experimental Results

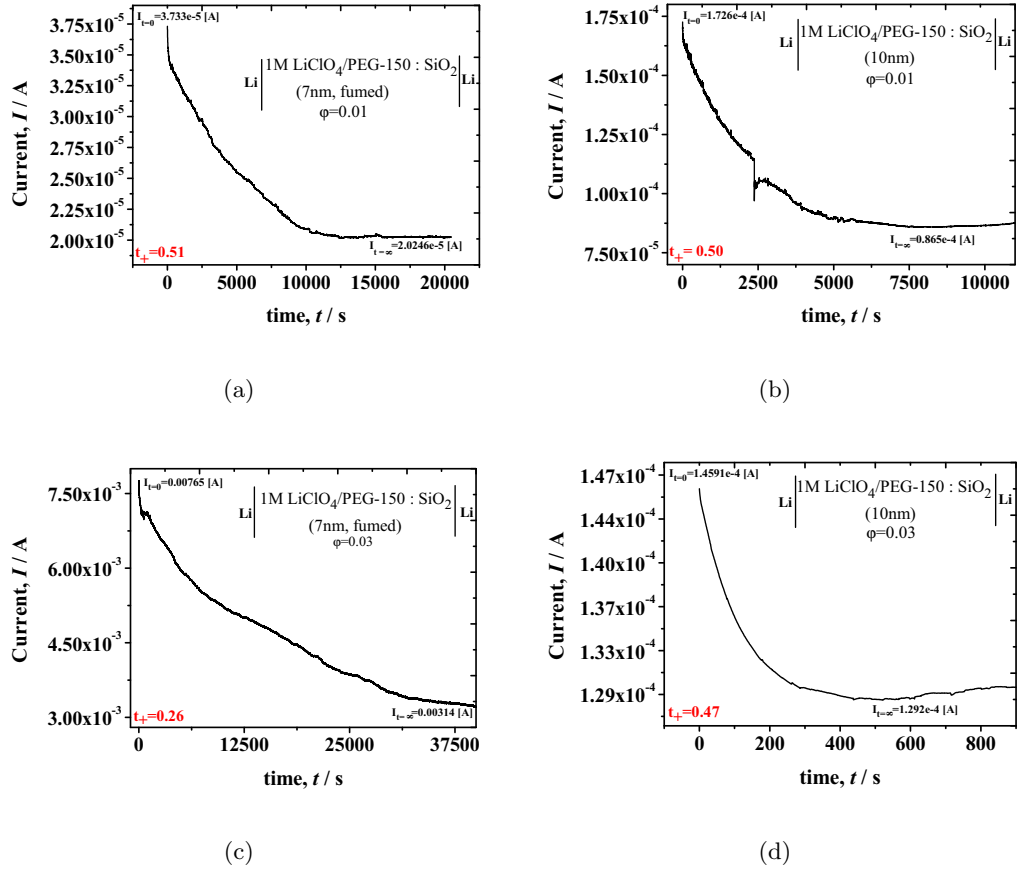


Figure 2.24: Plot of the current as a function of time. 10 mV (*, a 100 mV) of potential was applied across the symmetric cell, to (a) 1M LiClO₄/PEG – 150 : SiO₂, 7nm-fumed, $\varphi = 0.01$; (b) 1M LiClO₄/PEG – 150 : SiO₂, 10nm, $\varphi = 0.01^*$; (c) 1M LiClO₄/PEG – 150 : SiO₂, 7nm-fumed, $\varphi = 0.03^*$; (d) 1M LiClO₄/PEG – 150 : SiO₂, 10nm, $\varphi = 0.03^*$, at room temperature.

2. EXPERIMENTAL SECTION

Table 2.9: Values for measured $I_{(t=0)}$, $I_{(t=\infty)}$, $R_{(t=0)}$, $R_{(t=\infty)}$ and calculated t_+ , for the investigated samples consisting of PEG-150 with dissolved LiClO_4 and dispersed SiO_2 , 7nm-fumed. 10 mV of potential was applied across the symmetric cell (values with t_+ , 100 mV of potential). All the measurements were carried out at room temperature.

Sample	7 nm-fumed				
	$I_{(t=0)}/\mu\text{A}$	$I_{(t=\infty)}/\mu\text{A}$	$R_{(t=0)}/\Omega$	$R_{(t=\infty)}/\Omega$	t_+
0.01M $\text{LiClO}_4/\text{PEG} - 150$, $\varphi = 0$	3.14	0.89	748.1	742.7	0.23
0.01M $\text{LiClO}_4/\text{PEG} - 150 : \text{SiO}_2$, $\varphi = 0.01$	1.48	1.10	139.0	478.3	0.77
0.1M $\text{LiClO}_4/\text{PEG} - 150$, $\varphi = 0$	5.21	2.02	810.9	1109	0.29
0.1M $\text{LiClO}_4/\text{PEG} - 150 : \text{SiO}_2$, $\varphi = 0.01$	9.87	5.98	655.4	890.0	0.46
0.5M $\text{LiClO}_4/\text{PEG} - 150$, $\varphi = 0$	11.03	4.63	60.54	69.83	0.41
0.5M $\text{LiClO}_4/\text{PEG} - 150 : \text{SiO}_2$, $\varphi = 0.01$	35.78	20.89	157.3	262.1	0.56
1M $\text{LiClO}_4/\text{PEG} - 150$, $\varphi = 0$	27.69	9.77	58.84	92.67	0.33
1M $\text{LiClO}_4/\text{PEG} - 150 : \text{SiO}_2$, $\varphi = 0.01$	37.33	20.25	49.26	61.22	0.51*

Table 2.10: Values for measured $I_{(t=0)}$, $I_{(t=\infty)}$, $R_{(t=0)}$ and calculated t_+ , for the investigated samples consisting of PEG-150 with dissolved LiClO_4 and dispersed SiO_2 , 10nm. 10 mV of potential was applied across the symmetric cell (values with t_+ , 100 mV of potential). All the measurements were carried out at room temperature.

Sample	10nm				
	$I_{(t=0)}/\mu\text{A}$	$I_{(t=\infty)}/\mu\text{A}$	$R_{(t=0)}/\Omega$	$R_{(t=\infty)}/\Omega$	t_+
0.01M $\text{LiClO}_4/\text{PEG} - 150$, $\varphi = 0$	3.14	0.89	748.1	742.7	0.23
0.01M $\text{LiClO}_4/\text{PEG} - 150 : \text{SiO}_2$, $\varphi = 0.01$	0.0332	0.0209	342.0	523.9	0.63
0.1M $\text{LiClO}_4/\text{PEG} - 150$, $\varphi = 0$	5.21	2.02	810.9	1109	0.29
0.1M $\text{LiClO}_4/\text{PEG} - 150 : \text{SiO}_2$, $\varphi = 0.01$	5.43	3.88	691.2	626.0	0.59
0.5M $\text{LiClO}_4/\text{PEG} - 150$, $\varphi = 0$	11.03	4.63	60.54	69.83	0.41
0.5M $\text{LiClO}_4/\text{PEG} - 150 : \text{SiO}_2$, $\varphi = 0.01$	12.26	8.67	160.9	298.5	0.77
1M $\text{LiClO}_4/\text{PEG} - 150$, $\varphi = 0$	27.69	9.77	58.84	92.67	0.33
1M $\text{LiClO}_4/\text{PEG} - 150 : \text{SiO}_2$, $\varphi = 0.01$	172.57	86.50	30.64	63.09	0.50*

2. EXPERIMENTAL SECTION

2.3.4 Zeta-Potential

2.3.4.1 Theory

Zeta potential measurements allow the determination of the electrical potential change close to the interface and provide information on the adsorbed charges. The zeta-potential plays a central role in the repulsive forces between particles due to the electrical double layers (75).

The liquid electrolyte layer surrounding a solid particle consists of: **(1)** an inner rigid region sometimes called the *Stern layer*, where ions are more or less strongly bound and **(2)** an outer diffuse region, where they are less firmly attached (Fig. 2.25). The so-called zeta-potential is the potential at the transition from Stern plane to diffuse layer relative to the bulk ($\zeta = \Psi^d - \Psi_{x=\infty}$). If there is a relative motion between the particle

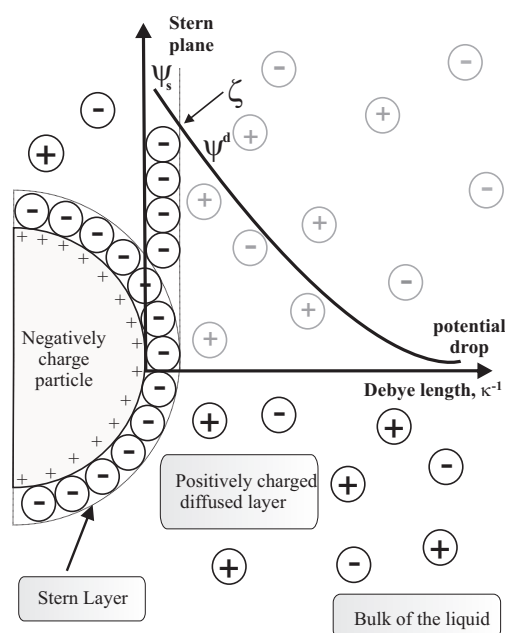


Figure 2.25: Model of ionic double layer created on particle oxide surface due to ion adsorption.

and the solution, there must be gliding plane within the space charge zone. The potential at this gliding plane is the electrokinetic potential. In most cases the electrokinetic potential is identified within the zeta-potential. It is not just this approximation but also the fact that the space charge layer may dynamically reconstruct as well as the

complexity of the experimental configuration that confers a semi-quantitative character on the measurement of the zeta-potential.

2.3.4.2 Results

To understand the local mechanism in the solution present between filler particles and to verify the adsorbed charge on the oxides surface as well as in vicinity of oxides dispersed in electrolyte, zeta-potential measurements using the electroacoustic technique were applied. In Figure 2.26 one can see changes in zeta-potential as a function of silica (7nm-fumed and 10nm) weight percent in ‘pure’ solvent (DMSO) containing no dissolved ions. The values of zeta-potential are slightly negative.

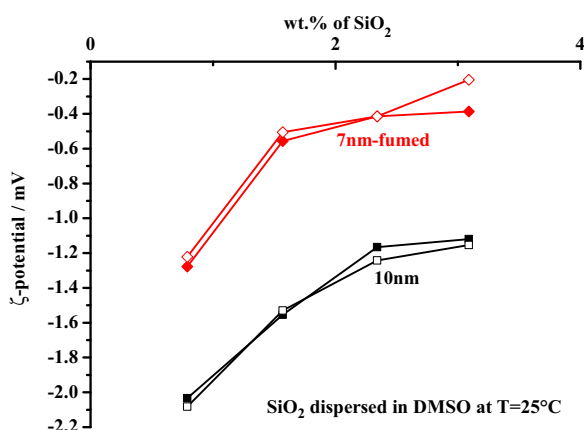


Figure 2.26: Zeta-potential as a function of weight fraction of SiO₂, 7nm-fumed and 10nm for ‘pure’ DMSO. Measurement was carried out at room temperature (open symbols – measurements without stirring; close symbols: measurements with stirring).

In Figure 2.27 and Figure 2.28 one can observe the change in zeta-potential as a function of weight fraction of SiO₂ (7nm-fumed and 10nm), and due to different concentrations of LiCl or LiClO₄. Values of zeta-potential were less negative, in the case of LiClO₄ or less positive, in the case of LiCl, with higher concentration of oxides and with reduced concentration of lithium salt. One can also observe slight differences between the different size SiO₂ particles (7nm-fumed and 10nm).

For the systems of electrolytes containing PEG-150 as a solvent one can find the oxide particles exhibiting zeta-potential behaviours similar to that of DMSO. In Fig-

2. EXPERIMENTAL SECTION

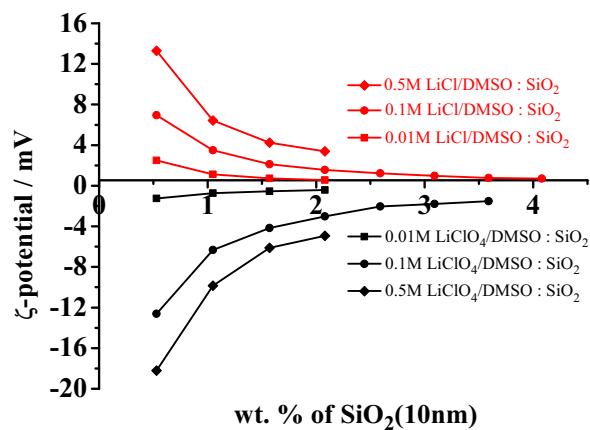


Figure 2.27: Zeta-potential as a function of weight fraction of SiO₂, 10nm for LiCl/DMSO:SiO₂ and LiClO₄/DMSO : SiO₂ systems. Salts concentration is at the range from 0.01M to 0.5M. Measurement was carried out at room temperature.

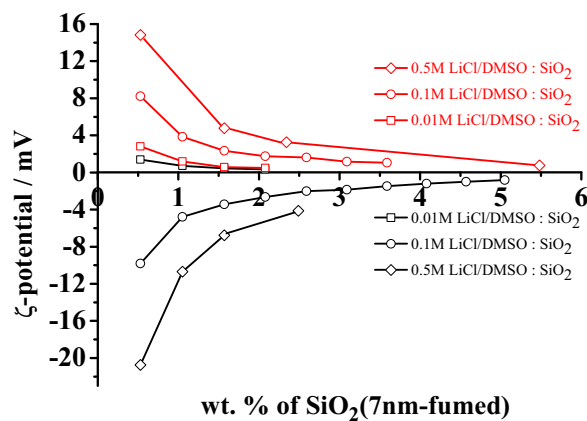


Figure 2.28: Zeta-potential as a function of weight fraction of SiO₂, 7nm-fumed for LiCl/DMSO:SiO₂ and LiClO₄/DMSO : SiO₂ systems. Salts concentration is at the range from 0.01M to 0.5M. Measurement was carried out at room temperature.

2.3 Experimental Results

ure 2.29 only LiClO_4 is considered as LiCl could not be dissolved in PEG-150 at those concentrations. One can find that the values of zeta-potential are less negative with

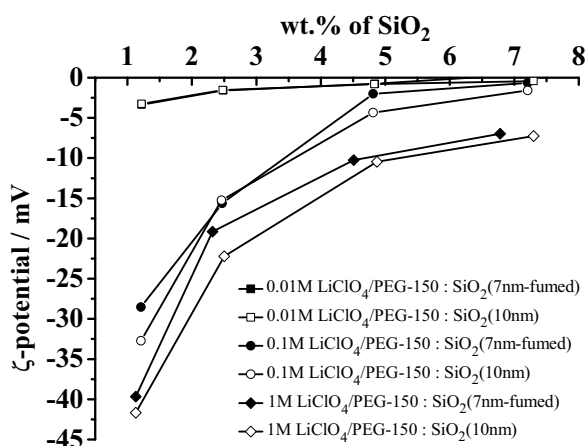


Figure 2.29: Zeta-potential as a function of weight fraction of SiO_2 , 7nm-fumed and 10nm for $\text{LiClO}_4/\text{PEG} - 150 : \text{SiO}_2$, salt concentrations range from 0.01M to 1M. Measurement was carried out at room temperature.

higher concentration of oxides as well as with reduced molarity of lithium salt. The same tendency but significantly more negative zeta-potential values were observed in the case of highly viscous PEG-350 (see Table 2.11).

Table 2.11: Zeta-potential for different weight fraction of SiO_2 , 7nm-fumed and 10nm for 0.01M $\text{LiClO}_4/\text{PEG}-350 : \text{SiO}_2$. Measurement was carried out at room temperature.

0.01M $\text{LiClO}_4/\text{PEG} - 350 : \text{SiO}_2$			
7nm-fumed		10nm	
wt.%	ζ -potential	wt.%	ζ -potential
1.2%	-543.7 mV	1.2%	-567.9 mV
2.3%	-274.0 mV	2.4%	-267.0 mV
3.6%	-195.4 mV	4.6%	-149.0 mV
5.3%	-126.0 mV	6.9%	-102.0 mV

2. EXPERIMENTAL SECTION

Since the magnitude of the zeta-potential gives an indication of the potential stability of the colloidal systems, here the obtained results suggest that the system becomes less stable with higher particles concentration. However, higher molarity of lithium salt at low weight fraction of SiO_2 ensures higher stability of the system. If the particles in suspension have large negative zeta-potential values (< -30 mV), they will tend to repel each other. Hence, there will be a smaller tendency to flocculate. On the other hand, if the particles have lower zeta-potential values then there is only a weaker force to prevent the particles coming together and flocculation will rapidly take place. The decrease of ζ with increasing φ , decreasing $[\text{LiX}]$ and increasing r points towards a lowered mean charge density at the oxide's surface. All this will be taken up in the discussion. Most important is the fact that the zeta-potential is negative in all cases (except for LiCl in DMSO) that is in line with the space charge model (see Discussion). The exceptional behaviour of LiCl is well-known in literature and perhaps is based on the high polarizability of Cl^- and the high strength of solvation.

2.3.5 Viscosity

2.3.5.1 Fluids behaviours

The viscosity (η) of a fluid is a measure of the internal resistance which is deformed by either shear stress, or extensional stress. In everyday terms (and just for fluids), viscosity is understood ‘thickness’. Thus, one can think of a ‘thin’ fluid as a fluid having a lower viscosity, while the ‘thick’ fluid has a higher viscosity. Ideal cases of condensed matter are:

1. **Hookean solid**, that is, an ideal solid which obeys Hooke’s law, where the stress (τ) is directly proportional to strain (γ): $\tau = G \cdot \gamma$ (G is the elastic modulus).
2. **Newtonian liquid** for which $\tau = \eta \cdot \dot{\gamma}$ ($\dot{\gamma}$ is shear strain rate).

Viscous fluids can be divided in two classes (see Fig. 2.30): (1) Newtonian Fluids – where the viscosity is constant with shear rate; the plot shear stress (τ) as a function of shear strain rate ($\dot{\gamma}$) is linear and passes through the origin (Fig. 2.31), and (2) Non-Newtonian Fluids – where the flow properties are not described by a constant viscosity; the relation between shear stress (τ) and shear strain rate ($\dot{\gamma}$) is hence non-linear, and can be time dependent (Fig. 2.30(a) and (b)).

The time dependencies can be distinguished as *rheopexy* (*anti-thixotropy*), where the apparent viscosity increases with duration of stress; and *thixotropy*, where the apparent viscosity decreases with duration of stress (see Fig. 2.30(a) and (b)). As to shear stress one can single out *shear thickening*, where the apparent viscosity increases

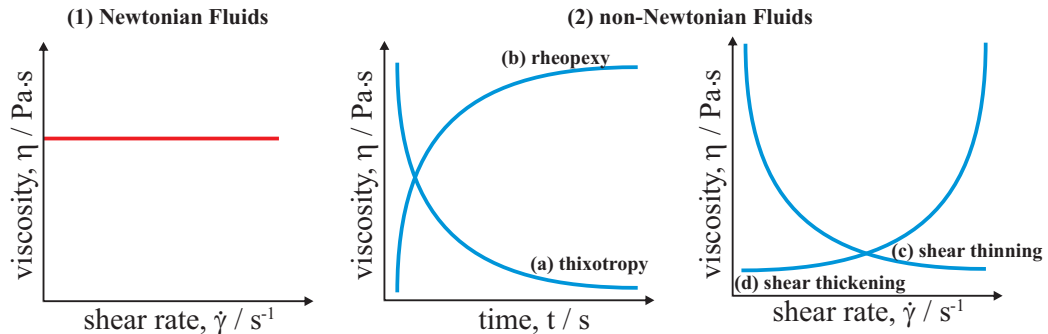


Figure 2.30: Viscous fluids behaviours, (1) Newtonian Fluids, (2) non-Newtonian Fluids, (a), (b) viscosity as a function of time, (c), (d) viscosity as a function of shear rate.

2. EXPERIMENTAL SECTION

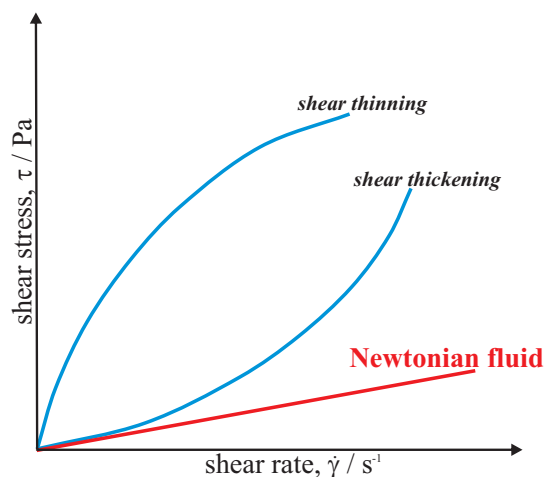


Figure 2.31: Viscous fluid behaviour – shear rate ($\dot{\gamma}$) as a function of shear stress (τ).

with increased stress and *shear thinning*, where the apparent viscosity decreases with increased stress (see Fig. 2.30 and Fig. 2.31).

2.3.5.2 Results

To verify the fluid behaviour in the network of oxide particles in the composite electrolytes, viscosity measurements were applied.

Firstly, viscosity as a function of time was measured under constant shear rate, $\dot{\gamma} = 500 \text{ s}^{-1}$. The Figures 2.32, 2.33(a) and 2.33(b) display this time dependence for different solvents, oxide particles, and volume fractions.

One observes that the viscosity is more or less unchanged with time for low volume fraction of silica. The figures show that situation changes in highly concentrated systems. One can find decreasing viscosities which are characteristic (higher volume fraction) of non-Newtonian, thixotropic fluids. This decrease is quite steep during the first 20 second of the measurement. The viscosity recovers after having removed the shear rate. This suggests that reversible severe morphological changes depend on time in systems containing higher amount of oxides. This time dependence should not be confused with the time dependence discussed in Subsection 2.3.2.2 occurring immediately after preparation. In Figures 2.34(a), 2.34(c) and 2.34(e) one can see that the effective viscosity (η) for all dilute (low volume fraction, φ) systems decreases with increased value of shear strain rate ($\dot{\gamma}$).

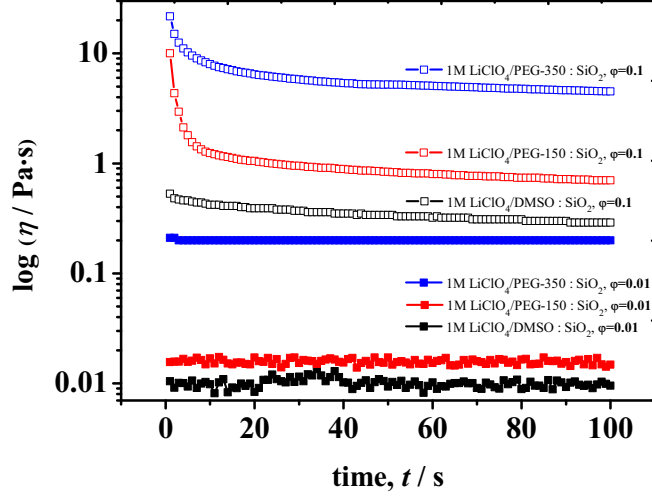


Figure 2.32: Viscosity as a function of time for 1M LiClO₄ composite electrolytes containing of DMSO, PEG-150, PEG-350 with low and high concentration of SiO₂ 10nm. Measurements were carried out at room temperature.

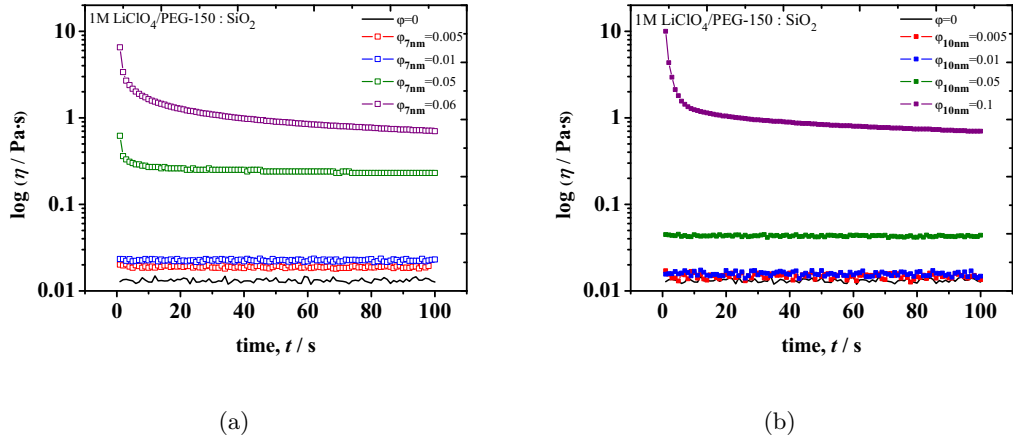


Figure 2.33: Viscosity as a function of time for 1M LiClO₄ composite electrolytes containing of PEG-150 and different concentration of SiO₂ (a) 7nm-fumed and (b) 10nm. Measurements were carried out at room temperature.

2. EXPERIMENTAL SECTION

This kind of behaviour is typical for shear thinning non-Newtonian fluids. Figure 2.34(e) also compares viscosity of two different size silica particles – 7nm-fumed and 10nm. One can notice that the viscosity is slightly higher for systems containing particles of smaller size (7nm-fumed). One can notice from Figures 2.34(a), 2.34(c), 2.34(e) that at higher volume fraction the viscosity decreases and starts growing again. As the time dependence (see above) is a monotonic decrease, a superposition of transient properties cannot lead to such a minimum. Rather we observe a transition from shear thinning to shear thickening. In the very concentrated systems containing highly viscous solvent such as PEG-350, there is even shear thickening right from the beginning. Obviously due to the large packing local density up can lead to even more viscous entities.

Figures 2.34(b), 2.34(d) and 2.34(f) present shear stress (τ) as a function of shear strain rate ($\dot{\gamma}$) (compare with Fig. 2.31). In cases of dilute systems, one observes shear thinning. The curves corresponding to $\varphi = 0 - 0.01$ do not cross the origin even though their behaviour is quite close to Newtonian fluids. At higher concentration ($\varphi = 0.01$) the situation is more complex and one observes both thickening and thinning as a function of shear strain rate (first thinning regime is not visible due to small number of data points). In Figure 2.35(a) and Figure 2.35(b) one can observe that for dilute as well as for concentrated (with respect to φ) systems, reversibility of the systems has not been attained. This effect is more pronounced for dilute samples and suggest alterations of the network morphology. Because in dilute systems the disconnected particles as well as smaller clusters are placed farther away from each other in comparison to denser system, this is expected.

2.3 Experimental Results

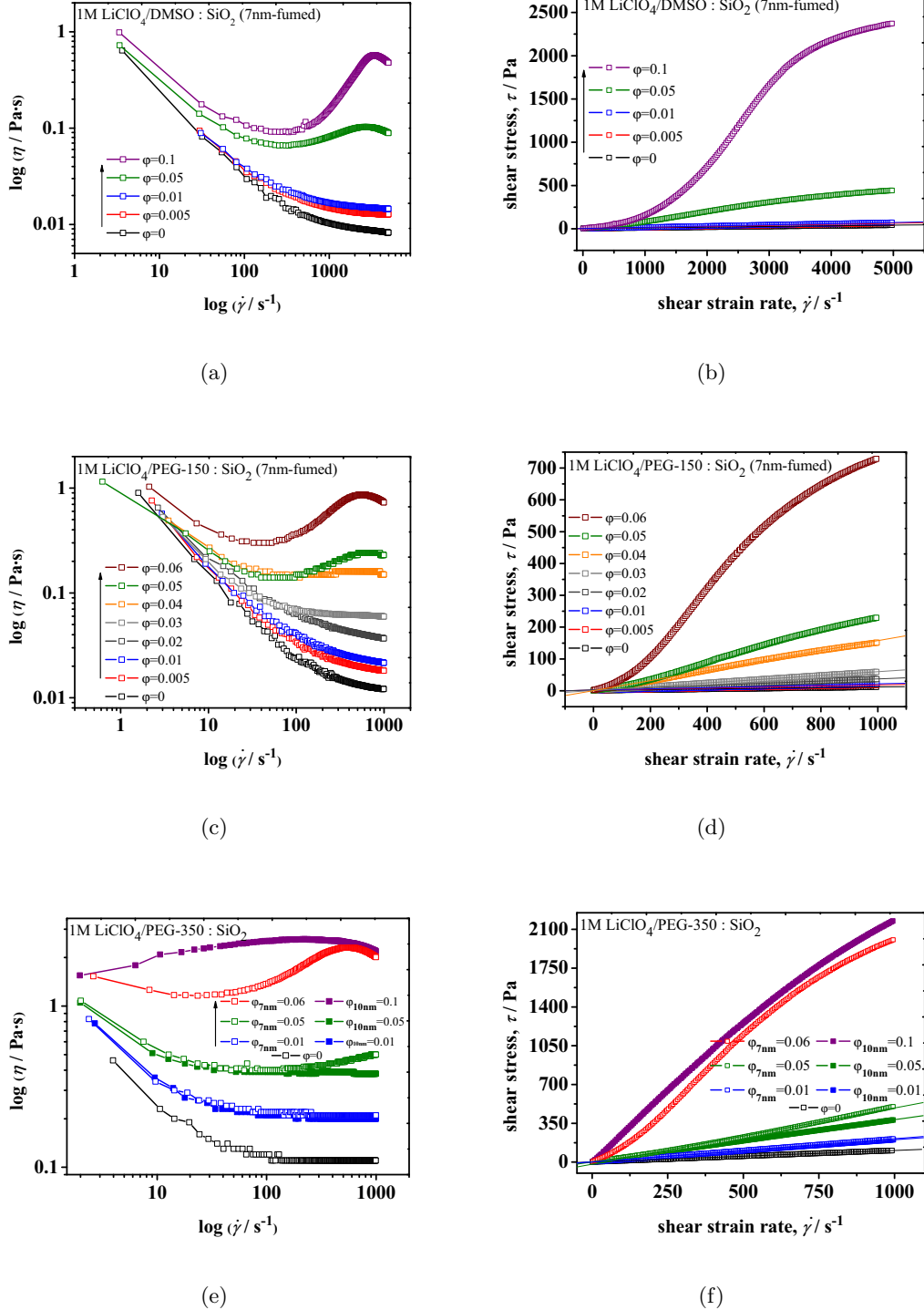
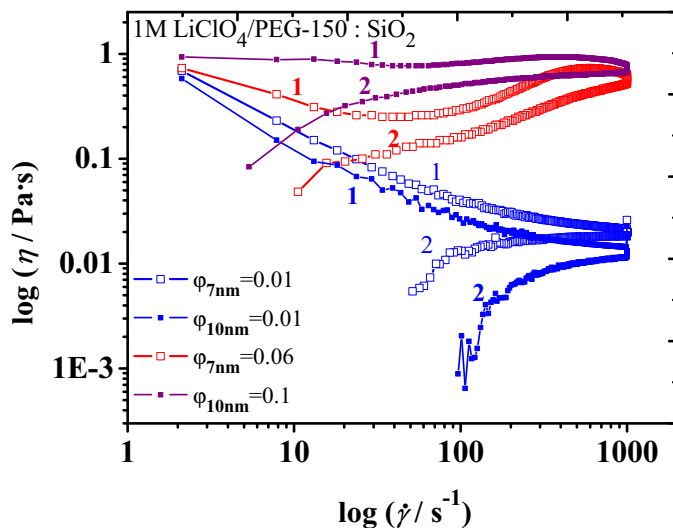
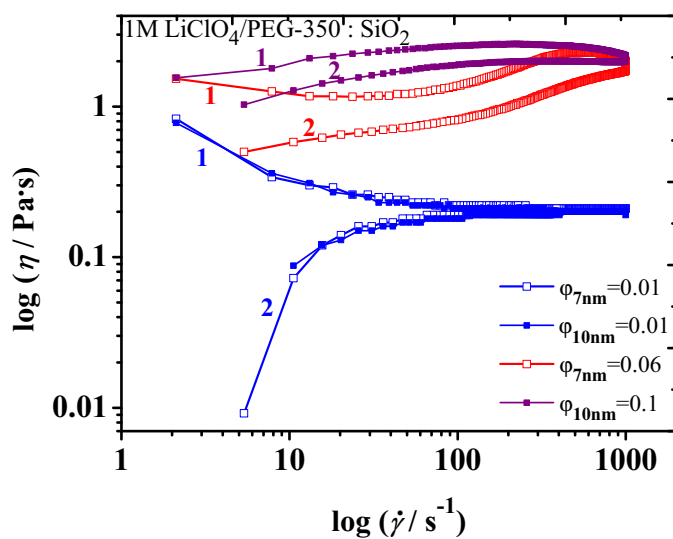


Figure 2.34: (a), (c), (e) Viscosity (η) as a function of shear strain rate ($\dot{\gamma}$) for composite electrolyte systems ((a), (b) 1M LiClO₄/DMSO : SiO₂, 7nm-fumed; (c), (d) 1M LiClO₄/PEG – 150 : SiO₂, 7nm-fumed; (e), (f) 1M LiClO₄/PEG – 350 : SiO₂, 7nm-fumed; 10nm) and (b), (d), (f) shear stress (τ) as a function of shear strain rate ($\dot{\gamma}$) for the same systems. Measurements were carried out at room temperature. (open symbols: 7nm-fumed, closed symbols: 10nm).

2. EXPERIMENTAL SECTION



(a) 1M LiClO₄/PEG – 150 : SiO₂, 7nm-fumed; 10nm



(b) 1M LiClO₄/PEG – 350 : SiO₂, 7nm-fumed; 10nm

Figure 2.35: Effective viscosity, η as a function of increased and decreased shear rate, $\dot{\gamma}$ for different polymer composite electrolytes. Measurement was carried out at room temperature. 1 – shear strain rate increase (first run); 2 – shear strain rate decrease (second run).

3

Numerical Modelling and Simulation

3.1 Modelling Methods

3.1.1 ‘Monte Carlo Random Walk Method’

In this thesis the ‘Monte Carlo’ technique was used to model the formation of the percolating oxide clusters due to the ‘random walk’ of oxide particles.

The ‘Monte Carlo Method’ term was used (76) to model stochastic processes by the physicists N. Metropolis, S. Ulam and von Neumann. Their calculations were carried out to predict the flux of neutrons in an atomic bomb. The flow of neutrons following random paths through a mass of uranium molecules, could only be modelled on a computer and not predicted from theory (77). Despite having most of the necessary data, the problem could not be solved with theoretical calculations. However, modelling on a computer using chance was proposed as a solution (78). Being a top-secret issue, Von Neumann and Ulam’s work required a code name. Von Neumann chose the name ‘Monte Carlo’, as a reference to the Monte Carlo Casino in Monaco – the gambling centre of the world (77, 79, 80).

‘Monte Carlo’ simulation methods are useful for modelling phenomena with significant uncertainty in inputs and/or systems with a large number of coupled degrees of freedom. Those techniques are often the only practical way to sample random variables governed by complicated probability density functions.

3. NUMERICAL MODELLING AND SIMULATION

A key idea in colloidal science that launched the study of particle aggregation and gellation is that of *fractals* (81, 82). Witten and Sander (83) made a breakthrough by proposing the *Diffusion-Limited Aggregation (DLA)* model. In this model a particle is released from the rim of a simulation box and allowed to diffuse (*via* random walk). When the diffusing particle hit another one, aggregation occurs. One of the famous Witten and Sander fractals, using ‘Monte Carlo’ technique is shown in Figure 3.1. This

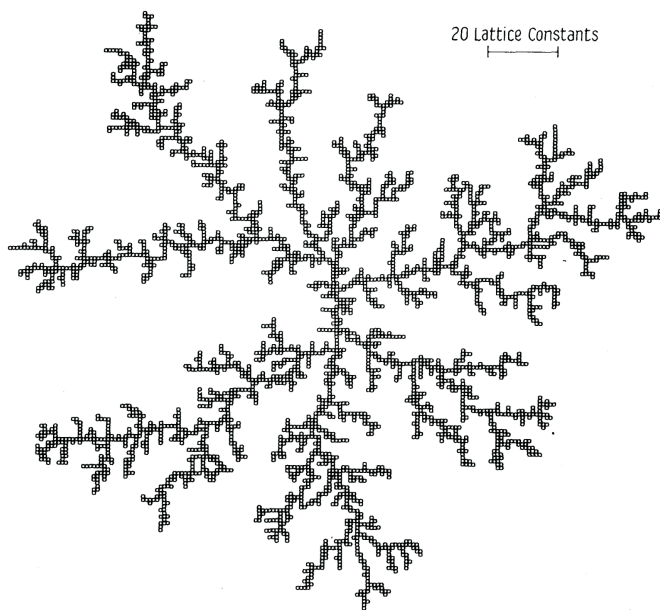


Figure 3.1: A fractal cluster growth according to Witten and Sander (83)

cluster has a fractal dimension of 1.7. In the DLA model the final fate of particles is either to stick to an initial ‘seed’ particle or to disappear off the rim again. Since the process is iterated, a ramified (non-compact) cluster is built up. Weitz and co-workers (84) showed that this model could be used to interpret the structure of real particle aggregates.

In this simple DLA model, two mobile, colloidal particles always bind upon meeting. This kind of binding is irreversible. In more general approaches, the binding probability is less than unity with a finite probability for subsequent unbinding (85). Although this is often called *Reaction-Limited Aggregation (RLA)*, this term is only appropriate if the

binding/unbinding process is sluggish compared with diffusion. In the *Cluster-Cluster Aggregation (CCA)* model one also allows clusters to diffuse and bind. If diffusion is the rate determining process, the term *Diffusion-Limited Cluster Aggregation (DLCA)* is used. The DLCA had been typically performed with low-concentrated systems, with the focus on the structural description of individual clusters in terms of fractal dimension (d_f) and statistical distributions of various structural parameters such as the radii of gyration of clusters (r_g) as functions of time. The DLCA model assists in understanding the formation of mesoscopic structures of aggregating colloids due to the presence of short range attraction between the aggregating particles. This computational model was independently initiated by Meakin (86) and Kolb and co-workers' (87) in the context of fractal growth. Figure 3.2 shows the process. Such growing clusters

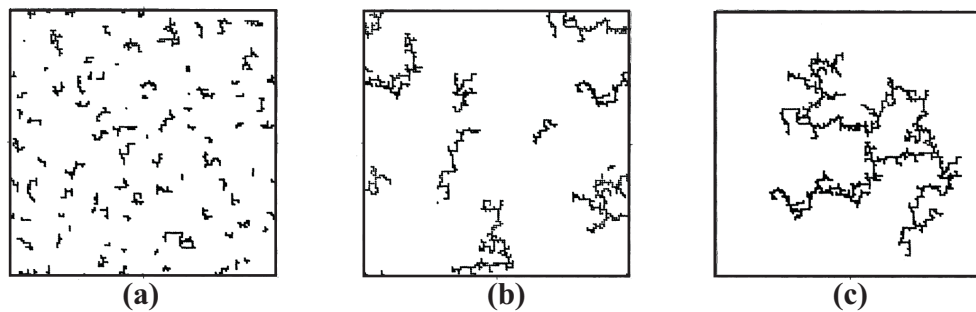


Figure 3.2: Kolb and co-workers simulation of the growth of clusters (87)

were found to be fractals, i. e. the mass of a cluster (m) which is proportional to the number of particles in a cluster (n), scales with its radius of gyration (r_g) as

$$n \sim m \sim r_g^{d_f} \quad (3.1)$$

where the non-integer d_f is the fractal dimension. In two dimensions the fractal dimension of such cluster from the large-scale computer simulations is $d_f = 1.42 \pm 0.05$ (82, 88). Also the kinetics of DLCA were found to depend on cluster mass (m) as

$$D_{cl}(m) \sim m^{-1/d_f} \quad (3.2)$$

where D_{cl} is the diffusion coefficient of a cluster. Since a gel composed of particles is a ramified space-filling structure, the gellation process can be described on the basis of growth of fractal structures (82).

3. NUMERICAL MODELLING AND SIMULATION

The modelling part of this thesis is subdivided in two parts according to two time regimes. The first describes the DLCA mechanism of forming fractal clusters. It is based on an irreversible ‘hit-and-stick’ mechanism. This formation of clusters and their growth create percolation paths, which in reality corresponds to ionic conductivity increase due to formation of the ionic path on oxide particles surface.

The second part of the modelling is related to coarsening effect. During this process more packed clusters are formed because of particles’ tendency to minimize the surface energy of the cluster. As this process is characterized by surface diffusion which can be assumed to be more sluggish than particle diffusion in the liquid characterizing the ‘hit-and-stick’ process, this two-step modelling is a reasonable first order approach.

3.1.2 Metropolis-Hastings algorithm

In the present thesis the Metropolis-Hastings algorithm was used to model the coarsening of the fractal structures, corresponding to the second time regime. The Metropolis-Hastings algorithm generates a sequence of random samples from a probability distribution for which direct sampling is difficult (89). This sequence can be used to approximate the unwieldy distribution or to compute expected values of integrals.

The algorithm was named after N. Metropolis. Together with his co-workers they proposed in 1953 an algorithm for analysing the specific case of the Boltzmann distribution (90). Later in 1970 W. K. Hastings (91), extended those algorithm to more general cases.

The Metropolis-Hastings algorithm is called today ‘simulated annealing’. Each particle on the square is moved according to a random (uniform) perturbation, forming a new configuration. This new configuration is accepted if the effected change in energy $\Delta E < 0$; or if $\Delta E > 0$, the configuration is accepted with the probability $\exp(-\Delta E/k_B T)$. Otherwise the previous one is retained. The system adopts a Boltzmann distribution for each state t which is proportional to $\exp(-E_t/k_B T)$. The perturbations of the particles are uniform and probabilities considering the move from state t to state t' are equal to the reverse move ($P_{t' t} = P_{t t'}$) according to the principle of microscopic reversibility. Hastings included the possibility of a non-symmetric instrumental distribution (89).

In the generalization by W. K. Hastings, the Metropolis-Hastings algorithm generates a ‘Markov Chain’ in which each state x^{t+1} depends only on previous one x^t .

The algorithm uses a proposal density (instrumental density from which the candidate x' was drawn, $Q(x'; x^t)$), which depends on the current state x^t , to generate a new proposed sample x' and to calculate a value

$$\alpha = \frac{P(x')}{P(x^t)} \cdot \frac{Q(x^t; x')}{Q(x'; x^t)} \quad (3.3)$$

where $P(x')/P(x^t)$ is the probability ratio between the proposed sample x' and the previous sample x^t , and $Q(x^t; x')/Q(x'; x^t)$ is the ratio of the proposal density in two directions (from x^t to x' and opposite). This is equal to 1 if the proposal density is symmetric. Then the new state x^{t+1} is chosen according to:

$$\begin{aligned} &\text{if } \alpha \geq 1 : x^{t+1} = x', \\ &\text{if } \alpha < 1 : x^{t+1} = \begin{cases} x' & \text{with probability } \alpha \\ x^t & \text{with probability } 1 - \alpha \end{cases} \end{aligned} \quad (3.4)$$

The algorithm works best if the proposal density matches the shape of the target distribution $P(x)$, that is $Q(x'; x^t) \approx P(x')$, but in most cases this is unknown.

3.2 ‘Hit-and-Stick’ Mechanism

As the consequence of ‘hit-and-stick’ mechanism driven by Brownian motion, clusters grow into fractal structures that comprise more and more particles, eventually linking together into a continuous gel (continuous solid phase). The reason why colloidal particles initially kept at some distance owing to electrostatic repulsion eventually stick together has been explained in Section 1.4 and highlighted by Figure 1.6.

In the first step a square lattice with given finite size is generated. Occupied sites are randomly placed in the system, with a certain probability, p (empty sites with probability $1 - p$). The probability values vary with the desired concentration. Then the single particles are allowed to move in randomly generated direction if a randomly chosen site is empty. If the site is occupied or the perimeter of the percolation system is reached, then the movement of the ‘random walker’ towards this site is rejected. However, the model considers the cluster growth due to hit and stick with such an occupied site (31). This ‘hit-and-stick’ process is repeated until the desired number of time steps have been performed, until all occupied sites are connected and all particles belong to one cluster (cluster number is 1). In the next step the program is checking

3. NUMERICAL MODELLING AND SIMULATION

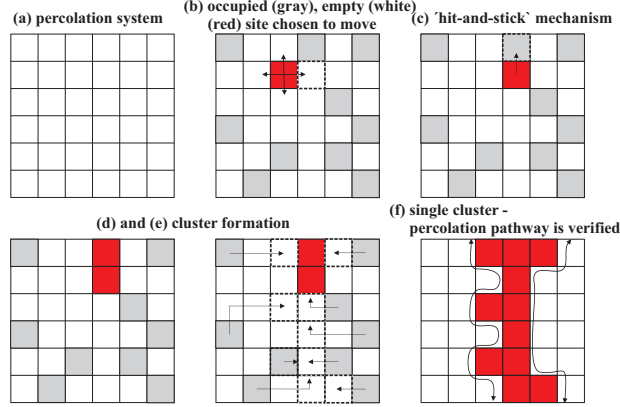


Figure 3.3: Schematic explanation of ‘Hit-and-stick’ mechanism (white squares – empty sites, gray squares – occupy sites, red square – randomly chosen site, expected to move). Occupied sites moved until all of them are connected. This ‘loop’ is repeated at least 1000 times.

if the final cluster percolates: 1 if yes (at least one particle is found on each: left-right or bottom-up lattice edge) or 0 if not, i. e.

$$N = \begin{cases} 0 \\ 1 \end{cases} \quad (3.5)$$

This procedure is repeated many times (m , minimum 1000 times) for each p and in the last step the program is counting the average percolation threshold occurrence for every p :

$$P(p) = \frac{N_1 + N_2 + N_m}{m} = \bar{N} \quad (3.6)$$

A schematic explanation of the above explained ‘hit-and-stick’ mechanism is presented in Figure 3.3.

To stress it again: at small p values, the system contains more empty sites, and creation of an ion conducting path connecting opposite edges of the lattice is less probable. However, at larger p values, many ion conducting paths between opposite edges exist. Therefore, at some concentration p_c a threshold concentration must exist, at which for the first time ions can percolate from one edge to the other. In systems in which there is no matrix conductivity, a jump of the conductivity occurs.

In our case matrix conductivity and conductivity along percolating pathways are not so different as to lead to such drastic effects. Table 3.1 shows such threshold concentrations, p_c for different percolation system sizes, for the probability values (p) which separate a phase of finite clusters $p < p_c$ from a phase where an infinite cluster is present $p > p_c$ (31). The average value of cluster radius r for each lattice sizes was calculated from

$$r = \frac{1}{n} \sum_{L=1}^n \sqrt{(x_L - x_0)^2 + (y_L - y_0)^2} \quad (3.7)$$

where n is the number of occupied places, x , y are coordinates of each occupied place, the index 0 refers to the first occupied place on the lattice and L is for all others. Comparing threshold concentrations, p_c at $P(p) = 0.5$ for different lattice sizes one can

Table 3.1: Calculated estimates for the average threshold concentration, p_c obtained for different size percolation systems for average value of percolation threshold occurrence, $P(p) = 0.5$ (n is particles number and r is an average cluster radius calculated from Equation 3.7).

Lattice[weight, height]	p_c	n	r
[50, 50]	0.3780	934	24.545
[100, 100]	0.3640	3616	50.008
[200, 200]	0.3490	13930	102.415
[350, 350]	0.3360	41106	181.1442
[500, 500]	0.305	76247	257.977
[600, 600]	0.302	108638	310.463
[700, 700]	0.299	146655	363.655

notice that percolation pathways occurred significantly earlier in the case of greater lattice size (corresponding to smaller particle size). For all these lattices and threshold concentration, p_c the fractal dimension was calculated from the slope obtained from the function of particles number (cluster mass) versus its average radius.

In Figure 3.4 one can find the fractal dimension obtained for various lattice sizes to be equal to $d_f = 1.872$. Additionally the fractal dimension was calculated for two percolation systems at various concentrations (lattice[100,100] in Figure 3.5(a) and lattice[500,500] in Figure 3.5(b)). The fractal dimension for clusters on the smaller lattice is equal 1.6 and for clusters on the larger lattice is 1.657.

3. NUMERICAL MODELLING AND SIMULATION

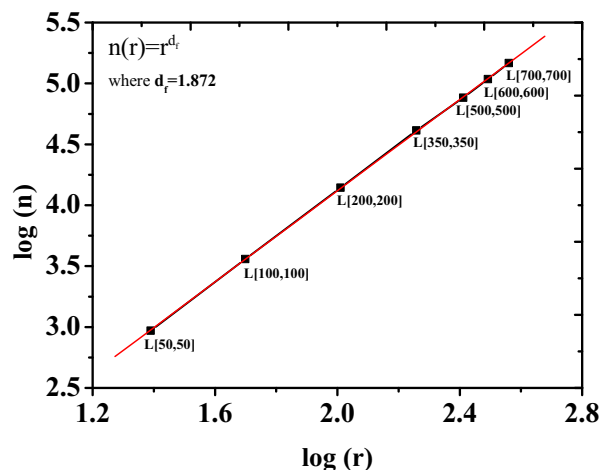
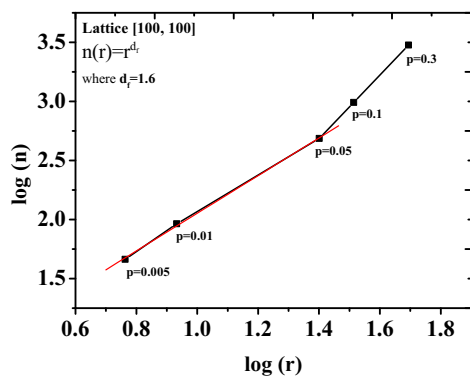
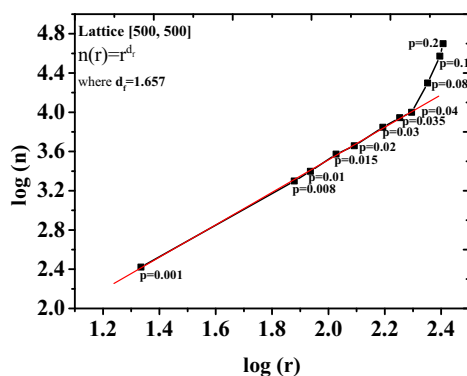


Figure 3.4: Particles numbers of the percolating cluster as a function of average radius of the percolating cluster for different system sizes. Fractal dimension (d_f) obtained from the slope, $d_f = 1.872$.



(a) Lattice[100, 100]



(b) Lattice[500, 500]

Figure 3.5: Particles numbers of the clusters as a function of their average radius for two systems at various concentrations, (a) Lattice[100, 100], (b) Lattice[500, 500]. Fractal dimension (d_f) obtained from the slope, (a) $d_f = 1.6$, (b) $d_f = 1.657$; (slopes increase qualitatively because of boundary effect).

To explore different situations which can occur during cluster formation in real systems, lattice size (see Fig. 3.6), concentration of occupied sites (see Fig. 3.7) and sticking probabilities (see Fig. 3.8) were varied. In Figure 3.6 one can see that for percolation systems of larger size but for the same value of concentration of occupied sites ($p = 0.05$), the fractal structure is more branched also. The space filling depends on the size of the percolation system. The small cluster is substantially more confined than the region within which its unaggregated particles were originally contained. A larger region gives a larger aggregate. The aggregate radius grows quicker than the radius of the region originally containing the particles to obtain the same size as the initial region (82).

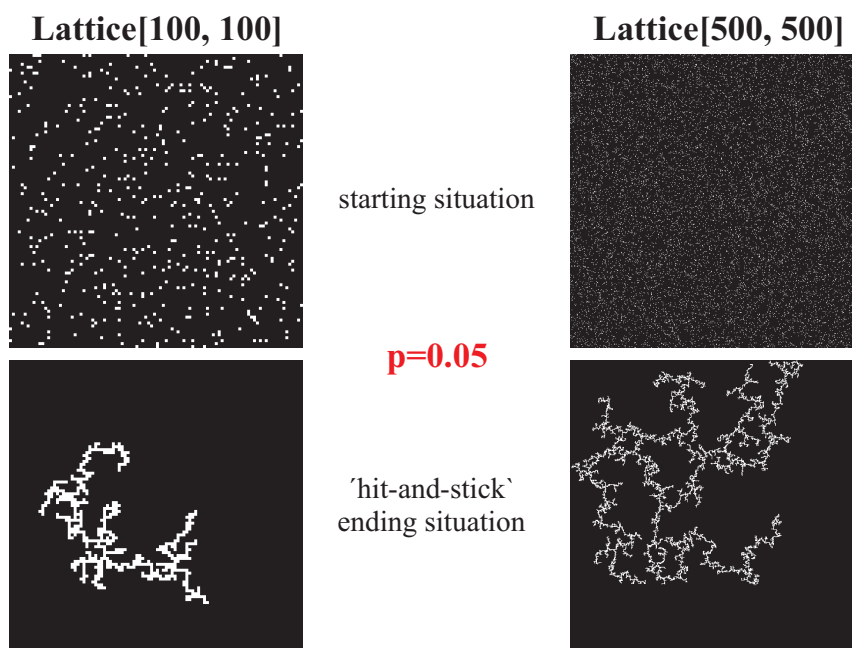


Figure 3.6: Different lattice sizes ([100, 100] and [500, 500]) of fractal structures (clusters), starting and ending conditions for ‘hit-and-stick’ mechanism.

Figure 3.7 presents the evolution of the fractal structure with increased concentration of occupied sites for percolation systems of small size (Lattice[100, 100]; qualitative impression). One can notice that with higher concentration of sites in use, the probability of percolation will increase, what in real system means, increased ionic conductivity. It is important to remember that with a larger size of the percolation system the percolation thresholds occurred earlier (Tab. 3.1).

3. NUMERICAL MODELLING AND SIMULATION

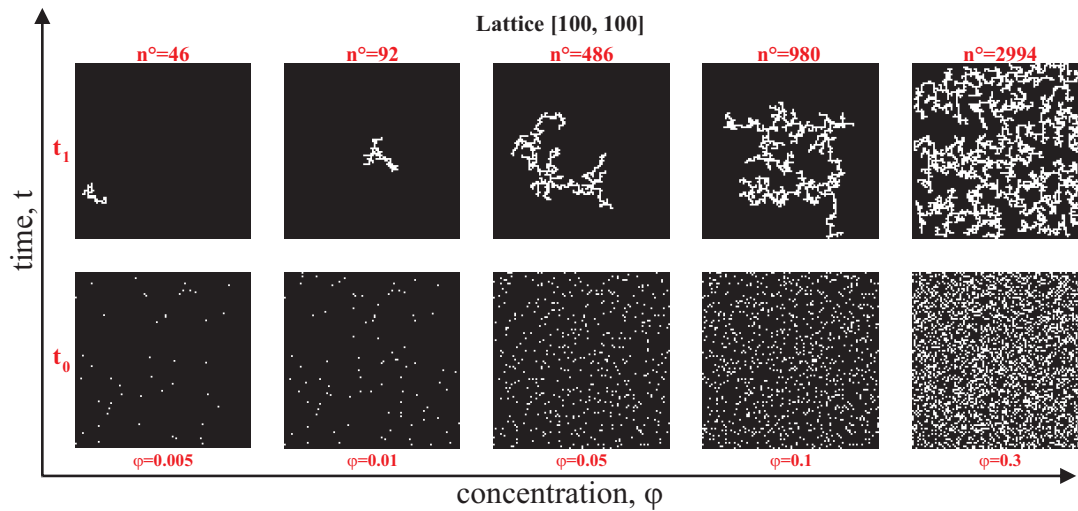


Figure 3.7: Different fractal structures (clusters) of various concentration of occupied sites (e. g. $\varphi = 0.005$, $\varphi = 0.01$, $\varphi = 0.05$, $\varphi = 0.1$, $\varphi = 0.3$), starting and ending conditions for ‘hit-and-stick’ mechanism (n° is a number of particles).

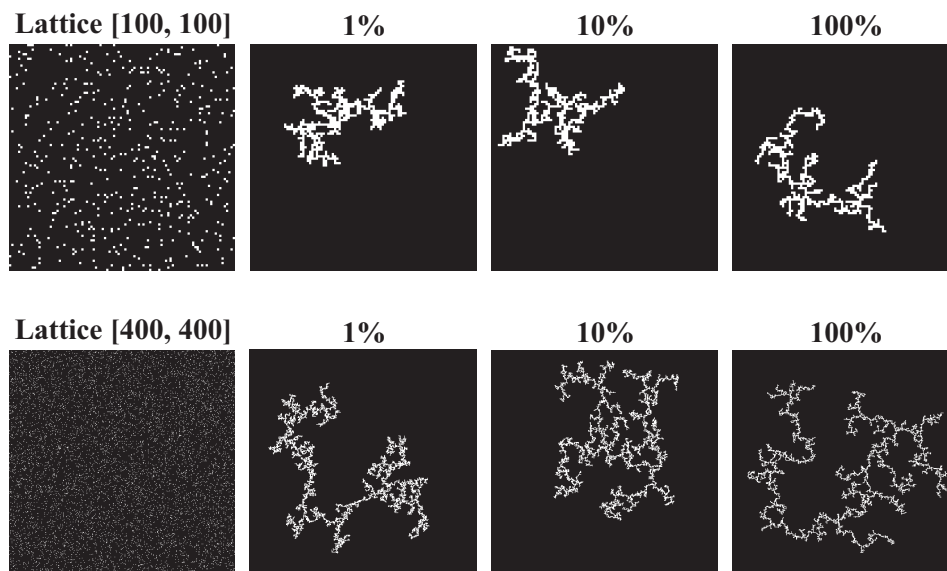


Figure 3.8: Different fractal structures because of various sticking probabilities (1%, 10% and 100%), starting and ending conditions.

Figure 3.8 shows how the situation changed with lowered sticking probability. It can be seen that after reducing the probability to 10% or even to 1% , a denser aggregate is formed. At first sight, it is surprising that the reduction in the sticking probability results in a denser agglomerate, but as literature confirms (Ref. (77)) this seems reasonable if one consider the fact that after touching the edge of the growing cluster the more mobile (less sticky) unit has a greater chance of penetrating into the space dominated by the filaments of the agglomerate, so that they can join the growing cluster further down inside its bush-like structure. As a consequence of obtaining denser aggregates the threshold concentration, p_c (e. g. for lattice [100, 100] p_c increases from 0.364 at 100% through 0.434 at 10% until 0.445 at 1%) also increases.

3.3 Coarsening

It was observed from experimental results that the ionic conductivity initially decreased with time. This can be explained by coarsening of the ‘hit-and-stick’-cluster on a longer time scale (typically 1 hour). Coarsening can happen by network rearrangement caused by the particles to glide (surface diffusion). The driving force is the minimalisation of the surface energy. In this way a particle can even be released from the cluster (with the low probability). It is also obvious that a particle with many contacts is quite immobilized and coarsening is very sluggish (see Fig. 3.9). In this way coarsening leads to more compact clusters. This modelling part starts after having obtained one cluster

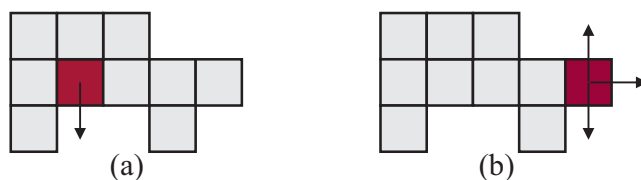


Figure 3.9: Various situation for particles due to different number of contacts.

as a result of the ‘hit-and-stick’ mechanism. Then a single particle of this cluster is randomly chosen, which is expected to glide. Then the gliding probability to a certain direction is investigated. For this purpose we estimate the energy of the ground state by counting the energy of a shared edge by Δ and, further arbitrarily, the energy of a shared corner by $1/2\Delta$ (i. e. interaction energy to a full contact is counted as Δ and to a partial contact as $1/2\Delta$). Similarly the transition state energy is estimated. There we assume that half a contact (half edge) also counts by $1/2\Delta$. This is depicted by Figure 3.10 and Figure 3.11.

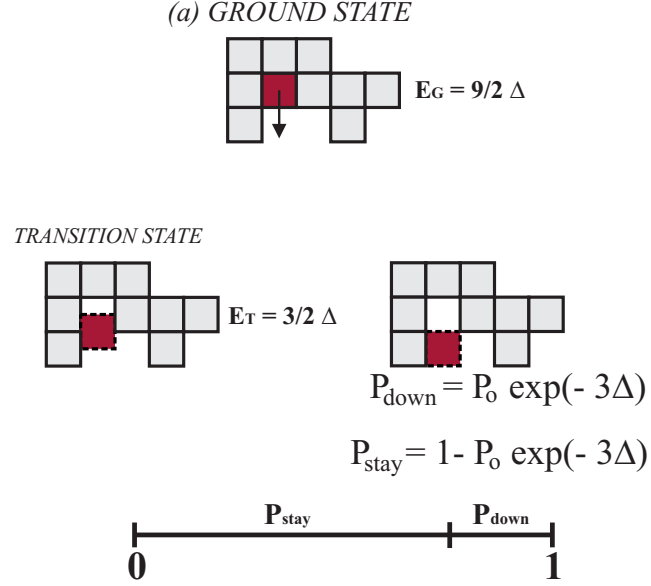


Figure 3.10: Schematic representation of coarsening of quite immobilize particle (one possible move) which at ground state has 3 full contacts (3Δ) and 3 partial contacts ($3/2\Delta$), used to calculate ground state energy. At transition state particle has 3 partial contacts ($3/2\Delta$). The difference between these two energies gives the activation energy (3Δ), (E_G , E_T are ground state and transition state energy, respectively).

The gliding probability in a given direction i is then calculated according to

$$P_i = \frac{1}{\chi} P_o \exp(-E_i) \quad (3.8)$$

where χ is a number of possible movements, P_o is a temporal frequency of ‘vibrating’ particles and E is difference between ground state energy (E_G) and transition state energy (E_T) for each movement. In other words: P_o/χ is the attempt frequency in the given direction. The probability of a particle to stay is

$$P_{\text{stay}} = P_o \left(1 - \frac{1}{\chi} \sum \exp(-E_i) \right) \quad (3.9)$$

3. NUMERICAL MODELLING AND SIMULATION

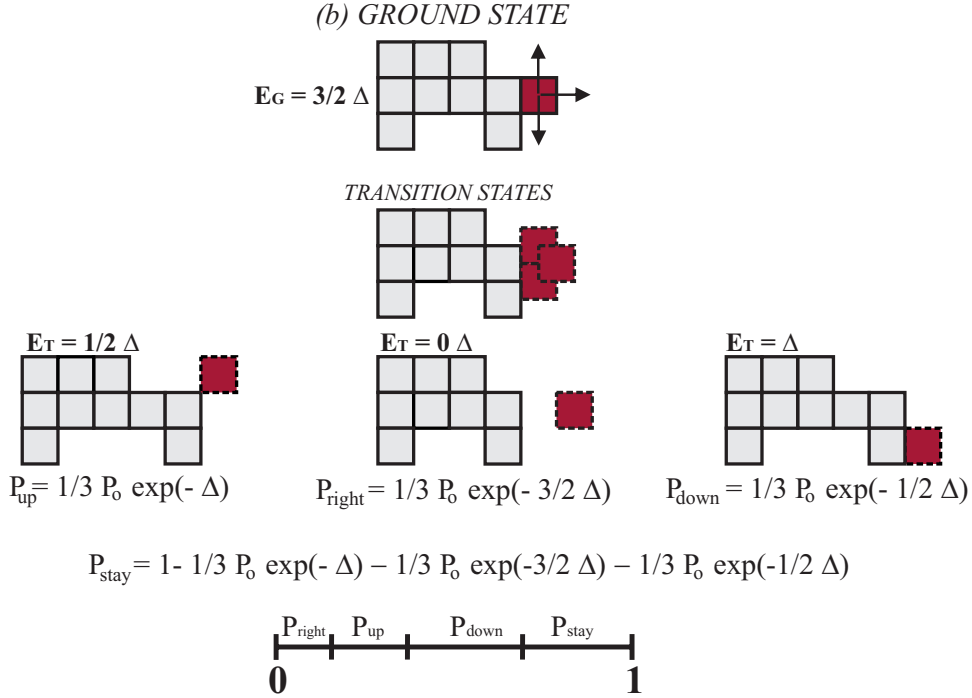


Figure 3.11: Schematic representation of coarsening of quite mobile particle (three possible moves) which at ground state has 1 full contact (Δ) and 1 partial contact ($1/2\Delta$), used to calculate ground state energy. The particle has three possible transition states. To move up (1 partial contact $1/2\Delta$); to move right (no contacts 0Δ); to move down (2 partial contacts Δ), used to calculate transition state energy (E_G , E_T are ground state and transition state energy, respectively). The difference between these two energies gives the activation energies.

Resorting to normalized probabilities \bar{P} rather than to absolute probabilities, by replacing P_o by αP_o , we have

$$\sum \bar{P}_i + \bar{P}_{stay} = \alpha \cdot P_o \left(\frac{1}{\chi} \sum \exp(-E_i) + 1 - \frac{1}{\chi} \sum \exp(-E_i) \right) = \alpha \cdot P_o = 1 \quad (3.10)$$

Hence $\bar{P}_i = P_i/P_o$.

Figure 3.12 shows how the cluster structures change due to coarsening. One recognizes that again many, but this time more compact clusters are obtained. An important consequence for the conductivity is that percolation pathways are destroyed and the conductivity rapidly decays.

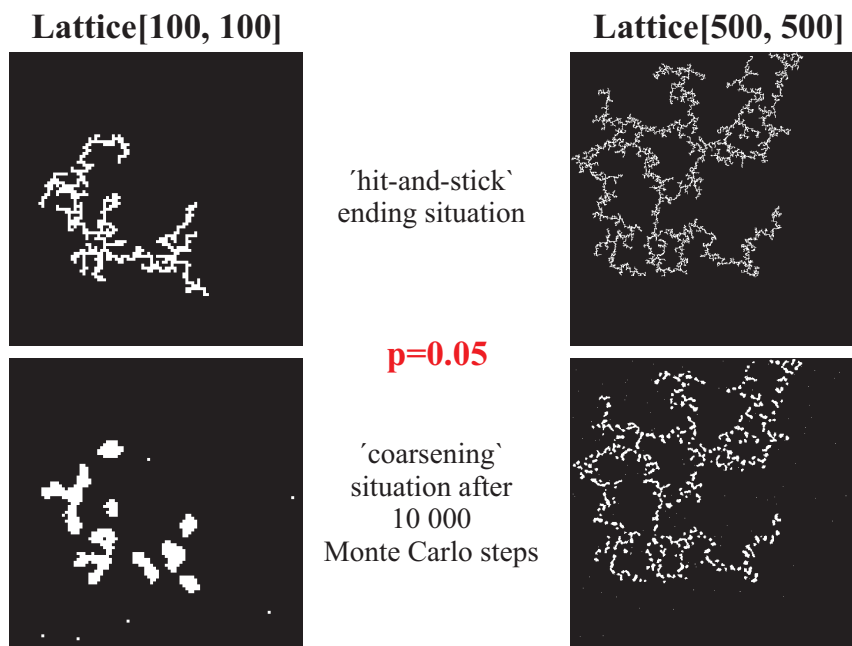


Figure 3.12: Changes in fractal structures due to coarsening for different lattice sizes ([100, 100] and [500, 500]), starting and ending (after 10 000 Monte Carlo steps) situations for coarsening.

In Figure 3.13 one can see similar changes in clusters structures as a function of various concentration of occupied sites due to coarsening. For more concentrated systems particles lose connection and form many, more compact clusters. The situation looks different for less concentrated systems, where, apart from few single particles which lose connection, one compact cluster is created. Figure 3.14 shows also differences in fractal structures (clusters) after coarsening due to changes in sticking probability. One can notice that for lower sticking probability values (1% and 10%) the clusters are formed with higher connectivity between them. Due to coarsening, the previously obtained fractal structure changed into a more compact one, that consequently leads to sedimentation and trapping of the solvent (Fig. 3.15). Figure 3.16 shows similar results for a more packed situation, where the particles exhibit on average more contacts.

3. NUMERICAL MODELLING AND SIMULATION

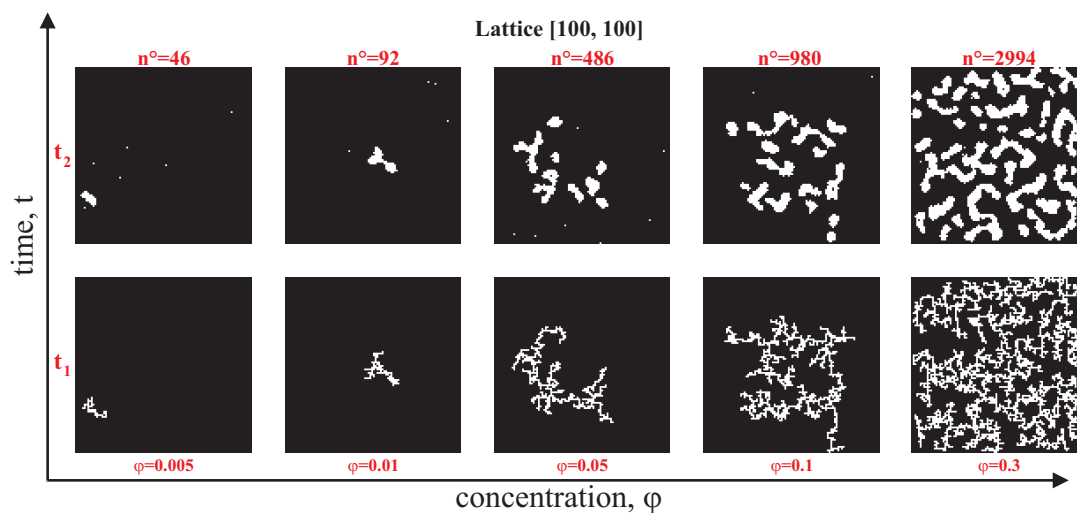


Figure 3.13: Different fractal structures for various concentration (e.g. $\varphi = 0.005$, $\varphi = 0.01$, $\varphi = 0.05$, $\varphi = 0.1$, $\varphi = 0.3$) of occupied sites due to coarsening; ending situations for ‘hit-and-stick’ mechanism and for coarsening after 10 000 Monte Carlo steps; n° is a number of particles.

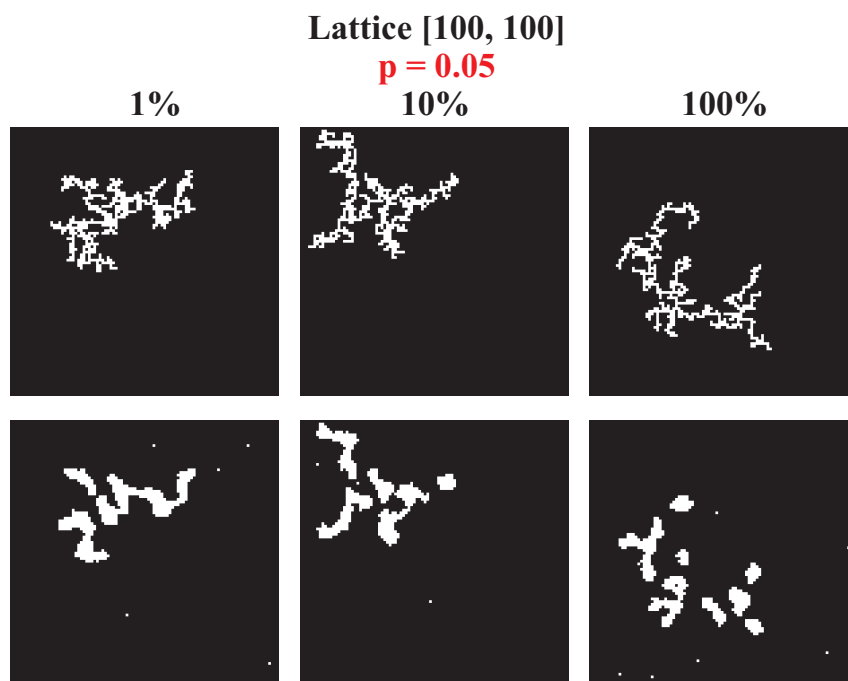


Figure 3.14: Changes in fractal structures after coarsening due to changes in sticking probability, starting and ending conditions for coarsening.

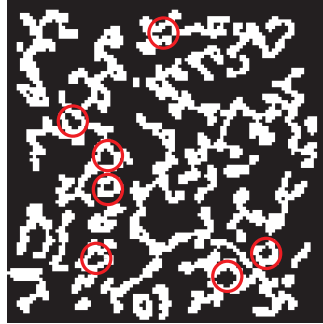


Figure 3.15: Examples of 'trapping' due to coarsening (Lattice[100,100], concentration $p=0.3$, 10000 Monte Carlo Steps).

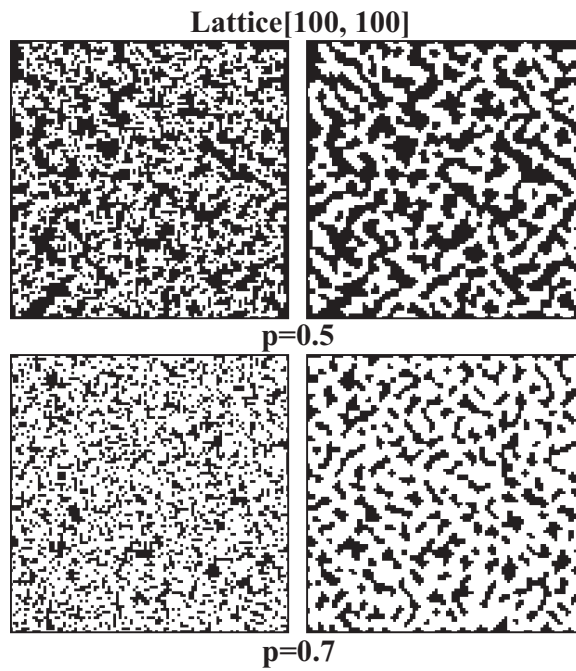


Figure 3.16: Changes in very concentrated fractal structures after coarsening.

3. NUMERICAL MODELLING AND SIMULATION

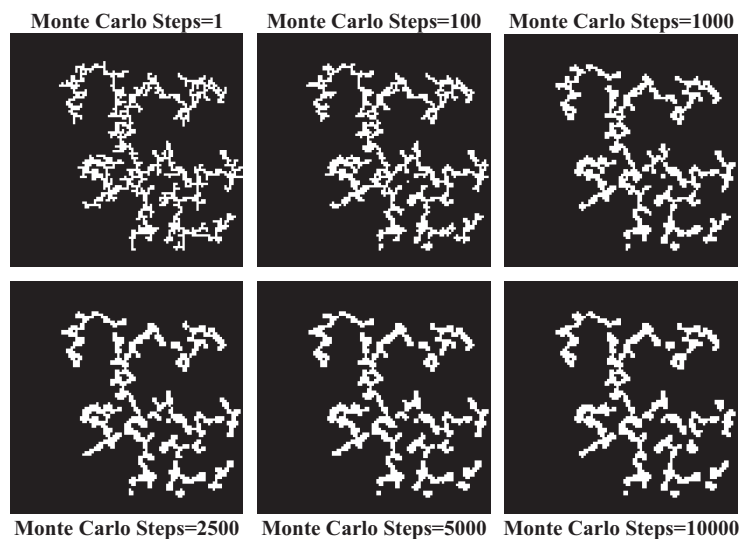


Figure 3.17: Coarsening process decelerates with time. Significant coarsening of ‘lose particles’ occurs on a shorter time scale (until ~ 1000 Monte Carlo Steps).

This is very obvious also from Figure 3.10 and Figure 3.11. The increase of the activation threshold for gliding by a factor of 2 leads to quadratic gliding probability; as $\bar{P} < 1$, $\bar{P}^2 \ll 1$. This point also emphasizes the fact that the coarsening process decelerates with time. The cluster evolution in Figure 3.17 shows clearly that within lower time steps the decisive rearrangement take place, while later (steps 2500 to 10000) only minor effects are observed.

The loss of percolation is augmented by the tendency of the larger particles to sediment. If a dispersion of particles is denser than the surrounding medium, it should be expected that the particles will experience a relative force to move downwards due to the action of gravity. When sedimentation does take place, the volume of the final sediment depends upon the extent of aggregation as well as on the inter-particle interactions. Aggregating particles form a continuous network structure which extends throughout the available volume and immobilizes the dispersion medium. The conductivity decrease due to sedimentation is further augmented by trapping of the solvent (see Paragraph 2.3.2.1).

4

Discussion

Here we briefly summarize qualitatively the main results that are to be explained by local mechanistic considerations and the network modelling.

We concentrate on the system LiClO_4 -PEG (PEG-150, PEG-350) and SiO_2 as the dispersoid (7nm-fumed, 10nm). Figure 4.1 indicates a typical plot “conductivity versus SiO_2 volume fraction” for the starting situation and the steady state. The steady state curve is typically reached at about 1 hour. The time constant τ is fairly constant under all conditions at room temperature but decreases with increasing temperature (around 1 hours for 10°C and around 25 minutes at ($\sim 35^\circ\text{C}$)). The σ -variation with time ($\delta\sigma$) is larger for smaller volume fraction and larger grain size, i. e. larger for lower packing density. $\delta\sigma$ also increases with decreasing viscosity (PEG-350 \rightarrow PEG-150).

As to the steady state values the conductivity increase on adding second phase particles $\Delta\sigma$ ($\Delta\sigma \equiv \sigma(\varphi) - \sigma(0)$) slightly increases when 7nm-fumed SiO_2 is used instead of 10nm; in fact $\Delta\sigma$ is roughly proportional to $1/r$. Owing to the lower viscosity the conductivities for PEG-150 are larger than for PEG-350, but the situation is inverse for $\Delta\sigma/\sigma(0)$, also in the case of zeta-potential the values are significantly more negative for PEG-350. For high φ -values the conductivity sharply drops to values slightly below $\sigma(\varphi = 0)$. The T -dependence is complicated due to network irreversibilities and will not be discussed further on.

Owing to the experimental difficulties not for all experimental points Li^+ transference numbers could be measured. But it was seen that on SiO_2 addition the Li^+ transference increased if the overall conductivity was increased. This gives independent information that the increase primarily affects the Li^+ conductivity. As to the

4. DISCUSSION

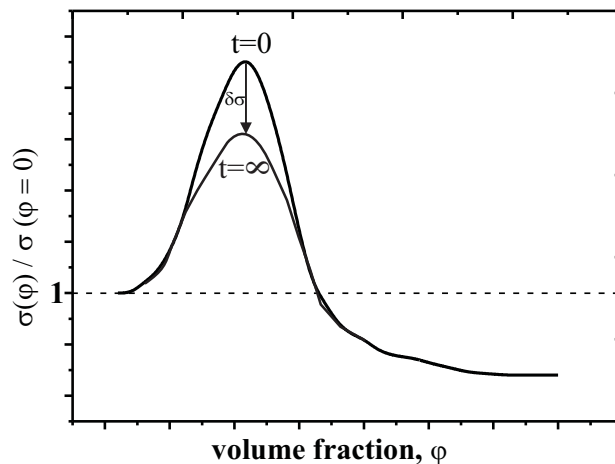


Figure 4.1: Typical plot representation conductivity versus SiO_2 volume fraction for starting and steady state situations.

SiO_2 pure solvent the transference number ranges from 20-50% and is higher for higher LiClO_4 concentration. This is due to the fact that dilution favour solvation and the strong Li^+ solvation lowers the mobility. For 10nm particles the increase in the transference number is more substantial for 0.5M LiClO_4 than for dilute ones. For 7nm-fumed the variation with such condition is different. Whether this is indicative of a different interaction behaviour is doubtful.

The zeta-potential is negative (much more negative than for the SiO_2 free situation); the magnitude decreases with higher volume fraction and higher salt concentration. The rheological behaviour is very different for low and high SiO_2 volume fractions. At low volume fractions we observe shear rate thinning with an almost time-independent viscosity under constant shear rate, while at high concentration a transition to shear rate thickening is observed. At constant shear rate ($\dot{\gamma} = 500 \text{ s}^{-1}$) the viscosity decreases with time. As in the case of temperature dependence irreversible effects are significant.

4.1 Interpretation

The interpretation of these results succeeds in terms of the **(a)** local interfacial mechanism occurring at the SiO₂/solvent interfaces and **(b)** the network behaviours. A reasonable explanation of the local conductivity effects can be given by the model of Heterogeneous Doping and was provided in Reference (24, 26, 33) when discussing “soggy sand” electrolytes. In this mechanism the acidic SiO₂ adsorbs anions of the Li-salt leading to breaking up of the ion pairs in the vicinity. Given large enough an effect all ion pairs will be broken in the space charge zones and the Li⁺ transference number therein, will be unity.

As shown in the above references the overall conductivity can be given by

$$\sigma_m = (1 - \varphi)\sigma_\infty + \beta\varphi\bar{\sigma} \quad (4.1)$$

where the mean space charge conductivity $\bar{\sigma}$ can be approximated by $\mu\sqrt{2\varepsilon\varepsilon_0RTc_0}$; for spherical particles the surface-to-volume ratio (Ω) is $3/r$. The initial increase of σ_m with φ , the initial proportionality of the second term with $1/r$ as well as the sign of the zeta-potential are all in line with the experiments. The decrease of $|\zeta|$ with φ and LiClO₄ can be readily explained by the fact that the charge density will decrease with increased overall SiO₂ surface available and decreased concentration of ions.

The results are also fairly in agreement with the transference number measurements. As we assume $\bar{\sigma} = \bar{\sigma}_+$ (where the index +, - refers to Li⁺, X⁻) and $\sigma(0) = \sigma(0)_+ + \sigma(0)_-$ the overall Li⁺ conductivity is

$$\sigma_{m+}(\varphi) = (1 - \varphi)\sigma(0) + \beta\varphi\Omega\bar{\sigma}_+ \quad (4.2)$$

where the argument zero $\varphi = 0$ refers to the SiO₂ free electrolyte. With the transference number definitions

$$t_{m+} \equiv \frac{\sigma_{m+}}{\sigma_m} \quad (4.3)$$

and

$$t(0)_+ \equiv \frac{\sigma(0)_+}{\sigma(0)} \quad (4.4)$$

We can write the observed relative conductivity enhancement $\Delta\sigma/\sigma_m$ in terms of the transference numbers as

$$\frac{\Delta\sigma}{\sigma_m} = \frac{(t_{m+} - (1 - \varphi)t(0)_+ - \varphi)}{(1 - t_{m+})} \quad (4.5)$$

4. DISCUSSION

which reduces for small φ to $\frac{t_{m+}-t(0)_+}{1-t_{m+}}$.

Let me make a brief estimate: A typical enhancement in the range of 1-5% for 1M LiClO₄/PEG-150:SiO₂ is by a factor of 1.2-1.3. We then expect – according to Equation 4.5 – a solution with a transference number $t(0)_+$ of 50% to increase on slight SiO₂-doping to a measured transference number of 60%. This is (see Table 2.8) obviously in agreement with the results. The fact that both conductivity and transference number enhancements are quite small is due to the fact that the space charge zones are not exceedingly more conductive than the bulk which contributes a lot to the overall values. An increase of the LiClO₄ concentration leads to an increased ion pair concentration and hence to larger enhancement of the Li⁺ conductivity. Yet non-idealities have to be considered at these high concentrations.

Of course we need percolating pathways in order to observe a long range conductivity as assumed above. The fact that the conductivity is quite low and even lower than the initial value can be ascribed to the fact that at large values of φ lowly charged SiO₂ particles (see Fig. 2.27; Fig. 2.28 and Fig. 2.29) block the network. As the modelling shows, coarsening in conjunction with sedimentation can trap salt making it inefficient even for bulk transport.

The relaxation phase of the freshly prepared two phase mixture before the steady state morphology is reached, is very revealing in this context. The modelling clearly shows how sensitive the coarsening kinetics depend on the packing density (compare the two situations in Figure 4.2 **(1)** $\bar{P}_1 \propto \exp -\Delta$; **(2)** $\bar{P}_2 \propto \exp -2\Delta = \bar{P}^2$).

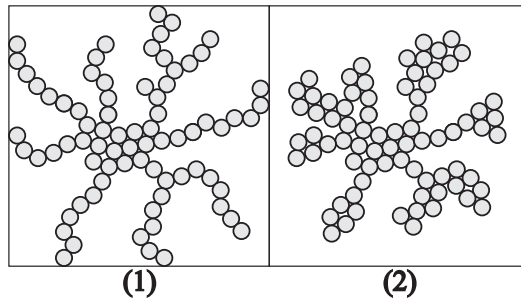


Figure 4.2: Coarsening kinetics depend on the packing density.

Hence as Figure 4.2 indicates we only expect the morphologies characterized by a low number of the nearest neighbours to vary in the experimental time window (τ_0); the

time constance for coarsening of partial morphologies involving highly packed arrangements can be assumed to be too large. This is corroborated by the fact that all the experimental time constants are similar (~ 10 - 20 min) irrespective of packing density etc., and it is only the conductivity drop $\delta\sigma$ that varies significantly.

If the network is very fragile (all the configurations have a low number of contacts) then a larger $\delta\sigma$ is observed than for network with only a small fraction of a low coordination number. This readily explains the observed variation of $\delta\sigma$ with φ and r .

The formation of coherent networks that break up under shear stress has been shown by the mechanical measurements. At low concentration and given non-zero shear stress, breaking up and reforming the network is fast and comparably equal, whereas for high φ this is unsurprisingly slower; at first breaking up of the network dominates and later equilibrium occurs between breaking up and reforming the network (thixotropy). The transition to shear rate thickening at high φ can be explained by increased resistance of the aggregates towards deformation. At high volume fractions, the particles are very close together and the average separation of the particles is very small. Therefore, the particle-particle interaction forces are large and will strongly affect the relative position of the particles. At low shear rates the stabilized particles have a sufficient opportunity to slip over each other; the interparticle forces tend to keep them in a layered-structure (at laminar flow). At a certain shear rate, the shearing process may become so rapid that the particles begin to pile up and to create a considerable resistance (92, 93) (turbulent flow). Due to this one can expect that the mechanical treatment causes a change from an ordered (layered) ‘fluid-’ like particle distribution to an irregular ‘solid-’like loose packing of particles what causes shear-thickening behaviour (see Fig. 4.3) (94).

4. DISCUSSION

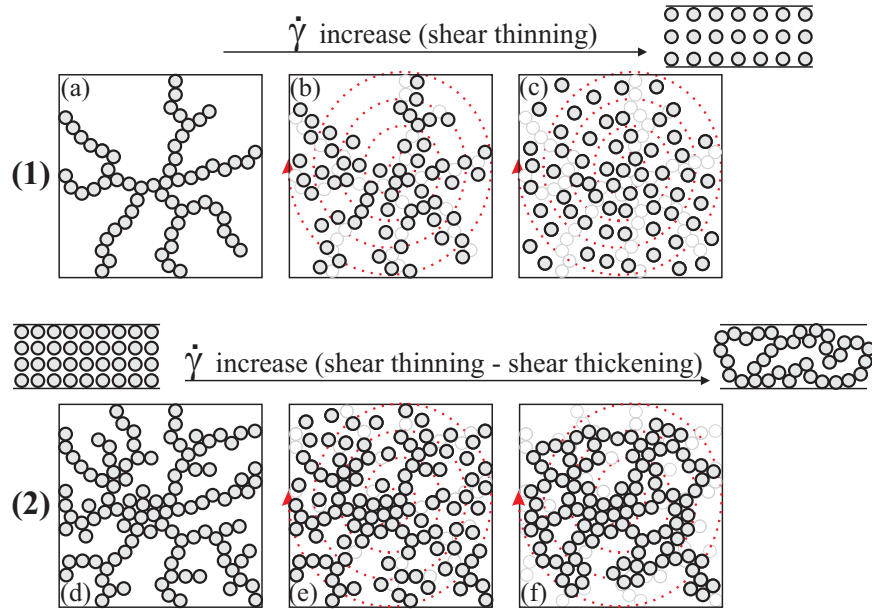


Figure 4.3: Schematic representation of various behaviours in diluted and concentrated systems.

4.2 Outlook and search for appropriate “Soggy Sand” electrolytes

This thesis mainly focused on composite liquid-solid electrolytes. As presented in this work, even in quite dilute systems significant ionic conductivity enhancement as well as improvements of the mechanical properties were found. In the literature enhancement effects have also been observed at higher volume fraction (more than 10% by volume of fillers), for example in “soggy sand” electrolytes containing low dielectric constant, non-aqueous solvents such as tetrahydrofuran (THF) (24, 33, 95), in composite polymer electrolytes (36), and in weak covalent electrolytes containing imidazole, where proton conductivity was enhanced (96). In this higher range of volume fractions the situation reminds of the Nafion-type composite electrolytes in which the counter ions are attached to the polymer backbone and the protons can move within tiny water filled channels (97, 98).

At quite high volume fractions, the introduced oxide particles are expected to be heavily connected (packing density is $\sim 52\%$ in a primitive cubic arrangement and $\sim 74\%$ in a close-packed arrangement) (24). This shows that establishing such highly packed situations is the challenge of the future. Extrapolating the results obtained here to such networks, and assuming the local situation to be unchanged, conductivity increases by one order of magnitude at around 10-15% can be expected also for the systems considered here. Simultaneously, and more importantly, a high kinetic stability should occur. Should blocking effects dominate, the lithium transference number is expected to be substantially increased nevertheless. In order to achieve and maintain such high ζ -potentials a high salt concentration is necessary.

4. DISCUSSION

5

Conclusions

In this contribution results are presented that rely on the addition of SiO₂ particles to liquid electrolytes. The networks formed are attractive as the shear thinning behaviour showed. The local conductivity anomalies can well be explained by the concept of heterogeneous systems, i. e. by breaking up ion pairs owing to adsorption of the anion on the SiO₂ surface. Yet unlike solid-solid composites questions of network stability and formation are much more delicate. This was the reason to also apply ‘Monte Carlo’ modelling. The formation as it was modeled by a ‘hit-and-stick’ mechanism, results in fractal percolating clusters. The percolating networks lead to an overall conductivity increase already at small volume fraction. This low percolation threshold obtained in experiments agrees with modelling results received for large size percolation system. On a longer time scale, these networks coarsen and in consequence lose the percolation path, then they sediment at the same time trapping solvent. This can be seen from both experiments and modelling. It is in particular shown that time variations in the operational time window only comprise network variations involving particles with few neighbours, while having packed particles are kinetically very stable.

It was proved that the coherent network stability is higher **(1)** if the oxide particles size is smaller, **(2)** the volume fractions of oxides are greater, **(3)** the viscosity of the solvent is higher, and also **(4)** if the zeta-potential is higher. Based on this modelling strategies to design better solid-liquid electrolytes are given. Such composite electrolytes have a reasonable chance to find an application in industry as electrolytes for lithium-based batteries and other electrochemical devices.

5. CONCLUSIONS

Symbols and Abbreviations

β_{∞}, β_L	number of parallel, continuous paths
ΔE	Nernst potential difference
ΔV	potential changes, voltage
$\dot{\gamma}$	shear strain rate
η, η_s	dynamic viscosity, viscosity of suspension
γ	shear strain
κ	Debye length
λ	sound wave length
μ, μ_d	electrophoretic mobility; dynamic electrophoretic mobility
μ	ion mobility
∇P	pressure gradient of the sound wave
ν	sedimentation velocity
Ω	angular velocity
ω	monochromatic signal frequency; frequency
ϕ', ϕ''	electrical potentials
ρ_m, ρ_p	medium density, particle density
ρ	density; density contrast
σ_s, σ_m	specific conductivity of the dispersed system and medium

SYMBOLS AND ABBREVIATIONS

σ_{∞}	conductivity of bulk solution
σ	ionic conductivity
τ	shear stress (refers to rheology); time constance (refers to conductivity)
θ	phase shift between voltage and current
$\tilde{\mu}'_{Li^+}, \tilde{\mu}''_{Li^+}$	electrochemical potential of cations
ε	dielectric constant; permittivity
φ	volume fraction
ζ	zeta potential
A	area of sample; area of the electrodes
c'_{Li^+}, c''_{Li^+}	concentration of polarization voltage
c_a, c_c	salt concentrations exist at an anode, at a cathode
C	BET constant related to energy of adsorption in the first adsorbed layer
D'_i	diffusion coefficient
d_f	fractal dimension
D_{cl}	diffusion coefficient of a cluster
Du	Dukhin number
E_G	ground state energy (coarsening)
E_T	transition state energy (coarsening)
E	external electric field strength
F	Faraday constant, 96485.3399(24) C · mol ⁻¹
g	local acceleration due to gravity
h	distance between electrodes, stationary and the movable plate; thickness of sample; height
i, I, I_{total}	current, total current

SYMBOLS AND ABBREVIATIONS

i_+, i_-	partial currents carried by cations, by anions
$I_{(t=0)}$	initial current
$I_{(t=\infty)}$	steady state current
j	current densities
k_B	Boltzmann constant
k	cell constant
L_i	Onsager transport coefficients
l	speed; number of rotation
M_d	torque
M_W	molecular weight
m	mass
n	number of particles
P_0	relative pressure
p_c	threshold concentration; percolation threshold or critical concentration
P	pressure
p	probability/concentration of randomly occupied sites on a squared lattice
Q°	CPE parameter with numerical value of the admittance
r, r_g	particle radius, radius of gyration
R_g	ideal gas constant, $8.314472(15) \text{ J} \cdot \text{K}^{-1} \cdot \text{mol}^{-1}$
$R_{(t=0)}$	initial resistance
$R_{(t=\infty)}$	steady state resistance
r_{plate}	plate radius
Re	Reynolds number
R	ohmic resistance

SYMBOLS AND ABBREVIATIONS

S	stress factor
t_+	transference number
T_b	boiling temperature; boiling point
T_c	crystallization temperature
T_f	flash temperature; flash point
T_g	glass transition temperature
T_m	melting temperature; melting point
T	temperature
t	time
v	specific volume
W_m	weight of adsorbate constituting
W	weight of gas adsorbed
Z''	impedance: imaginary part
Z'	impedance: real part
Z	impedance
z	<i>CPE</i> parameter
\AA	Angstrom, 10^{-10} m
A/C	Air Conditioning
AC	Alternating Current
BET	Brunauer-Emmett-Teller Technique determining surface area
C	Capacitor
CNLS	Complex Non-Linear Least Square
CPE	Constant Phase Element
CVI	Colloid Vibration Current

SYMBOLS AND ABBREVIATIONS

DLCA	Diffusion-Limited Cluster Aggregation
DLVO	Derjaguin-Landau-Verwey-Overbeek Theory
DMC	Dimethyl Carbonate
DMSO	Dimethylsulfoxide
DSC	Differential Scanning Calorimetry
EC	Ethylene Carbonate
EIS	(Electrochemical) Impedance Spectroscopy
IVP	Ion Vibration Potential
L	Inductor
Li	Lithium
PC	Propylene Carbonate
PEDs	Portable Electronic Devices
PEG-150	Poly(ethylene glycol)dimethyl ether
PEG-350	Methoxy polyethylene glycol
PEO	Poly(ethylene oxide)
pzc	Point of Zero Charge
R	Resistor
RF	Radio Frequency
RLCA	Reaction-Limited Cluster Aggregation
SEM	Scanning Electron Microscope
SPEs	Solid Polymer Electrolytes

SYMBOLS AND ABBREVIATIONS

List of Figures

1.1	Battery technologies	2
1.2	Scheme of a lithium-ion battery	3
1.3	Conducting boundary layers in the ionic conductor	9
1.4	Heterogeneous doping concept	10
1.5	Forces between particles vs. particles distance	15
1.6	Interactions between charged particles	15
2.1	Sinusoidal voltage perturbation and current response.	25
2.2	Impedance plot in a complex plane	26
2.3	Nyquist diagram	27
2.4	Plate-Plate Sensor Systems	30
2.5	DSC thermogram for DMSO Systems	32
2.6	DSC thermograms for PEG-150, PEG-350 with different concentration of LiClO ₄	33
2.7	DSC thermograms for PEG-150 and PEG-350 systems with SiO ₂	36
2.8	Home-built system to measure conductivity	37
2.9	Bode diagram of PEG-350 composite electrolyte	39
2.10	Nyquist diagram of PEG-350 composite electrolyte	39
2.11	Schematic equivalent circuit	40
2.12	Conductivity vs. temperature of 0.1M LiCl/DMSO : SiO ₂ (300nm)	41
2.13	Conductivity vs. temperature of 1M LiClO ₄ /PEG – 150(350) : SiO ₂	42
2.14	Conductivity vs. oxides type in systems containing DMSO and PEGs	43
2.15	Conductivity vs. salt concentration in DMSO and PEG-150	44
2.16	Conductivity and its relative increase vs. SiO ₂ volume fraction	45
2.17	Conductivity vs. time of 0.1M LiClO ₄ /DMSO : SiO ₂	46

LIST OF FIGURES

2.18	Conductivity vs. time for different SiO ₂ volume fraction solutions	47
2.19	Conductivity vs. time for different LiClO ₄ concentration	48
2.20	Conductivity vs. time for solutions with different viscosity	48
2.21	Relative conductivity changes vs. time	49
2.22	Sedimentation effect on the samples	50
2.23	Current vs. time of DMSO systems	54
2.24	Current vs. time of PEG-150 systems	57
2.25	Double layer model	60
2.26	Zeta-potential vs. oxides weight fraction for ‘pure’ DMSO systems	61
2.27	Zeta-potential vs. SiO ₂ (10nm) weight fraction for DMSO electrolytes	62
2.28	Zeta-potential vs. SiO ₂ (7nm-fumed) weight fraction for DMSO electrolytes	62
2.29	Zeta-potential vs. oxides weight fraction for PEG-150 electrolytes	63
2.30	Newtonian and non-Newtonian Fluids Behaviours	65
2.31	Viscous fluid behaviour	66
2.32	Viscosity as a function of time	67
2.33	Viscosity as a function of time and volume fraction	67
2.34	Viscosity of non-Newtonian composite electrolytes	69
2.35	Irreversibility of polymer composite electrolytes	70
3.1	A fractal cluster growth according to Witten and Sander (83)	72
3.2	Kolb and co-workers simulation of the growth of clusters (87)	73
3.3	Schematic explanation of ‘Hit-and-stick’ mechanism.	76
3.4	Logarithmic function of particles numbers versus cluster average radius for different lattice sizes	78
3.5	Logarithmic function of particles numbers (mass) vs. cluster average radius for different concentrations (p)	78
3.6	Different lattice sizes of fractal structures	79
3.7	Different fractal structures for various concentration of occupied sites	80
3.8	Different fractal structures because of various sticking probabilities	80
3.9	Various situation for particles due to different number of contacts.	82
3.10	Schematic representation of coarsening (quite immobilize particle	83
3.11	Schematic representation of coarsening (quite mobile particle).	84

LIST OF FIGURES

3.12	Changes in fractal structures due to coarsening	85
3.13	Different fractal structures for various concentration of occupied sites due to coarsening	86
3.14	Changes in fractal structures after coarsening due to changes in sticking probability	86
3.15	Examples of ‘trapping’ due to coarsening (Lattice[100,100], concentra- tion $p=0.3$, 10000 Monte Carlo Steps).	87
3.16	Changes in very concentrated fractal structures after coarsening.	87
3.17	Coarsening process decelerates with time. Significant coarsening of ‘lose particles’ occurs on a shorter time scale (until ~ 1000 Monte Carlo Steps).	88
4.1	Typical plot representation conductivity versus SiO_2 volume fraction for starting and steady state situations.	90
4.2	Coarsening kinetics depend on the packing density.	92
4.3	Schematic representation of various behaviours in diluted and concen- trated systems.	94

LIST OF FIGURES

List of Tables

2.1	Properties of solvents used in electrolytes	20
2.2	Oxides Properties	23
2.3	Thermal properties of PEG-150, 1M LiClO ₄ /PEG-150 and the influence of SiO ₂ particles on the mentioned systems.	34
2.4	Thermal properties of PEG-350, 1M LiClO ₄ /PEG-350 and the influence of SiO ₂ particles on the mentioned systems.	34
2.5	Fitting parameters for 1M LiClO ₄ /PEG – 350 : SiO ₂	40
2.6	Table of measured currents and resistances in DMSO systems	56
2.7	Table of the t_+ of DMSO systems	56
2.8	Table of the t_+ of PEG-150 systems	56
2.9	Table of measured currents and resistances in PEG-150:SiO ₂ , 7nm-fumed systems	58
2.10	Table of measured currents and resistances in PEG-150:SiO ₂ , 10nm systems	59
2.11	Zeta-potential of 0.01M LiClO ₄ /PEG-350:SiO ₂	63
3.1	Estimates for the average threshold concentration	77

LIST OF TABLES

Bibliography

- [1] Tarascon, J. M. and Armand, M. *Nature* **414**(6861), 359–365 (2001). 1, 2, 3, 5, 6
- [2] Whittingham, M. S. *Science* **192**(4244), 1126–1127 (1976). 1
- [3] Broadhead, J. and Butherus, A. D., Rechargeable nonaqueous battery, Patent 05/274,596 (1972). 2
- [4] Broadhead, J., DiSalvo Jr., F. J., and Trumbore, F. A., Non-aqueous battery using chalcogenide electrode, Patent 05/352,514 (1973). 2
- [5] Murphy, D. W., Disalvo, F. J., Carides, J. N., and Waszczak, J. V. *Materials Research Bulletin* **13**(12), 1395–1402 (1978). 2
- [6] Lazzari, M. and Scrosati, B. *Journal of The Electrochemical Society* **127**(3), 773–774 (1980). 2
- [7] Bruce, P. G., Scrosati, B., and Tarascon, J. M. *Angewandte Chemie International Edition* **47**(16), 2930–2946 (2008). 3
- [8] Will, F. G., Hermetically sealed secondary battery with lanthanum nickel anode, Patent 05/374,907 (1975). 2
- [9] Wikipedia. *The Free Encyclopedia* (2009). 3
- [10] Basu, S., Rechargeable battery, Patent 06/208,878 (1980). 3
- [11] Padhi, A. K., Nanjundaswamy, K. S., and Goodenough, J. B. *Journal of The Electrochemical Society* **144**(4), 1188–1194 (1997). 4
- [12] Kang, B. and Ceder, G. *Nature* **458**(7235), 190–193 (2009). 4
- [13] Blonsky, P. M., Shriver, D. F., Austin, P., and Allcock, H. R. *Solid State Ionics* **18-19**(Part 1), 258 (1986). 5

BIBLIOGRAPHY

- [14] Skaarup, S., West, K., and Zachau-Christiansen, B. *Solid State Ionics* **28-30**(Part 2), 975–978 (1988). 5
- [15] Capuano, F., Croce, F., and Scrosati, B. *Journal of The Electrochemical Society* **138**(7), 1918–1922 (1991). 5, 7
- [16] Wieczorek, W., Florjanczyk, Z., and Stevens, J. R. *Electrochimica Acta* **40**(13-14), 2251 (1995). 5
- [17] Gray, F. M. *Solid polymer electrolytes: fundamentals and technological applications*. VCH Publishers, Inc., Weinheim, (1991). 5, 16, 21
- [18] Nazri, G.-A. and Pistoia, G., editors. *Lithium Batteries. Science and Technology*. Kluwer Academic Publishers, Norwell, (2004). 5
- [19] Scrosati, B. *Applications of Electroactive Polymers*. Chapman and Hall, London, (1993). 5, 16
- [20] Xu, W. and Angell, C. A. *Electrochimica Acta* **48**(14-16), 2029–2035 (2003). 6
- [21] Alarco, P.-J., Abu-Lebdeh, Y., Abouimrane, A., and Armand, M. *Nat Mater* **3**(7), 476 (2004). 6
- [22] Gores, H. J. and Barthel, J. M. G. *Pure And Applied Chemistry* **67**(6), 919–930 (1995). 7
- [23] Chandra, A. and Maier, J. *Solid State Ionics* **148**(1-2), 153 (2002). 7
- [24] Bhattacharyya, A. J. and Maier, J. *Advanced Materials* **16**(9-10), 811–814 (2004). 7, 8, 16, 91, 95
- [25] Kumar, B. and Rodrigues, S. J. *Solid State Ionics* **167**(1-2), 91 (2004). 7
- [26] Maier, J. *Progress in Solid State Chemistry* **23**, 171 (1995). 9, 10, 16, 91
- [27] Liang, C. C. *Journal of The Electrochemical Society* **120**(10), 1289 (1973). 9
- [28] Shahi, K. and Wagner, J. J. B. *Applied Physics Letters* **37**(8), 757–759 (1980). 9
- [29] Maier, J. *Physical Chemistry of Ionic Materials. Ions and Electrons in Solids*. John Wiley and Sons Ltd., Chichester, (2005). 9, 10
- [30] Shaw, D. J. *Introduction to Colloid and Surface Chemistry*, volume Third Edition. Butterworth and Co. Ltd., Great Britain, (1980). 11, 12, 50

- [31] Bunde, A. and Havlin, S., editors. *Fractals and Disordered Systems*. Springer-Verlag Berlin, Heidelberg. 13, 14, 75, 77
- [32] Bhattacharyya, A. J., Dolle, M., and Maier, J. *Electrochemical and Solid-State Letters* **7**(11), A432–A434 (2004). 16
- [33] Bhattacharyya, A. J., Maier, J., Bock, R., and Lange, F. F. *Solid State Ionics* **177**(26-32), 2565–2568 (2006). 16, 91, 95
- [34] Wieczorek, W., Lipka, P., Zukowska, G., and Wycislik, H. *J. Phys. Chem. B* **102**(36), 6968–6974 (1998). 16
- [35] Marcinek, M., Zalewska, A., Zukowska, G., and Wieczorek, W. *Solid State Ionics* **136-137**, 1175–1179 (2000). 16
- [36] Stephan, M. A. and Nahm, K. S. *Polymer* **47**(16), 5952 (2006). 16, 95
- [37] Berthier, C., Gorecki, W., Minier, M., Armand, M. B., Chabagno, J. M., and Rigaud, P. *Solid State Ionics* **11**(1), 91 (1983). 16
- [38] Bruce, Peter, G., editor. *Solid State Electrochemistry*. Cambridge University Press, Cambridge, (1995). 16, 20
- [39] Besenhard, J. O. *Handbook of Battery Materials*, volume Volume 29. Wiley-Vch, (1999). 16
- [40] Wieczorek, W., Raducha, D., Zalewska, A., and Stevens, J. R. *J. Phys. Chem. B* **102**(44), 8725–8731 (1998). 16
- [41] Jayathilaka, P. A. R. D., Dissanayake, M. A. K. L., Albinsson, I., and Mellander, B. E. *Electrochimica Acta* **47**(20), 3257–3268 (2002). 16
- [42] Adebahr, J., Best, A. S., Byrne, N., Jacobsson, P., MacFarlane, D. R., and Forsyth, M. *Phys. Chem. Chem. Phys.* **5**, 720–725 (2003). 16
- [43] Fry, A. J. *Synthetic Organic Electrochemistry*. John Willey, London, second edition, (1989). 19
- [44] Izutso, K. *Electrochemistry in Nonaqueous Solutions*. Willey-VCH Verlag GmbH, (2002). 19, 20
- [45] *CRC Handbook of Chemistry and Physics (A Ready-Reference Book of Chemical and Physical Data)*. CRC Press, Inc., Boca Raton, Florida, 61st edition, (1980-1981). 20

BIBLIOGRAPHY

- [46] Xu, K. *Chemical Reviews* **104**(10), 4303–4418 (2004). 21
- [47] Kumar, T. P., Prabhu, P. V. S. S., Srivastava, A. K., Bejoy Kumar, U., Ranganathan, R., and Gangadharan, R. *Journal of Power Sources* **50**(3), 283–294 (1994). 21, 41
- [48] Pyper, N. C. and Popelier, P. *Journal of Physics: Condensed Matter* (2), 471–488 (1997). 21
- [49] Reed, J. S. *Principles of Ceramics Processing*. John Wiley and Sons Inc., New York, 2nd edition, (1995). 22
- [50] Barsoukov, E. and Macdonald, J. R., editors. *Impedance Spectroscopy Theory, Experiments, and Applications*. John Wiley and Sons, Inc., Hoboken, New Jersey, second edition. 25
- [51] Enderby, J. A. *Proceedings of the Royal Society of London. Series A, Mathematical and Physical Sciences* **207**(1090), 329–342 (1951). 28
- [52] O’Brien, R. W. *Journal of Fluid Mechanics Digital Archive* **190**(1), 71–86 (1988). 28, 29
- [53] Dukhin, A. S., Shilov, V. N., Ohshima, H., and Goetz, P. J. *Langmuir* **15**(20), 6692–6706 (1999). 28
- [54] Dukhin, A. S., Ohshima, H., Shilov, V. N., and Goetz, P. J. *Langmuir* **15**(10), 3445–3451 (1999). 28
- [55] Dukhin, A. S. and Goetz, P. J. *Ultrasound for Characterizing Colloids. Particle Sizing, Zeta Potential, Rheology*. Elsevier B.V., Amsterdam, (2002). 28, 29
- [56] Mangelsdorf, C. S. and White, L. R. *Journal Of The Chemical Society-Faraday Transactions* **94**(16), 2441–2452 (1998). 28
- [57] Mangelsdorf, C. S. and White, L. R. *Journal Of The Chemical Society-Faraday Transactions* **94**(17), 2583–2593 (1998). 28
- [58] Ohshima, H. *Colloid and Polymer Science* **285**(13/October), 1411–1421 (2007). 29
- [59] Goodwin, J. W. and Hughes, R. W. *Rheology for Chemists. An Introduction*. The Royal Society of Chemistry, Cambridge, (2000). 30, 50, 51

-
- [60] Marcinek, M., Ciosek, M., Zukowska, G., Wieczorek, W., Jeffrey, K. R., and Stevens, J. R. *Solid State Ionics* **171**(1-2), 69–80 (2004). 33
- [61] Gaikwad, A. N., Wood, E. R., Ngai, T., and Lodge, T. P. *Macromolecules* **41**(7), 2502–2508 (2008). 33
- [62] Hoehne, G., Hemminger, W., and Flammersheim, H.-J. *Differential Scanning Calorimetry*. Springer-Vorlag, Berlin, Heidelberg, second edition, (2003). 33
- [63] Lind, J. E., Zwolenik, J. J., and Fuoss, R. M. *Journal of the American Chemical Society* **81**(7), 1557–1559 (1959). 38
- [64] Wagner, C. *The Journal of Chemical Physics* **18**(1), 62–68 (1950). 52
- [65] Hebb, M. H. *The Journal of Chemical Physics* **20**(1), 185–190 (1952). 52
- [66] Yokota, I. *J. Phys. Soc. Jpn.* **16**(11), 2213–2223 (1961). 52
- [67] Maier, J. *Zeitschrift Fur Physikalische Chemie Neue Folge* **140**(2), 191–215 (1984). 52
- [68] Evans, J., Vincent, C. A., and Bruce, P. G. *Polymer* **28**(December), 2324–2328 (1987). 52
- [69] Maier, J. *Journal of the American Ceramic Society* **76**(5), 1212–1217 (1993). 53
- [70] Maier, J. *Journal of the American Ceramic Society* **76**(5), 1218–1222 (1993). 53
- [71] Maier, J. *Journal of the American Ceramic Society* **76**(5), 1223–1227 (1993). 53
- [72] Maier, J. *Journal of the American Ceramic Society* **76**(5), 1228–1232 (1993). 53
- [73] Kaskhedikar, N., Paulsdorf, J., Burjanadze, A., Karatas, Y., Roling, B., and Wiemhofer, H. D. *Solid State Ionics* **177**(26-32), 2699–2704 (2006). 53
- [74] Maier, J. (*in preparation*) (2009). 53
- [75] Kumar, P., Kapur, P. C., and Saraf, D. N. *Colloid and Polymer Science* **253**(9/September), 738–743 (1975). 60
- [76] Metropolis, N. and Ulam, S. *Journal of the American Statistical Association* **44**(247), 335–341 (1949). 71
- [77] Kaye, B. H. *A Random Walk Through Fractal Dimensions*. VCH Verlagsgesellschaft, Weinheim (Germany), 1st edition edition, (1989). 71, 81

BIBLIOGRAPHY

- [78] Ulam, S. and Von Neumann, J. *Bulletin of American Mathematical Society* **51**(9), Abstract 165 (1945). 71
- [79] Hubbard, D. W. *How to Measure Anything: Finding the Value of 'Intangibles' in Business: Finding the Value of Intangibles in Business*. John Wiley and Sons, Inc., New York, (2007). 71
- [80] Grinstead, C. and Snell, L. J. *Introduction to Probability*. American Mathematical Society, USA, 2nd revised edition, (1997). 71
- [81] Mandelbrot, B. B., *The Fractal Geometry of Nature*, Patent (1983). 72
- [82] Poon, W. C. K. and Haw, M. D. *Advances in Colloid and Interface Science* **73**, 71–126 (1997). 72, 73, 79
- [83] Witten, T. A. and Sander, L. M. *Physical Review Letters* **47**(19), 1400–1403 (1981). 72, 106
- [84] Weitz, D. A. and Oliveria, M. *Physical Review Letters* **52**(16), 1433 (1984). 72
- [85] Shih, W. Y., Liu, J., Shih, W.-H., and Aksay, I. A. *Journal of Statistical Physics* **62**(5), 961–983 (1991). 72
- [86] Meakin, P. *Physical Review Letters* **51**(13), 1119–1122 (1983). 73
- [87] Kolb, M., Botet, R., and Jullien, R. *Physical Review Letters* **51**(13), 1123–1126 (1983). 73, 106
- [88] Kolb, M. and Jullien, R. *J. Physique Lett.* **45**(20), 977–981 (1984). 73
- [89] Hitchcock, D. B. *The American Statistician* **57**(4), 254 (2003). 74
- [90] Metropolis, N., Rosenbluth, A. W., Rosenbluth, M. N., Teller, A. H., and Teller, E. *The Journal of Chemical Physics* **21**(6), 1087–1092 (1953). 74
- [91] Hastings, W. K. *Biometrika* **57**(1), 97–109 (1970). 74
- [92] Freundlich, H. and Roeder, H. L. *Transactions of the Faraday Society* **34**, 308 – 316 (1938). 93
- [93] Pivinskii, Y. *Refractories and Industrial Ceramics* **38**(2), 54–60 (1997). 93
- [94] Zaman, A. A. and Moudgil, B. M. *Emulsions, Foams, And Thin Films* , 399–409 (2000). 93

BIBLIOGRAPHY

- [95] Edwards, W. V., Bhattacharyya, A. J., Chadwick, A. V., and Maier, J. *Electrochemical and Solid-State Letters* **9**(12), A564–A567 (2006). 95
- [96] Beyazyildirim, S., Kreuer, K. D., Schuster, M., Bhattacharyya, A. J., and Maier, J. *Advanced Materials* **20**(7), 1274–1278 (2008). 95
- [97] Wang, H., Holmberg, B. A., Huang, L., Wang, Z., Mitra, A., Norbeck, J. M., and Yan, Y. *Journal of Materials Chemistry* **12**(4), 834–837 (2002). 95
- [98] Herring, A. M. *Polymer Reviews* **46**(3), 245 – 296 (2006). 95

BIBLIOGRAPHY

Acknowledgments

First, I would like to thank Prof. Dr. Joachim Maier for guiding me through my doctoral studies, for giving me this chance to work independently in great place between remarkable scientists, colleagues and friends. Thank you for all fruitful discussions, suggestions, patience and charity, especially during correcting my thesis.

Second, I would like to thank Prof. Armin Bunde and Dr. Kosmas Kosmidis (present Aristotle University in Thessaloniki) from the University of Giessen for an effective collaboration, all invaluable modelling lessons and introducing me the “fractals” world. I would like also to thank all Theoretical Physics III group members from the University of Giessen for their kindness and help during my staying in Giessen.

I am grateful to Prof. Dr. Klaus Müller, Prof. Dr. Joachim Bill, Prof. Dr. Thomas Schleid for kindly accepting their participation in the examination committee.

I would like to thank affably Sofia Weiglein for enormous help, patience and goodwill with explaining me all formal procedures and rules, for support in every situation.

Many thanks to all my friends and colleagues from the Max Planck Institutes in Stuttgart and also from Research School, especially I would like to thank Dr. Hans-Georg Libuda for all his support, patience and help.

Absolute thanks to present and past group members for making this entire time in the group and in Germany full of unforgettable memories. In very special way I would like to thank to Dr. Sarminala Hore for everything she did since my first day at Max Planck Institute, for numerous invaluable discussions, support, patience and willingness. Many thanks for

finding the time to correct this thesis, for all insights and advices. Also great thanks to Dr. Dominik Samuelis for everyday discussion, patience, friendliness and help especially with some computer problems. Great thanks to Dr. Katja Weichert for all help with the “Zusammenfassung” and Dr. Mykola Tasinkevych (Max Planck Institute for Metals Research, group of Prof. Dr. S. Dietrich) for all help and discussions concerning DLCA theory.

I would like to thank Annette Fuchs for providing support on the BET, SEM and Ewald Schmitt for DSC measurements and enormous help with creating the conductivity setup, cells etc., also Gabi Götz, Udo Klock, Peter Senk, Barbara Reichert and Renee Stotz for kindness and willingness to help. Thanks to Wolfgang Koenig (Infra Red Spectroscopy), Armin Schultz (Raman Spectroscopy), Dr. Francesco Giannici (Palermo University; Small-angle X-ray scattering), Dr. Jens Weber (Max Planck Institute of Colloids and Interfaces, Berlin; Dynamic Light Scattering) for measurements and results I did not present in this dissertation. I am grateful to Prof. Dr. F. Aldinger and Prof. Dr. Joachim Bill from Max Planck Institute for Metals Research for affording the Haake RheoStress 1 on the viscosity measurement.

Very special thanks to Uwe Traub for providing me immense IT-help, especially with programming. Invaluable appreciation for his readiness to help, discussions, kindness and patience with explaining me programming stuff and charity because of my mistakes.

At the end I would like to thank to my family, especially to my parents, to all my friends and to person close to my heart for all kinds of support I got from all of them particularly during last months.

Curriculum vitae

Anna Jarosik

Max Planck Institute for Solid State
Research
Department of Prof. J. Maier
Heisenbergstrasse 1
70569 Stuttgart, Germany

Phone: +49 (0) 711 689-1769
Mobile: +49 (0) 17665198365
Fax: +49 (0) 711 689-1722
Email: a.jarosik@gmail.com

Personal

Born on July 8, 1981.

Polish Citizen.

Single

Education

February 2006-December 2009 Doctoral degree at Max Planck Institute for Solid State Research in the Department of Prof. J. Maier and at the University of Stuttgart, in International Max Planck Research School.

September 2003-June 2004 SOKRATES/ERASMUS Scholarship at Ecole Européenne de Chimie, Polymères et Matériaux, University of Louis Pasteur, Strasbourg, Coordinator: Prof. H. Leismann

October 2000-June 2005 Poznań University of Technology, Diploma in Chemical Technology (10 semesters), Faculty of Chemical Technology, Specialization: Process and Chemical Engineering, Supervisor: Prof. A. Lewandowski, Thesis: ‘Viscosity of room temperature ionic liquids and their mixtures with molecular solvents’

Employment

2004-2006 Motorway Operation – Autostrada Eksploatacja S.A. in Poznan, *Highway Manager Assistant*

2004 Agricultural Distillery in Lezce Professional training (4 weeks)

2003 Kompania Piwowarska S.A. (SAB Miller Group) in Poznan, Professional training

Publications

Journal Articles

A. Jarosik, S. R. Krajewski, A. Lewandowski, P. Radzimski ‘Conductivity of ionic liquids in mixtures’, *Journal of Molecular Liquids* 123 (2006) 43–50.

A. Jarosik, S. Hore, N. Kaskhedikar, J. Maier ‘Heterogeneously doped polyethylene glycol as nano-composite soft matter electrolyte’, 2009, (*in preparation*).

A. Jarosik, A. Bunde, J. Maier, ‘Ion Conducting Particle Networks in Liquids: Modelling of Network Stability’, 2009, (*in preparation*).

Workshops and Conferences

IMPRS-Summer School ‘Dynamics Moving Matter on Different Time Scales Part I: Basics and Diffusion’ and ‘Part II: Phase Transformations and Soft Matter’ (2006).

Zahner Mess Systeme Seminar: Kronacher Impedanztage (2006).

38th IFF Spring School 2007 (Forschungszentrum Jülich) ‘Probing the nanoworld- Microscopies, Scattering and Spectroscopies of the Solid State’ (2007).

IMPRS-Winter School ‘Magnetism in nanostructures and novel materials’ (2008).

Höchstleistungsrechenzentrum Stuttgart (HLRS): ‘Programming in Fortran’ (2008).

59th Annual Meeting of the International Society of Electrochemistry, Seville, Spain, poster: *Percolation of oxide networks in composites of solid and non-aqueous lithium salt solutions*, (2008).

International Workshop on Fundamentals of Lithium-based Batteries, Schloss Ringberg, Germany, poster: *Conductivity and Stability of Particle Networks in Liquids*, (2008).

IMPRS-Winter School 'Nanoscale Materials: Structure-Property-Relations', poster: *Conductivity and stability of particle networks in liquid electrolytes*, (2009).

Bunsentagung Köln, Germany, poster: *Conductivity and stability of particle networks in composite lithium based electrolytes*, (2009).

5th Kurt Schwabe Symposium, Erlangen, Germany, oral presentation: *Conductivity and stability of oxide particles networks in composite non-aqueous electrolytes*, (2009).

17th Conference on Solid State Ionics, Toronto, Canada, oral presentation: *Percolation of oxide networks in composite lithium based electrolytes*, (2009).

International Conference on Materials for Advanced Technologies, Singapore, poster: *Conductivity and stability of particle networks in composite lithium based electrolytes*, (2009).

Lithium Batteries Discussion (LiBD), Arcachon, France, poster: *Conductivity and stability of particle networks in composite lithium based electrolytes*, (2009).